

Institut für Theoretische Physik  
Fakultät Mathematik und Naturwissenschaften  
Technische Universität Dresden

# **Understanding Mechanics and Polarity in Two-Dimensional Tissues**

Dissertation  
zur Erlangung des akademischen Grades  
Doctor rerum naturalium

vorgelegt von  
**Douglas B. Staple**

Max-Planck-Institut für  
Physik komplexer Systeme

Dresden 2012

*This thesis is dedicated to my friend, Shane A. Smith.*

Eingereicht am 3.2.2012

1. Gutachter: Prof. Dr. Frank Jülicher
2. Gutachter: Prof. Dr. Klaus Kroy

Verteidigt am 21.3.2012

# Abstract

During development, cells consume energy, divide, rearrange, and die. Bulk properties such as viscosity and elasticity emerge from cell-scale mechanics and dynamics. Order appears, for example in patterns of hair outgrowth, or in the predominately hexagonal pattern of cell boundaries in the wing of a fruit fly. In the past fifty years, much progress has been made in understanding tissues as living materials. However, the physical mechanisms underlying tissue-scale behaviour are not completely understood. Here we apply theories from statistical physics and fluid dynamics to understand mechanics and order in two-dimensional tissues. We restrict our attention to the mechanics and dynamics of cell boundaries and vertices, and to planar polarity, a type of long-ranged order visible in anisotropic patterns of proteins and hair outgrowth.

Our principle tool for understanding mechanics and dynamics is a vertex model where cell shapes are represented using polygons. We analytically derive the ground-state diagram of this vertex model, finding it to be dominated by the geometric requirement that cells be polygons, and the topological requirement that those polygons tile the plane. We present a simplified algorithm for cell division and growth, and furthermore derive a dynamic equation for the vertex model, which we use to demonstrate the emergence of quasistatic behaviour in the limit of slow growth. All our results relating to the vertex model are consistent with and build off past calculations and experiments.

To investigate the emergence of planar polarity, we develop quantification methods for cell flow and planar polarity based on confocal microscope images of developing fly wings. We analyze cell flow using a velocity gradient tensor, which is uniquely decomposed into terms corresponding to local compression, shear, and rotations. We argue that a pattern in an inhomogeneously flowing tissue will necessarily be reorganized, motivating a hydrodynamic theory of polarity reorientation. Using such a coarse-grained theory of polarity reorientation, we show that the quantified patterns of shear and rotation in the wing are consistent with the observed polarity reorganization, and conclude that cell flow reorients planar polarity in the wing of the fruit fly. Finally, we present a cell-scale model of planar polarity based on the vertex model, unifying the themes of this thesis.



# Acknowledgement

I would like to thank Prof. Jülicher for the opportunity to work and contribute to biophysics with him. This thesis relied critically on the collaborative work of theoretical physicists and experimental biologists. Experimental data presented here was obtained by experimentalists B. Aigouy, A. Sagner, and J.-C. Röper in the group of S. Eaton at MPI-CBG, Dresden. The present author developed physical theories and models in collaboration with R. Farhadifar in the group of F. Jülicher here at MPI-PKS. All material relating to planar cell polarity, both theoretical and experimental, was discussed, and often developed, in group meetings involving all of these persons and the present author. Further details of collaborative contributions are given in Appendix C. Results presented in this thesis have been published in *The European Physical Journal E* [1] and *Cell* [2].

I would like to thank the Natural Sciences and Engineering Research Council of Canada (NSERC), the German Academic Exchange Service (DAAD), and the Max Planck Society (MPG) for supporting me during my doctorate.



# Contents

<b>1</b>	<b>Introduction</b>	<b>11</b>
1.1	Biophysics of tissues	11
1.1.1	Continuum descriptions	11
1.1.2	Discrete models	13
1.2	Vertex models	13
1.3	Planar cell polarity	15
1.3.1	Hair patterns and proteins	15
1.3.2	How do cells coordinate polarity?	16
1.3.3	Theory of planar cell polarity	18
1.4	Basic questions and ideas	20
1.4.1	Why study development?	20
1.4.2	The fly wing as a model system	22
1.4.3	Simplified models as tools	22
1.4.4	Multi-scale theories	22
1.4.5	Collective phenomena, self-organization, and emergence	23
1.5	Contents of this thesis	23
<b>2</b>	<b>Vertex model for mechanics and dynamics of epithelia</b>	<b>25</b>
2.1	Potential energy or work function	25
2.2	Ground states	26
2.2.1	Polygons of minimal potential	27
2.2.2	Networks of minimal potential	30
2.3	Effects of external pressure	31
2.4	Shear and compression moduli	31
2.5	Summary	33
<b>3</b>	<b>Topological processes and tissue growth</b>	<b>35</b>
3.1	Energetics of manifold vertices	35
3.2	Cell extrusion by T2 transitions	36
3.3	Cell division in the vertex model	37
3.4	Tissue morphologies generated by growth	38
3.5	Summary	40

---

<b>4</b>	<b>Dynamics beyond the quasistatic approximation</b>	<b>41</b>
4.1	Limitations of the quasistatic approximation	41
4.2	Dynamic description of the vertex model	42
4.2.1	Generalized coordinates	42
4.2.2	Choices of dissipative forces	43
4.2.3	Area friction	44
4.2.4	Dynamic equation for the vertex model	45
4.3	Numerically solving vertex model dynamics	45
4.4	Relaxation rates	47
4.5	Effects of friction on tissue growth	49
4.6	Summary	50
<b>5</b>	<b>Quantifying tissue dynamics in experiments</b>	<b>53</b>
5.1	Cell velocity and derivative fields	54
5.1.1	Cell flow	54
5.1.2	Local rotation, shear, and compression rates	55
5.2	Planar cell polarity	59
5.2.1	Quantitative definition of planar cell polarity	60
5.2.2	Methods for application to experimental data	61
5.2.3	Average nematic order	63
5.2.4	Quantified polarity patterns at cell and tissue scales	64
5.2.5	Connection with nematic liquid crystals	64
5.3	Summary	67
<b>6</b>	<b>Theoretical framework for planar cell polarity</b>	<b>69</b>
6.1	Hydrodynamic theory of polarity reorientation	69
6.1.1	Theoretical background	69
6.1.2	Simplified dynamic equation for polarity reorientation	70
6.1.3	Application to observed polarity reorientation	71
6.1.4	Testing the model: Severed wings	74
6.2	Planar cell polarity in the vertex model	77
6.3	Summary	81
<b>7</b>	<b>Conclusions</b>	<b>83</b>
<b>A</b>	<b>Ground states of the vertex model</b>	<b>87</b>
A.1	Networks of identical cells	87
A.2	General networks of cells	87
<b>B</b>	<b>Topological processes and tissue growth</b>	<b>91</b>
B.1	Topological changes	91
B.1.1	T1 transitions	91
B.1.2	T2 transitions	92
B.2	Comparison of growth algorithms	92

---

<b>C Collaborative contributions .....</b>	<b>95</b>
<b>Bibliography .....</b>	<b>97</b>



# 1 Introduction

## 1.1 Biophysics of tissues

Tissues are materials formed from groups of cells, for example muscles, blood, bones, epithelia such as skin, and brain tissue [3, 4]. Relevant length scales are that of individual cells ( $\mu\text{m}$ ) up to the scale of whole tissues, varying from, e.g.,  $< 1$  mm for the wing of a developing fly up to meters for the skin of a large mammal. Tissues are active materials, i.e. they consume energy, typically in the form of ATP (adenosine triphosphate), in order to perform their various functions. This leads to material properties not normally observed in inanimate materials. For example, cell division in tissues causes the generation of local force dipoles [5]. Thus, anisotropic cell division can lead to an active anisotropic stress, which can in turn induce shear flow in tissues. In this way a tissue can flow and shear spontaneously, i.e. without necessarily having any external body act on it. Further properties arise from fluctuations accompanying such active processes. For example, fluctuations induced by cell division can relieve strain energy in an otherwise elastic tissue, causing it to behave as a viscous fluid [5]. In the remainder of this section we review specific concepts dealing with the biophysics of tissues relevant for this thesis.

### 1.1.1 Continuum descriptions

It is now standard practice to describe tissues on large length scales as continuous materials. However, the appropriate continuum description has been significantly debated. In the 1960s and 1970s, M. S. Steinberg wrote a series of papers pioneering a fluid model of tissues [6–11]. This fluid model was motivated by three related experimental phenomena: the sorting out of mixtures of distinct cell types, the spreading of one tissue over another, and the preferential adhesion of tissue fragments. As early as 1907, H. V. Wilson observed that “cells and cell clusters obtained by squeezing a sponge through the meshes of fine, silk, bolting cloth could reunite, and that aggregates obtained this way could reconstitute themselves into functional sponges” [9, 12]. Later, in 1944 J. Holtfreter directly observed cell-sorting in tissues dissociated using basic solution and subsequently allowed to reassociate under neutral pH [9, 13]. Additional experiments in vertebrates confirmed that intermixed cell types can spontaneously sort [9, 14–19]. In these experiments, as well as in normal development, it was typical to observe one tissue type spreading over

the surface of another. These experiments [13–19] were performed in the context of previous results by Holtfreter [20, 21], and later Weiss [22], which demonstrated preferential adhesion between tissue types [9, 23]. Ultimately, all these phenomena were explained in a seminal paper by Steinberg in 1963 [9], wherein different cell types were described as immiscible liquids, with surface tension resulting from preferential adhesion the dominant interaction. Early fluid models focused primarily on equilibrium arguments [9, 10], and thus made no mention of viscosity. Most real fluids are viscous, so a viscous fluid theory of tissues is a natural development following the early work of Steinberg *et al.* [24–27].

A simple fluid description of tissues is compelling and has predictive power, and the experiments that motivate such a description are remarkable. However, the fluid description of Steinberg and coworkers is incomplete. Clearly blood behaves as a fluid. Bone, however, usually does not. In fact, tissues including bone, cartilage, and muscle have been routinely described as nonlinear elastic solids since at least the 1960s [28]. This is consistent with the experimental fact that tissues generate a restoring force when deformed, even over long periods of observation. Stated more bluntly, “While it is possible that for very large times of observation, the stress could relax to zero, it is highly unlikely for were it to be true, tissue cannot retain its shape and our body would eventually ‘flow’ and would cease to have form” [29].

A more complete picture is that all tissues are viscoelastic materials, and different tissues may show liquid, solid, or intermediate behaviour depending on the tissue and environment. Extreme examples are blood and bone. Viscous behaviour in bone and other solid-like tissues is observed as a time-dependent stress following deformation; this stress subsequently relaxes to a constant nonzero value at long times [28]. Thus even bone exhibits viscosity, behaviour typical of a liquid. In the opposite limit, at vanishing shear rate even blood behaves elastically [28]. It is easy to simply lump all tissues into a grey-zone of viscoelastic materials. However, there remains an important qualitative distinction: In the long-time limit, will a given tissue behave as a fluid or a solid? In the terminology of Y. C. Fung, this is the difference between a viscoelastic fluid and a viscoelastic solid [28]. On timescales longer than mechanical relaxation, viscoelastic fluids flow and can be treated as viscous fluids [5, 26, 27]. Viscoelastic solids, however, maintain nonzero stress in response to a deformation even in the long time limit [29]. This distinction helps clarify the debate of elastic-solid versus viscous-fluid models of tissues. Bones and muscles fall into the category of viscoelastic solids [28]; sea sponges and embryonic tissues are well described as viscoelastic fluids. Finally, it is worth noting that tissues may undergo plastic deformation: if sufficiently large strain is induced, a viscoelastic solid may be forced to flow. Conversely, for sufficiently small strain a viscoelastic fluid behaves as a solid [28]. Thus, one might describe all tissues as visco-elastic-plastic materials, which behave as viscoelastic fluids at stresses below a given yield stress and viscoelastic solids above it [30]. Further generalization is possible by describing a biological tissue as composed of multiple components, which may themselves have distinct rheological properties [31–33].

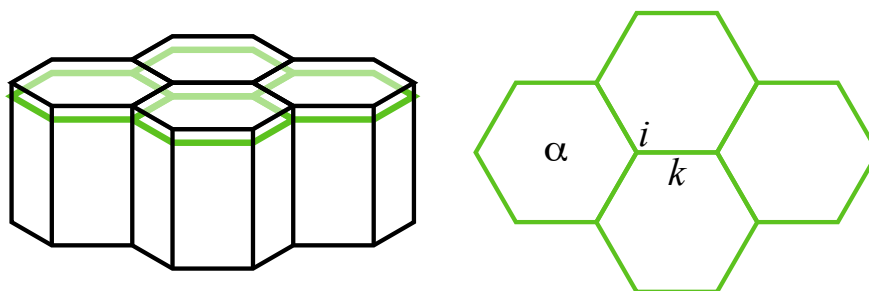


Figure 1.1: Left: Schematic representation of four columnar, hexagonal cells in an epithelium. Here adhesive “adherens” junctions are represented in green. Right: Cells in vertex models are represented in two-dimensions as networks of polygons. Labels indicate a cell  $\alpha$ , a vertex  $i$ , and a boundary  $k$ . Based on Fig. A of [69].

Continuum descriptions have also been developed and applied to problems on shorter length scales such as cell migration in the extracellular matrix [34–37] and mechanics of the cell cytoskeleton [38–47].

### 1.1.2 Discrete models

Three-dimensional models coarse-grained at the single-cell scale have been used as standard tools in the group of D. Drasdo *et al.*, in particular to study the physics of tissue growth and cancer [48–64]. In these models, cells are represented as spheres obeying simple rules: cells adhere to each other, obey volume exclusion, divide, die, and follow Langevin dynamics. Recently, related three-dimensional coarse-grained models have appeared based on dissipative particle dynamics (DPD) [5, 65]. One way in which DPD simulations differ from previous Langevin-dynamic models is that they allow the possibility for internally generated dissipative forces, i.e., exchanged between cells, to dominate over dissipation with respect to a background medium.

Owing to their primarily two-dimensional morphology, epithelia are particularly well suited to theoretical studies at the single-cell level. For example, some epithelial properties such as polygon distributions can be described using topological arguments alone [66–68]. However, in order to understand the biomechanics of such tissues at the single-cell level, it is necessary to develop physical models describing stresses and forces on constituent cells. One type of discrete model for two-dimensional tissues are vertex models, which describe epithelia as networks of polygons at the level of the adherens junctions.

## 1.2 Vertex models

We define “vertex model” as a coarse-grained model describing mechanical forces on a network of polygons. Such a definition is experimentally motivated as follows.

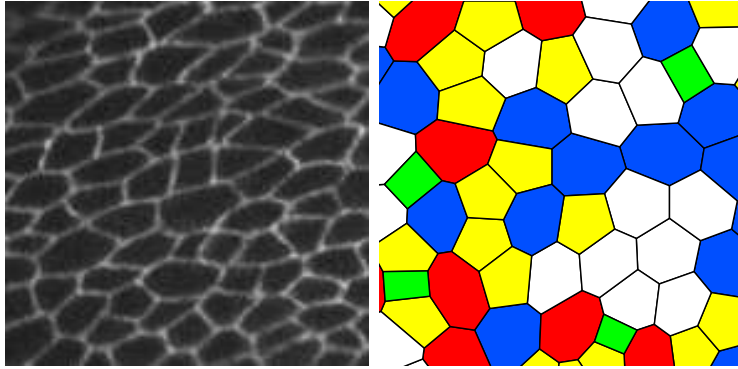


Figure 1.2: Left (A): Confocal microscope image of a developing *Drosophila* wing (E-cadherin labelled with green fluorescent protein in a wing disc epithelium). Right (B): Epithelia in vertex models are represented as networks of polygons.

Near the surface of an epithelium, cellular contacts are tightly controlled in a network of so-called adherens junctions. These junctions are enriched with cell adhesion proteins called cadherins, which promote cell adhesion via homophilic interactions [70]. At the level of the adherens junctions, the wing epithelium resembles a network of polygons, see Fig. 1.2a. Thus, an epithelium can be described at this level using a set of vertex positions and the connections between them. During development, the biophysical properties of cells and their contacts generate mechanical forces. These forces act in turn on the epithelial network, driving topological changes and the relative motion of vertices. Here topological changes include cell division, cell boundary rearrangement, and cell extrusion via apoptosis. Conversely, such topological changes can be active processes, themselves inducing forces on cells and their neighbours. Thus, mechanical forces and network dynamics undergo a subtle interplay as the cellular network evolves dynamically.

In a vertex model, force balance must be satisfied for any stable and stationary network, irrespective of the nature of the forces acting on the network. However, it is necessary to dictate an explicit form for the forces acting on the network in order to make closer contact with experiment. These forces are typically written as the gradient of a potential energy or work function [69, 71]. Such a choice is valid in the quasistatic limit, i.e., on timescales long compared to local mechanical relaxation in the tissue. The choice of forces is one property that differentiates two vertex models from one another. Recently, Farhadifar *et al.* described a vertex model that can account for the geometrical and mechanical properties of the wing disc [69, 71], which is the precursor structure that ultimately forms the fly wing.

Vertex models have been used to discuss tissue morphology [72], dynamics [73, 74], and, more recently, to study detailed problems such as the dynamics of wound closure [75], cell sorting [76], the mechanical regulation of cell division and growth [77], the emergence and reorientation of planar polarity [2], and the dynamics of

growth control and morphogen scaling [78, 79]. Early models were evoked in discussions of foam [80–84] and grain boundaries [85, 86] rather than living tissue, and these parallels continue today [87, 88]. Similar models have also been used to study wound closure [89] and the geometric structure of ommatidia in the *Drosophila* eye [90]. Vertex models can be made computationally efficient in two dimensions, however it is not straightforward to generalize vertex models to three dimensions. An important method has been to use a modification of the many-states Potts model [91–95] in order to represent complex cell shapes in two and three dimensions. A slightly different approach is to treat cells exclusively using cell-centers (see [96] and references therein); such calculations are typically less detailed but more computationally efficient. Tissues have also been recently treated on large length scales using continuum descriptions [39, 97, 98], see Sect. 1.1.

Vertex models in their simplest forms help one to understand geometry, mechanics, and dynamics of the cellular arrangements in epithelia. Vertex models gain further significance in their extensions: details can naturally be incorporated in order to understand higher biochemical and biophysical properties of epithelia, such as the emergence and reorientation of planar polarity in the fly wing.

## 1.3 Planar cell polarity

### 1.3.1 Hair patterns and proteins

Planar polarity refers to broken symmetries in the plane of an epithelium [99–105]. These broken symmetries are most visible in the outgrowth of external structures. For example, in the pattern of hair outgrowth on the human arm, hairs tend to align over the length of the arm. Similarly, near the end of development of the fly wing, a single hair grows from each cell on the wing and points in the distal direction, see Fig. 1.3. Hairs can therefore be used to define a pattern of planar polarity at the end of development in the fly wing. However, the mechanisms governing the emergence and dynamics of planar polarity are not well understood. Planar polarity is an example of long-range order in biological systems. In this context “long-range” refers to the scale of complete tissues or organisms. Many physical systems exhibit long-range order, for example in ferromagnetic transitions. However, no physical analogue to magnetism is apparent in the wing of the fruit fly.

The pattern of hair outgrowth is determined by the distribution of certain proteins called planar cell polarity (PCP) proteins [100–102]. Although the pattern of hair outgrowth provides a straightforward and intuitive measure of planar polarity, hair outgrowth occurs at a single time point at the end of development. It is thus necessary to investigate the distribution of PCP proteins in order to probe the dynamics of planar polarity prior to hair outgrowth. These PCP proteins are distributed anisotropically in the plane of the epithelium, and evolve dynamically during development. At the time of hair outgrowth, PCP proteins are localized in complexes at proximal and distal cell boundaries, see Fig. 1.4. Naming only the

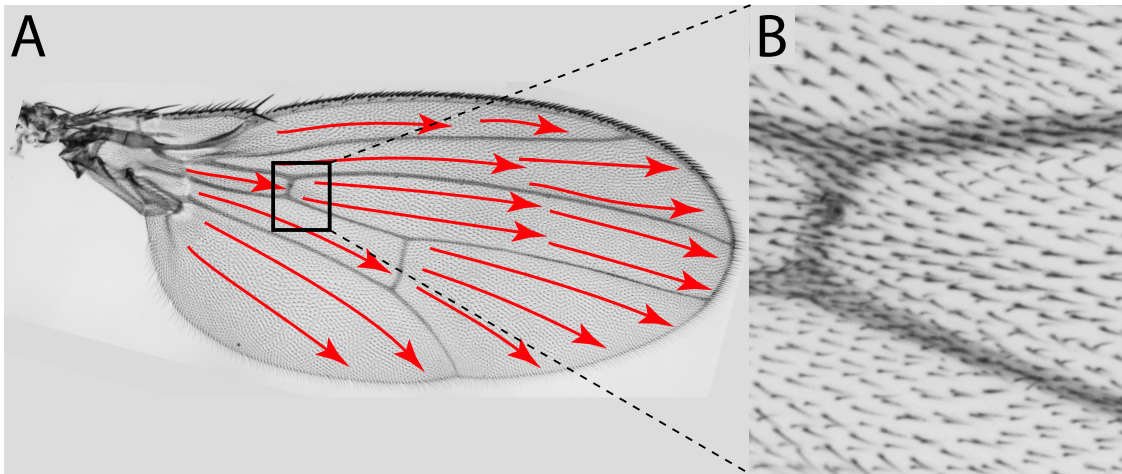


Figure 1.3: (A) Hair pattern on the adult wing of the fly exhibiting large-scale order with wing hairs pointing towards the distal end of the wing. Arrows indicate the hair orientation in different regions. (B) Higher magnification of region in (A) reveals individual wing hairs. Experimental images courtesy of Suzanne Eaton, MPI-CBG.

so-called “core” PCP proteins, complexes containing the proteins Flamingo (Fmi), Strabismus (Stbm), and Prickle (Pk) are found on proximal cell boundaries at the end of development, see Fig. 1.4. These proximal protein complexes interact across cell boundaries with distal complexes containing the proteins Flamingo (Fmi), Frizzled (Fz), Dishevelled (Dsh), and Diego (Dgo); here the protein Flamingo (Fmi) localizes to both distal and proximal cell boundaries. Thus, PCP proteins in individual cells align with the proximal-distal axis (PD-axis, the long axis of the wing) during development prior to hair outgrowth.

### 1.3.2 How do cells coordinate polarity?

How can individual cells align to form a long-ranged polarity pattern? Possible mechanisms can be divided into two categories: (i) global signals, where each cell polarizes independently from its neighbours in response to some global spatial cue or cues, and (ii) local signals, where cells polarize in response to spatial cues that are received from a limited number of neighbours. Over twenty years of genetic experiments show that PCP is controlled locally, via spatial information transmitted between neighbouring cells [101]. Nevertheless, we review here the evidence for and against both of these two classes of mechanisms, (i) and (ii), in order to form a more complete picture of the mechanisms controlling PCP in the fly wing.

Chemical species often form concentration gradients in tissues. In the wing, the proteins Four-Jointed (Fj) and Dachshous (Ds) form opposing concentration gradients: Ds is found in high levels in proximal regions of the wing that give rise to the wing hinge and at lower levels in the wing blade. Fj is expressed in an opposite gra-

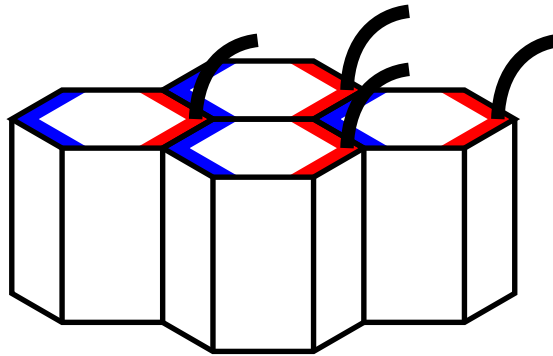


Figure 1.4: Planar cell polarity (PCP) proteins localize in complexes across proximal (blue) and distal (red) cell boundaries. At the end of development, a single hair grows from the distal vertex of each cell, pointing in the distal direction.

dient, with levels highest in the wing blade. Such gradients could theoretically act as global spatial cues in the wing, with individual cells polarizing along the axis of a gradient. In support of this idea, Ds and Fj are necessary for the proper functioning of the PCP system, together with another protein called Fat (Ft), which is expressed uniformly in the wing. Ds is a ligand for Ft, and Fj is proposed to regulate Ft/Ds activity. It is thus reasonable to propose that the combined Ft/Ds/Fj system provides global spatial cues for planar polarity in the wing. This is, however, certainly not the case in the abdomen, where the core PCP proteins including Fmi and Fz polarize independently from Ft/Ds [106]. Even in the wing, mutant flies uniformly expressing Ds in the wing still orient PCP correctly, even in the absence of Fj [107]. Furthermore, there is a temporal problem with the theory that Ft and Ds lead to the polarization of PCP proteins: Ft and Ds act at earlier developmental stages prior to pupation [107], while PCP proteins do not align with the PD-axis until later times prior to hair outgrowth [108]. Such statements about the temporal action of Ft/Ds follow from experiments on mutant flies with temperature-dependent misexpression of Ds [107]: here the experimentalist controls the temperature in a time-dependent fashion, in order to determine during which times the normal expression of Ds is necessary for the proper formation of PCP. It is clear that Ft, Ds, and Fj are somehow necessary for PCP. However, gradients of these molecules cannot explain the spatial pattern of PCP in the wing via global cues. It is of course still possible that the gradient of some other protein or chemical species provides a global cue for PCP. This is the mysterious “factor X” invoked in past models of polarity. However, after two decades of failing to observe a gradient necessary for PCP, it is now time to focus on other possible mechanisms.

The polarization of PCP protein complexes seen in the wing relies on all core PCP proteins. In mutants lacking any one PCP protein the distribution of the other PCP proteins and the resulting hair outgrowth are perturbed. However, the perturbed hair patterns in such mutant animals are not completely random: rather,

hair patterns in animals misexpressing PCP proteins show characteristic defects such as swirls [101]. In particular, hairs in mutant patterns align with their neighbours, although they do not align over the scale of the complete tissue. It is hard to imagine how such behaviour could result in a system governed by global rules. Rather, such behaviour is characteristic of local interactions: even if a system fails to attain global order, local interactions cause groups of cells to align with one another, and this alignment decays over some correlation length. Local signals are a robust mechanism for establishing global order in general. For example, in a flock of birds or a school of fish, animals successfully coordinate movement in large groups without centralized control, and without knowledge of the activity of every member of the flock or school. For the coordination of complete organisms, one expects senses such as sight to function as local cues. For the coordination of individual cells in the fly wing, PCP protein concentrations are a clear candidate. In particular, Fmi, Fz, and Stbm are transmembrane proteins: the concentration profiles of Fmi, Fz, and Stbm in a given cell directly influence the accumulation of PCP proteins in neighbouring cells. This influence is visible in experiments where clones of mutant cells misexpressing PCP proteins are introduced in wild-type tissue or vice-versa. The effects are well summarized by J. A. Zallen [101]: “When clones of *frizzled* mutant cells are generated in otherwise wild-type tissue, the hairs made by wild-type cells near the clone point toward the *frizzled* mutant cells [[109, 110], Fig. 3B in [101]]. Conversely, wild-type hairs point away from mutant cells that lack the Strabismus transmembrane protein [[111], Fig. 3C in [101]].”

It is now the status quo to explain PCP as being dominated by the local interactions of cells and their neighbours, rather than responses of cells to a global cue such as a chemical gradient. The complete picture is likely to be more complicated than that outlined here. For example, in addition to the Ft/Ds/Fj pathway, microtubules in the wing have been shown to align preferentially with the PD-axis, and it has been proposed that microtubules are involved in the formation of anisotropic PCP protein distributions, for example via directed transport of PCP proteins along the microtubule axis [112].

### 1.3.3 Theory of planar cell polarity

In the past ten years, mathematical models of PCP have appeared that attempt to account for the complex interactions of many molecular species [113–119]. Such detailed models can be used to show that a proposed mechanism is consistent with experimental observations. However, detailed models of biological systems have their shortcomings. Firstly, the chemical reactions at work in biological organisms are complex and typically not known in complete detail. Multiple assumptions are necessary to formulate a model describing such details, and the likelihood of a model being correct in detail falls exponentially with the number of independent

model assumptions <sup>1</sup>. This implies that a model involving on the order of thirty free parameters is almost certainly incorrect at the most detailed level. Furthermore, the individual assumptions necessary to construct a detailed model are more error prone due to their more precise nature, as compared to the rough assumptions necessary to construct a coarse-grained model <sup>2</sup>. Models involving, e.g., ten coupled nonlinear partial differential equations (PDEs) [115] are typically intractable analytically and thus difficult to understand in detail. It is difficult to know which of thirty parameters or ten PDEs is critical for the proper functioning of a model. Nevertheless, such models are highly flexible and thus capable of reproducing the wild-type PCP pattern and also patterns characteristic of PCP mutants [113, 115]. A pessimistic explanation would be that reproducing wild-type and mutant PCP patterns is not contingent on the knowledge or correctness of details at the molecular level. Such a position is supported by the fact that the specific models being discussed [113, 115] rely on a global biasing signal, “factor X”, which is not supported by experimental evidence, see Sect. 1.3.2. Despite the arguments presented here, detailed mathematical models are one type of tool that can be used to help understand biophysical systems, for example by motivating and providing clues for future experiments. Simplified models are a different type of tool, with different strengths and weaknesses.

It is desirable to define a simple model whose behaviour mimics that of the real system, with the hope to determine underlying physical mechanisms also present in the real system. We identify three theoretical studies of planar cell polarity that follow this philosophy [120–122]. In [120], Burak and Shraiman develop a coarse-grained model describing PCP in analogy to ferromagnetism. Their study highlights the effect of noise, and investigates the dynamics of polarity formation both in the presence and absence of an unknown global biasing signal. In [121], H. Zhu presents a phenomenological model of planar polarity via an analogy to the interactions of polarized dielectric molecules. The results of that study [121] are strongly dependent on the presence of a global biasing signal, and much of the paper is devoted to the effects of varying the global biasing signal. In [122], Schamberg, Houston, Monk, and Owen develop simplified models describing PCP as resulting from intracellular reorganization of PCP proteins combined with an intercellular inhibition in the form of a negative feedback loop. The authors consider a one-dimensional network of cells, with each cell coupled to its two neighbours. PCP activity is captured via dimensionless dynamic variables,  $l_j$  and  $r_j$  describing PCP activity on the left and right sides of cell  $j$ , respectively. Explicit choices for dynamic equations  $dl_j/dt$  and  $dr_j/dt \forall j$  allow the authors to compute steady states, linear stability analyses, and

---

<sup>1</sup>If the probability of detailed model assumption  $i$  being correct is  $p_i$ , then the probability of multiple independent model assumptions being simultaneously correct is the product  $\prod_i p_i$ .

<sup>2</sup>For example, in a highly coarse-grained model one might assume that two proteins inhibit one another’s accumulation, and investigate the consequences. In a more detailed model, one might assume that two proteins inhibit one another’s accumulation in a specific way, which is a stronger claim.



Figure 1.5: Examples of pattern formation in complex systems. Left (A): Turbulent flow in water visualized using laser-induced fluorescence [123]. Here the field of view is  $45 \times 45 \text{ mm}^2$ . The false-colour scheme represents the concentration of a fluorescent dye, with red representing the highest concentration and blue the lowest. Image reproduced with the permission of J. Westerweel. Center (B): Spiral patterns in the oxidation of carbon-monoxide on platinum revealed via photoemission electron microscopy [124, 125]. Here dark regions are covered in oxygen, and bright areas are covered in carbon-monoxide. The dimensions of the image are approximately  $445 \times 410 \mu\text{m}^2$ . Image reproduced with the permission of G. Ertl. Right (C): Pattern formation in a butterfly wing. Photograph used with permission from the photographer, Muhammad Mahdi Karim [126]. Images from panels (A) and (C) appeared on Wikipedia in addition to the given original citations [127].

numerical simulations.

## 1.4 Basic questions and ideas

In this section I address some basic scientific and philosophical questions and ideas that are implicitly present in this thesis. Here the objective is twofold, firstly to introduce fundamental concepts such as the rationale behind coarse-grained modelling, and secondly to explain the author's motivation for the research presented here, revealing personal bias. By nature, this section is more subjective than the strictly scientific content of the rest of this thesis. Nevertheless, references are provided where possible in order to stimulate further reading and substantiate the arguments presented here.

### 1.4.1 Why study development?

Understanding growth and development is a classic problem in biology, and developmental biology contains questions of both epistemological and immediate practical

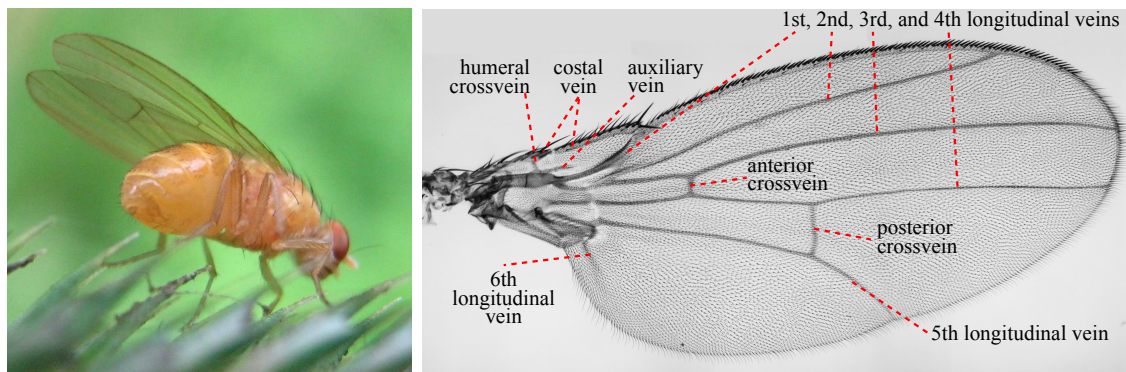


Figure 1.6: Left: The fruit fly *Drosophila melanogaster*. Photograph used with permission from the photographer, Götz Grambow [136]. Right: Fruit fly wing with labelled veins. Experimental image courtesy of Suzanne Eaton.

importance [128]. For instance: How does a single cell give rise to a complex multicellular organism? Connections between biology, chemistry, and physics have both stimulated the application of physical and chemical theories to problems in biology, and also driven the development of the theories themselves. For example, nonlinear dynamics are ubiquitous in chemistry, physics, and biology and are linked with complex pattern formation [129–131]. Turbulent flow in fluids is associated with nonlinearity in the Navier-Stokes equation [132, 133], and oscillatory patterns in reacting and diffusing chemicals result from instability and nonlinearity in the underlying kinetics [129], see Fig. 1.5. Along these lines, A. Turing applied the theory of reacting and diffusing chemical species to pattern formation during development [134]<sup>3</sup>. The general problems of nonlinear dynamics and pattern formation are thus closely linked between physics, chemistry, and developmental biology. Furthermore, living organisms are open thermodynamic systems far from equilibrium [129]. Indeed, no living matter would survive the long-time limit, or thermodynamic isolation. Rather, thermodynamics requires that living systems consume energy to establish and maintain order [129]. Describing ordered systems in far-from-equilibrium conditions, Nicolis and Prigogine stated: “structures that appear in this way are radically different from the ‘equilibrium structures’ studied in classical thermodynamics” [129].

<sup>3</sup>Note that nonlinear terms were not included in Turing’s original paper [134]. Indeed, the Turing instability can be derived using linear stability analysis alone. However, nonlinearities are necessary to bound the exponential growth of unstable modes, and also in order to determine which pattern is selected or favoured following an instability [134, 135].

### 1.4.2 The fly wing as a model system

This thesis deals in general with the biophysics of tissues. Epithelia are thin tissues such as mammalian skin or the wing of a fruit fly <sup>4</sup>. In this thesis we choose the wing of the fruit fly *Drosophila* as a model system, see Fig. 1.6. The motivation for restricting our attention to epithelia is twofold: Firstly, the formation of epithelia is in itself an important situation. Secondly, choosing a primarily two-dimensional model system results in significant simplifications in the resultant theories of cell division, death, mechanics, and dynamics. From a theoretical point of view, any particular model organism is equally well suited for forming a general understanding of tissue mechanics and dynamics. We choose the *Drosophila* wing as a model system in order to benefit from and to contribute to the wealth of genetic knowledge surrounding this organism.

### 1.4.3 Simplified models as tools

Coarse-grained descriptions are used throughout this thesis: we do not attempt to capture the intricacies of a real fly wing. The purpose of building simplified models is to identify and understand underlying physical processes that are also present in real systems. For example, continuum mechanics operates by shedding the burden of discrete structure on the atomic scale. Such simplified models are not improved by the introduction of additional details. Indeed, the notion of improving such a model is in itself ill-defined. Success or failure is defined with respect to a particular set of goals, and the objective of science as presented in this thesis is to understand physical systems.

### 1.4.4 Multi-scale theories

Multi-scale modelling is a key concept for understanding tissues. Here the idea is to formulate descriptions of tissues at different length scales, with the objective to form a consistent picture bridging all scales. On smaller length scales cells are identifiable as discrete units, and must be treated so theoretically. Although microscopic dynamics can be seen to give rise to macroscopic phenomena, microscopic theories are often not the best way to understand macroscopic phenomena. Understanding cell flow by individually discussing the motions of thousands of individual cells is probably not the most economic or enlightening approach. Rather, theory at longer length scales provides additional insights by discarding irrelevant details. Thus, it is helpful to describe tissues on large length scales as continuous materials, averaging out heterogeneity on the scale of single cells. In general, different models may be helpful for understanding different aspects of a given system. Models at

---

<sup>4</sup>More specifically, mammalian skin is composed of multiple layers including the so-called hypodermis, dermis, and epidermis; the epidermis is a prototypical epithelium. The *Drosophila* wing is composed of two epithelial layers.

small length scales are helpful for understanding microscopic details and discrete events, and also for understanding how discrete behaviour at the cell-scale gives rise to large-scale behaviour. Conversely, models at large length scales are helpful for studying collective phenomena, and for determining the continuum limits expected in small-scale models. A complete understanding of the system is obtained by requiring that small- and large-scale models be consistent, for example by deriving large-scale models from small-scale counterparts [32]. In this way, the maximum information about a system is obtained at each level of detail, without sacrificing the scientific rigour or conceptual advantage of possessing a single, complete picture describing the system at all scales.

### 1.4.5 Collective phenomena, self-organization, and emergence

Collective phenomena, self-organization, and emergence are general concepts connecting biology, chemistry, physics, and the present thesis. Collective phenomena result from the combined behaviour of many agents, for example, the collective motion of a school of fish [137], or a collective excitation of electrons (plasmon) in a solid [138]. Self-organization refers to processes where parts of the overall system are not centrally controlled [137, 139, 140]. For example, the aforementioned school of fish is probably self-organized [137], in a mechanism where individual fish move in coordination with their neighbours, as opposed, e.g., to having all the fish in the school follow a leader. Emergence is an extremely broad idea described by the Stanford Encyclopedia of Philosophy as “a notorious philosophical term of art” [141]. The essential idea behind emergence is that parts of a system can combine to give rise to some behaviour that is not obvious from looking at the parts themselves. In the context of the mechanics and dynamics of tissues, tissue-scale behaviour emerges from the collective behaviour of individual cells. Tissue-scale properties may or may not be self-organized, depending on whether cells coordinate using some external global cue, or strictly using interactions internal to the tissue. The ideas of collective phenomena, self-organization, and emergence are not directly employed as scientific theories in this thesis. However, these related concepts should explain to the reader why biology can indeed be tackled using the tools of theoretical physics, albeit with some difficulty. Furthermore, these concepts provide the general context to understand the necessity and utility of using simplified and multi-scale models.

## 1.5 Contents of this thesis

In this thesis we present a theoretical analysis of the vertex model, and a theoretical description of planar cell polarity (PCP). These theoretical analyses build off and contribute to the literature surrounding the vertex model and PCP. The remainder of this thesis is structured as follows: In Chapter 2 we present a definition of the vertex model and an analytical derivation of the ground state diagram. In Chap-

ter 3 we discuss topological processes in the vertex model, such as cell-boundary rearrangements and cell division, and present methods and results for simulating tissue growth. We present in Chapter 4 an extension of the vertex model designed to go beyond the so-called quasistatic approximation, which is used in Chapter 3 and in other vertex-model studies. In Chapter 5 we shift our focus to make closer contact with experiment, presenting theoretical methods and results for quantifying and subsequently visualizing experimental data. In particular, we present in Sect. 5.1 a quantification for cell flow fields and their derivatives, and we present in Sect. 5.2 a quantification for planar cell polarity (PCP). In Chapter 6 the ideas motivated by the quantifications of Chapter 5 are developed into a consistent PCP theory, including in Sect. 6.1 a theoretical analysis of the interaction between cell flow and polarity reorientation. All topics of this thesis are unified in Sect. 6.2 in a cell-scale model of PCP based on the vertex model. The thesis concludes in Chapter 7 with a discussion of what has been achieved and suggestions for future work.

## 2 Vertex model for mechanics and dynamics of epithelia

In the present chapter, we introduce a vertex model in terms of a potential energy or work function and subsequently derive the ground states of the model using analytical arguments. We discuss the effects of external pressure on the ground state diagram, and present elastic properties of the ground states including shear and compression moduli. Knowledge of the ground state diagram and analytical methods for its determination help to understand the forces acting on real tissues. The specific vertex model introduced in this chapter, and used throughout this thesis, first appeared in [69] and [71]. The results presented here build off are refine those presented in [69, 71]. In the remainder of this thesis, we refer to the particular vertex model under study as “the vertex model”. For a discussion of other vertex models, see Sect. 1.2.

### 2.1 Potential energy or work function

The geometry of the polygonal network is described by a set of vertex positions  $\mathbf{r}_i$ , with  $i = 1, \dots, N_V$ , where  $N_V$  denotes the number of vertices, together with bonds  $k$  that connect pairs of vertices. Each polygon describes one cell, indexed by  $\alpha = 1, \dots, N$ , where  $N$  is the number of cells in the system. The mechanical properties of the network in stationary conditions are described by a potential or work function:

$$F(\mathbf{r}_i) = \sum_{\alpha} \frac{K_{\alpha}}{2} (A_{\alpha} - A_{\alpha}^{(0)})^2 + \sum_k \Lambda_k l_k + \sum_{\alpha} \frac{\Gamma_{\alpha}}{2} L_{\alpha}^2. \quad (2.1)$$

Here,  $A_{\alpha}$  denotes the area of cell  $\alpha$ ,  $L_{\alpha}$  is the cell perimeter and  $l_k$  is the length of bond  $k$ . The first term describes area elasticity, where the sum is over all cells  $\alpha$ . If the polygonal area  $A_{\alpha}$  of a cell with constant volume  $V = A_{\alpha}h$  is changed, the cell height  $h$  adjusts. Under such a deformation the elastic energy can be described by an area elastic modulus  $K_{\alpha}$  and a preferred area  $A^{(0)}$ . The second term describes bond tension  $\Lambda_k$ , where the sum is over all bonds  $k$ . This tension results from actomyosin contractility in the cortical bundles associated with the adherens junctions, and also from the mechanics of cell-cell adhesion. In a general expansion of the work

function in terms of vertex positions, higher order terms in bond lengths appear. We introduce as a specific choice of a quadratic term the perimeter elasticity described by the coefficient  $\Gamma_\alpha$ . This term accounts for changes in bond tension due to a change in cell perimeter. It is motivated by the fact that an actomyosin ring underlies the adherens junctional network, which is in general expected to exert a tension depending on cell perimeter.

Of particular theoretical interest is the case where all cells have the same properties, i.e., they all have a common preferred area  $A_\alpha^{(0)} = A_0$ , perimeter stiffness  $\Gamma_\alpha = \Gamma$ , area stiffness  $K_\alpha = K$ , and all bonds have the same line tension  $\Lambda_k = \Lambda$ . This special case is still relevant to comparisons with experiment [69, 71], is somewhat tractable analytically, and serves as the reference for situations with inhomogeneous tissue parameters. In this situation the dimensionless potential energy per cell  $\bar{F} = F/(NKA_0^2)$  can be written as

$$\bar{F} = \frac{1}{N} \sum_{\alpha} e(a_{\alpha}, p_{\alpha}) \quad (2.2)$$

with

$$e(a, p) = \frac{1}{2} [(a - 1)^2 + \bar{\Lambda}p + \bar{\Gamma}p^2] \quad (2.3)$$

$$= \frac{1}{2} [(a - 1)^2 + \bar{\Gamma}(p - p_0)^2] + e_0, \quad (2.4)$$

where  $a_\alpha = A_\alpha/A_0$  and  $p_\alpha = L_\alpha/\sqrt{A_0}$ . Dimensionless bond lengths are similarly defined as  $\ell_k = l_k/\sqrt{A_0}$ . The model parameters are represented as  $p_0 = -\bar{\Lambda}/2\bar{\Gamma}$ , which is a dimensionless preferred perimeter and  $e_0 = -\bar{\Lambda}^2/8\bar{\Gamma}$ , where  $\bar{\Lambda} = \Lambda/(KA_0^{3/2})$  and  $\bar{\Gamma} = \Gamma/(KA_0)$ . In writing Eq. 2.4 we have made use of the choice that all bonds have the same line tension  $\Lambda_k = \Lambda$ , so that line tension can be absorbed in the perimeter term by introducing  $p_0$ . Changes in area  $\delta a$  and perimeter  $\delta p$  imply a change in potential:

$$\delta e = (a - 1)\delta a + \bar{\Gamma}(p - p_0)\delta p + \frac{1}{2}(\delta a^2 + \bar{\Gamma}\delta p^2). \quad (2.5)$$

If a cell has  $a = 1$  and  $p = p_0$  then the potential of that cell  $e = e_0$  is at the absolute minimum of  $e$ .

## 2.2 Ground states

Here we systematically determine the ground states of the vertex model. Ground states can be interpreted as being the most relaxed network configurations. They are the absolute minima of  $F$  for a given number of cells  $N$ , using periodic boundary conditions for simplicity. The size of the periodic box is given by the lengths  $L_x$  and

Perimeter	Area	Properties of $e(a, p)$	Geometric constraint on $(a, p)$
$p > p_0$	$a < 1$	potential minimum is a regular polygon	none
$p = p_0$	$a = 1$	this is the absolute potential minimum	$\bar{\Lambda} \leq -4\bar{\Gamma}\sqrt{n \tan(\pi/n)}$
$p = 0$	$a = 0$	potential minimum is a collapsed cell	$\bar{\Lambda} \geq (2/c)[(2c - \bar{\Gamma})/3]^{3/2}$ ( $\bar{\Gamma} < 2c$ ) $\bar{\Lambda} \geq 0$ ( $\bar{\Gamma} \geq 2c$ )
$p < p_0$	any $a$	potential can be reduced by increasing perimeter	none
$p = p_0$	$a \neq 1$	potential can be reduced by uniform scaling	none
$p > p_0$	$a \geq 1$	potential can be reduced by uniform compression	none

Table 2.1: Geometric constraints limit the values of the dimensionless perimeter  $p$  and area  $a$  that are possible for a polygonal cell. These constraints are listed in the rightmost column. Given a set of  $(a, p)$  (first and second columns), a corresponding polygon may or may not be a minimum of  $e$ , as indicated in the third column.

$L_y$ . We consider the case where all cells have the same properties, and represent the potential  $F$  using the dimensionless potential energy per cell  $\bar{F}$ .

First, we determine minimal potential configurations of single polygons. We then construct lower bounds of  $\bar{F}$  for arbitrary polygonal lattices and compare them to  $\bar{F} = e_6$  for hexagonal lattices and to the value  $\bar{F} = 1/2$  of a collapsed network ( $a_\alpha = 0, p_\alpha = 0$ ). In this way we determine regions in parameter space where different types of ground-state networks exists, see Fig. 2.1.

### 2.2.1 Polygons of minimal potential

First we determine the shape corresponding to the global minimum of the potential  $e(a, p)$  of a single polygon with a fixed number of sides  $n$ . We identify several cases depending on the values of  $a$  and  $p$ , see Table 2.1. An optimal polygon with  $a > 0$  must obey  $\partial e' / \partial \chi|_{\chi=1} = 0$ , where

$$e' = \frac{1}{2} [(\chi^2 a - 1)^2 + \bar{\Gamma}(\chi p - p_0)^2 + e_0] \quad (2.6)$$

is the potential of a polygon rescaled by a factor  $\chi = 1 + \epsilon$ . This condition implies

$$2a(a - 1) + \bar{\Gamma}p(p - p_0) = 0. \quad (2.7)$$

Thus, we distinguish three cases of possible minima of  $e$ : (i)  $p < p_0$  and  $a > 1$ , (ii)  $p = p_0$  and  $a = 1$ , and (iii)  $p > p_0$  and  $a < 1$ . The first case (i) is unstable with respect to shear, because  $\partial e/\partial p|_a = \bar{\Gamma}(p - p_0) < 0$  and it is always possible to increase the perimeter of a polygon at fixed area. Case (ii) corresponds to an absolute minimum of  $e$ , at which both area and perimeter take their preferred values. This is possible only if  $p_0$  is equal to or larger than the minimal perimeter of an  $n$ -sided polygon of unit area, which leads to the condition:

$$\bar{\Lambda} \leq -4\bar{\Gamma}\sqrt{n \tan\left(\frac{\pi}{n}\right)}. \quad (2.8)$$

In the limit of large  $n$  Eq. 2.8 becomes:

$$\bar{\Lambda} < -4\sqrt{\pi}\bar{\Gamma}. \quad (2.9)$$

In case (iii), the optimal shape is either a regular  $n$ -sided polygon or a collapsed cell ( $a = 0$ ,  $p = 0$ ). For  $p > p_0$ ,  $\partial e/\partial p|_a > 0$ , thus reducing the perimeter at fixed area reduces the potential. A regular  $n$ -sided polygon has a smaller perimeter than any irregular  $n$ -sided polygon with equal area. Thus if  $p > 0$  the optimal shape is a regular  $n$ -sided polygon. A special case is a collapsed cell with  $a = 0$ ,  $p = 0$ , and  $e = 1/2$ . For regular polygons  $a = cp^2$  where  $c = \cot(\pi/n)/4n$ . The potential is

$$e(p) = \frac{1}{2} [(cp^2 - 1)^2 + p\bar{\Lambda} + p^2\bar{\Gamma}]; \quad (2.10)$$

the stationarity condition  $de(p)/dp = 0$  provides the relation

$$4c^2p^3 + (2\bar{\Gamma} - 4c)p + \bar{\Lambda} = 0. \quad (2.11)$$

Combining Eq. 2.11 with the inequality  $e > 1/2$ , we obtain the condition for polygonal collapse:

$$\begin{aligned} \bar{\Lambda} &\geq \frac{2}{c} \left( \frac{2c - \bar{\Gamma}}{3} \right)^{3/2} && (\bar{\Gamma} < 2c) \\ &\geq 0 && (\bar{\Gamma} \geq 2c). \end{aligned} \quad (2.12)$$

In the limit of large  $n$  Eq. 2.12 becomes:

$$\begin{aligned} \bar{\Lambda} &\geq \frac{8}{\sqrt{\pi}} \left( \frac{1 - 2\pi\bar{\Gamma}}{3} \right)^{3/2} && (2\pi\bar{\Gamma} < 1) \\ &\geq 0 && (2\pi\bar{\Gamma} \geq 1). \end{aligned} \quad (2.13)$$

Note that, as will be shown in Sect. 2.2.2, Eq. 2.8 and Eq. 2.12 define characteristic boundary lines in the ground-state diagram of the vertex model, see Fig. 2.1a.

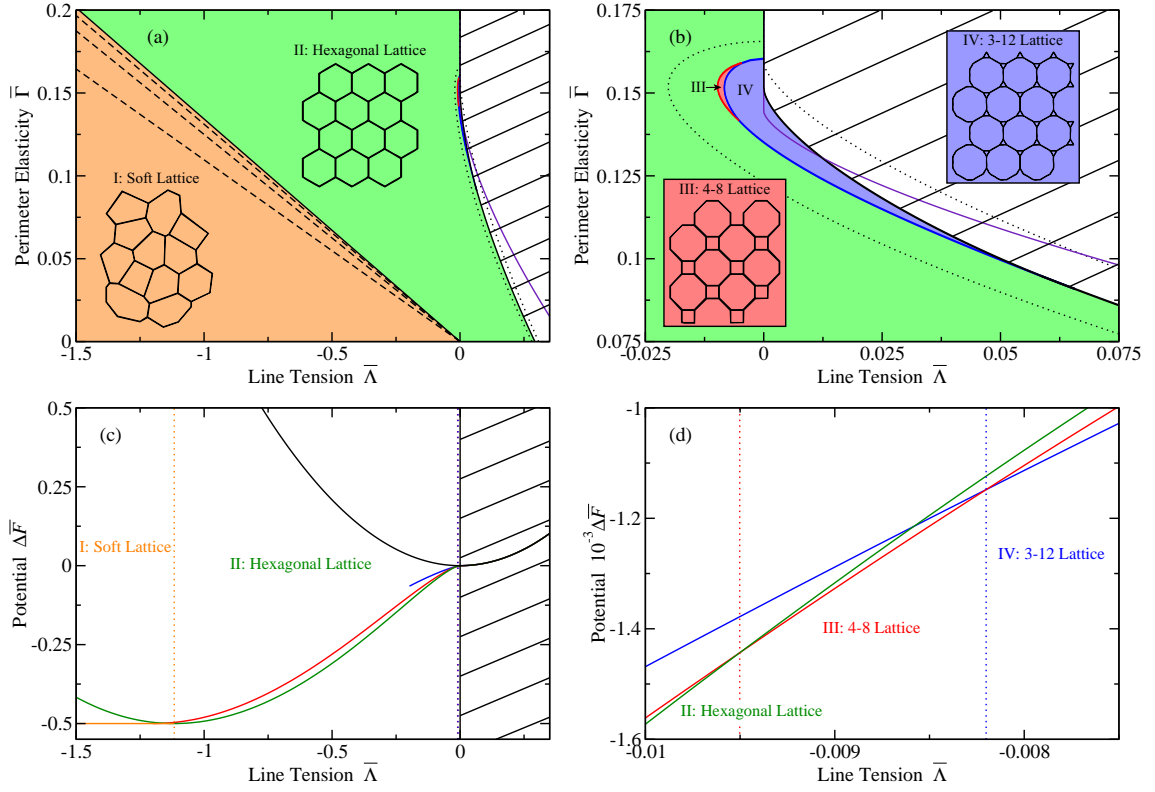


Figure 2.1: (a) The ground-state diagram of the vertex model. In region (I) (orange) the ground states are degenerate and correspond to primarily irregular networks, in which all cells have equal perimeter  $p = p_0$  and equal area  $a = 1$ . Within this region, dashed lines (described by Eq. 2.8 for  $n = 3, 4$ , and  $5$ ) separate subregions with varying degrees of degeneracy. In these subregions the ground state is composed of irregular polygons with (from left to right)  $n \geq 3$  sides,  $n \geq 4$  sides,  $n \geq 5$  sides, and  $n = 6$  sides, respectively. The solid line separating region (II) where the regular hexagonal lattice is the ground state is described by Eq. 2.8 with  $n = 6$ . Within the hatched region the ground state is a collapsed lattice of cells with zero area. (b) The region enclosed by the two dotted lines in (a) is magnified. Two additional regions (III) (red) and (IV) (blue) can be identified, where a “4-8” lattice and “3-12” lattice, respectively, have lower energies than the regular hexagonal lattice. The violet line indicates where the hexagonal lattice becomes locally unstable. In the region outside of the two dotted lines the nature of the ground state can be shown rigorously. (c) Diagrams of the potential energy per cell  $\Delta\bar{F} = \bar{F} - e_0 - 1/2$  of different lattices, as a function of normalized line tension  $\bar{\Lambda}$  for  $\bar{\Gamma} = 0.15$ . Intersections of  $\Delta\bar{F}$  for different lattices are marked by dotted lines. The lowest energy (orange) corresponds to soft lattices, which exist in region (I) for  $\bar{\Lambda} \lesssim -1.12$ . The energy of the hexagonal lattice (green) has minimal energy in region (II). The energy of collapsed lattices with zero area is indicated by the black line, and minimizes the energy in the hatched region. Furthermore, the energies of 4-8 and 3-12 lattices are indicated in red and blue, respectively. (d) Magnification of a small region of line tension of the energy diagram shown in (c), highlighting the regions where new periodic lattices have minimal energy.

## 2.2.2 Networks of minimal potential

In Sect. 2.2.1 we showed that the potential energy  $e(a,p)$  of an individual cell is minimized by regular  $n$ -sided polygons. Here we determine ground-state networks, defined as the configurations of polygons that minimize the potential  $\bar{F}$  for a given set of parameter values  $\bar{\Lambda}$  and  $\bar{\Gamma}$  with periodic boundary conditions. The size of the periodic box is also varied in the minimization. This minimization problem is solved by using the minimal energy polygons described in the last section together with the fact that the average neighbour number is less than or equal to six. Note that in periodic networks containing only threefold vertices the average neighbour number is exactly six. In periodic networks containing manyfold vertices, the average neighbour number is less than six. Details of the determination of ground states and the corresponding ground-state diagram are presented in App. A.

In Figs. 2.1a and 2.1b we present the ground-state diagram of the vertex model. We find four distinct regions of parameter space ( $\bar{\Lambda}$  and  $\bar{\Gamma}$ ): (I) irregular networks are the (degenerate) ground states, (II) the ground state is a hexagonal lattice, and two further regions (III) and (IV), where other periodic lattices are the ground state. In the hatched region the ground state is a collapsed network of cells with zero area. Region (I) is bounded by a straight line described by Eq. 2.8 for  $n = 6$ . Region (I) can be further divided into four subregions (separated by dashed lines in Fig. 2.1a), characterized by the degree of degeneracy of the ground states. From right to left the ground states in the four subregions are composed of irregular  $n$ -sided polygons with  $n = 6$ ,  $n \geq 5$ ,  $n \geq 4$ , and all  $n$ , respectively. They are obtained from Eq. 2.8 for  $n \leq 6$ . The region inside of the dotted lines is highlighted in Fig. 2.1b. Outside of this region, the state diagram is known exactly, see App. A. The dotted line within the hatched region is given by Eq. 2.13, while the dotted line within region (II) is determined in App. A. Between these dotted lines we find two small regions (III) (red) and (IV) (blue) where two new periodic lattices have a lower energy than the hexagonal lattice, see Fig. 2.1. These regions were identified numerically by comparing the minimized energies of various periodic tilings of the plane. Furthermore, we show in Fig. 2.1b a violet line, showing the limit of local stability of the hexagonal network.

The energy of different periodic network configurations is shown in Figs. 2.1c and 2.1d as a function of  $\bar{\Lambda}$  for  $\bar{\Gamma} = 0.15$ . The energy of soft lattices in region (I) is constant and the corresponding line (orange) exists for  $\bar{\Lambda} \lesssim -1.12$ , up to the dotted line in Fig. 2.1c. The energy of hexagonal lattices is indicated in green, while those of periodic “4-8” and “3-12” lattices are shown in red and blue, respectively. Note that the blue line only exists for  $\bar{\Lambda} \gtrsim -0.20$ . The black line shows the energy of collapsed cells of zero area. The energy branch of soft lattices (orange) meets the energy of the hexagonal lattice (green) at a point where the energy of the hexagonal lattice has zero slope, indicative of a second order transition, see Fig. 2.1c. The transitions between regions (II), (III), and (IV), however, are first order transitions because the different branches have different slopes, see Fig. 2.1d.

## 2.3 Effects of external pressure

The effects of external pressure  $\sigma$  can be incorporated into the dimensionless potential energy per cell  $\bar{F}$  by adding a dimensionless potential energy  $a\sigma$  to the potential of an individual cell  $e(a, p)$ . Under this modification, Eq. 2.4 becomes:

$$e(a, p) = \frac{1}{2} [(a - 1)^2 + \bar{\Lambda}p + \bar{\Gamma}p^2] + a\sigma. \quad (2.14)$$

Completing the square and renormalizing, the effect of external pressure  $a\sigma$  can be combined with the other terms in Eq. 2.14 yielding the equation:

$$\tilde{e}(\tilde{a}, \tilde{p}) = \frac{1}{2} [(\tilde{a} - 1)^2 + \tilde{\Lambda}\tilde{p} + \tilde{\Gamma}\tilde{p}^2] + \Delta\tilde{e}, \quad (2.15)$$

where  $\tilde{e} = e/(1 - \sigma)^2$ ,  $\tilde{a} = a/(1 - \sigma)$ ,  $\tilde{p} = p/\sqrt{1 - \sigma}$ ,  $\tilde{\Lambda} = \bar{\Lambda}/(1 - \sigma)^{3/2}$ ,  $\tilde{\Gamma} = \bar{\Gamma}/(1 - \sigma)$ ,  $\Delta\tilde{e} = [1/(1 - \sigma^2) - 1]/2$ , and we have assumed  $\bar{\Lambda} \neq 0$ . Thus, external pressure can be accounted for in a rescaling of model parameters  $\bar{\Lambda}$  and  $\bar{\Gamma}$ , together with a rescaling of the dimensionless areas  $a$  and perimeters  $p$ , leaving the ground-state diagram otherwise unchanged. As dimensionless pressure  $\sigma$  is changed, the system moves on a path in the ground-state diagram with effective parameters  $\tilde{\Lambda}$  and  $\tilde{\Gamma}$

$$\tilde{\Lambda} = \frac{\bar{\Lambda}}{(1 - \sigma)^{3/2}} \quad (2.16)$$

$$\tilde{\Gamma} = \frac{\bar{\Gamma}}{1 - \sigma}, \quad (2.17)$$

where  $\bar{\Lambda}$  and  $\bar{\Gamma}$  are the dimensionless line tension and dimensionless perimeter elasticity in the absence of external pressure as defined in Sect. 2.1.

Eq. 2.16 points out that as external pressure  $\sigma$  is increased, the magnitude of the effective line tension  $\tilde{\Lambda}$  increases. If  $\bar{\Lambda} < 0$  this suggests that for sufficiently large  $\sigma$  it might be possible to force a transition from the region where a hexagonal lattice is the ground state of the vertex model (green region of Fig. 2.1a) to the region where irregular lattices are the ground states of the vertex model (orange region of Fig. 2.1a). Such transitions are indeed observed in simulations, see Fig. 2.2. Conversely, if  $\bar{\Lambda} > 0$  then increasing pressure will eventually force a transition to the region where a collapsed lattice of zero area is the ground state of the vertex model (hatched region in Fig. 2.1a).

## 2.4 Shear and compression moduli

Here we discuss the shear and compression moduli of the ground states of the vertex model. For fixed cell number  $N$  and box dimensions  $L_x$  and  $L_y$  we define the

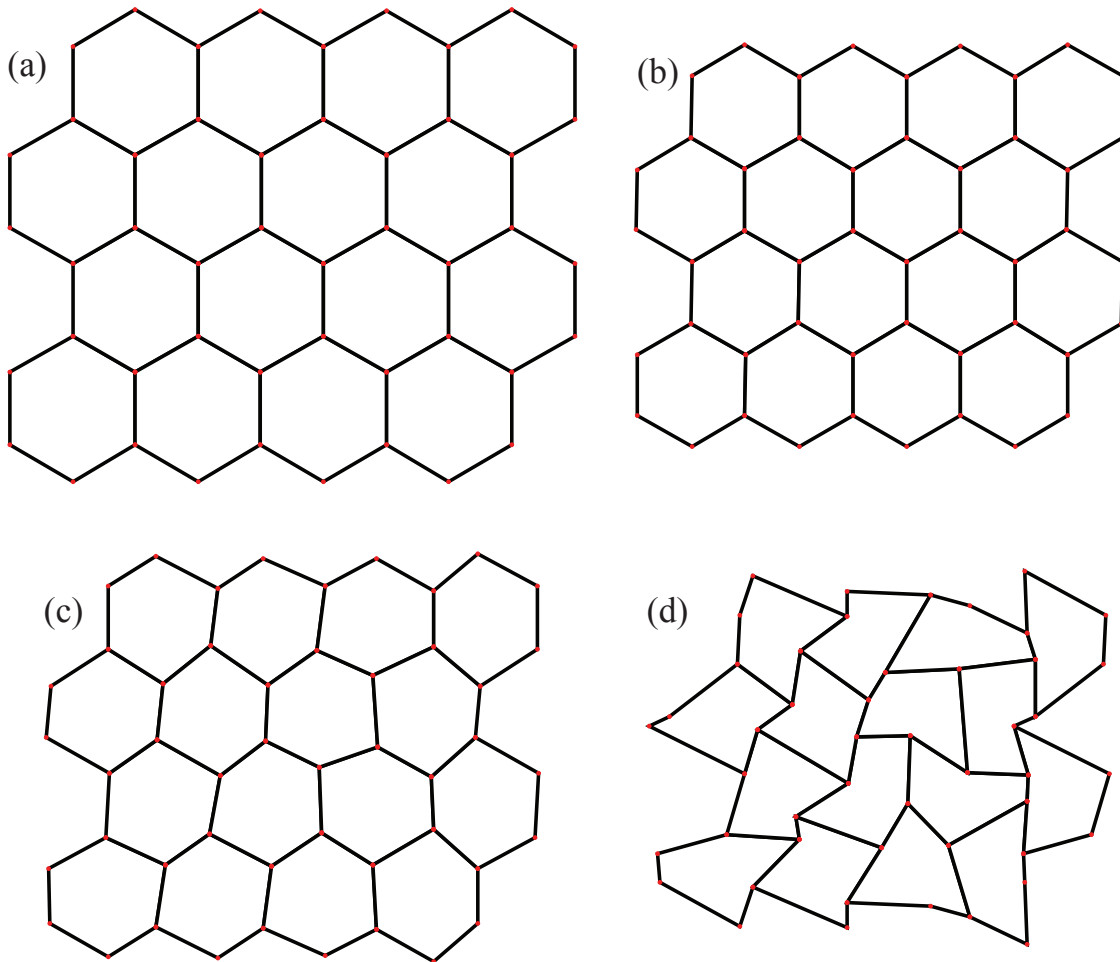


Figure 2.2: Calculation results showing a forced transition from a hexagonal state to an irregular lattice via the application of external pressure. In all panels, parameter values  $\bar{\Lambda} = -0.25$ ,  $\bar{\Gamma} = 0.04$  were chosen to be close to the transition line. (a) For zero pressure,  $\sigma = 0$ , the potential  $\bar{F}$  is minimal for a network of regular hexagons. (b) For dimensionless pressure  $\sigma = 0.3$ , the potential is still minimal for a network of regular hexagons, although the size of hexagons in the ground state has been reduced. (c) Increasing the pressure slightly further, to  $\sigma = 0.302$ , forces a transition to a network of deformed hexagons. (d) For  $\sigma = 0.5$  the network is massively deformed and contains convex cells.

minimum of the potential  $F$  by the function  $F(L_x, L_y)$ . The shear modulus  $\mu$  can then be obtained as:

$$\mu = \frac{1}{2A} \left. \frac{\partial^2 F(L_x, L_y)}{\partial \gamma^2} \right|_{\gamma=0}, \quad (2.18)$$

where  $A = L_x L_y$ ,  $L_x = L_x^{(0)}(1 + \gamma)$ , and  $L_y = L_y^{(0)}/(1 + \gamma)$ . Here,  $L_x^{(0)}$  and  $L_y^{(0)}$  define the size of a reference box and  $\gamma$  is a dimensionless rescaling parameter. Similarly, the compression modulus  $\lambda$  can be obtained as

$$\lambda = \frac{1}{4A} \left. \frac{\partial^2 F(L_x, L_y)}{\partial \epsilon^2} \right|_{\epsilon=0}, \quad (2.19)$$

where  $L_x = L_x^{(0)}(1 + \epsilon)$  and  $L_y = L_y^{(0)}(1 + \epsilon)$ . In the region where the ground state is a hexagonal lattice the network has both nonzero shear and compression moduli:

$$\begin{aligned} \bar{\mu} &= (\sqrt{3}/16)p^2 + 2\sqrt{3}\bar{\Gamma} - 1/2 \\ \bar{\lambda} &= 6\sqrt{3}\bar{\Gamma} + 3\sqrt{3}\bar{\Lambda}/p, \end{aligned} \quad (2.20)$$

where  $\bar{\lambda} = \lambda/(KA_0)$  and  $\bar{\mu} = \mu/(KA_0)$ .

As line tension and perimeter elasticity are reduced the shear modulus of the network decreases; when the equilibrium perimeter of cells in the hexagonal ground state reaches  $p = p_0$  the shear modulus vanishes, yielding a transition line at  $\bar{\Lambda} = -2^{5/2}3^{1/4}\bar{\Gamma}$ . This is exactly the transition line where the ground state changes from a network of regular hexagons to a degenerate network where all cells have  $a = 1$ ,  $p = p_0$ , and  $e = e_0$ , see Sect. 2.2.2. For line tensions and perimeter elasticity below this transition line, small shear deformations can be performed with no work required, indicative of a transition from a solid to a soft network.

For sufficiently high perimeter elasticity and tension the compression modulus vanishes. Setting  $\lambda = 0$  in Eq. 2.20 yields an instability line for the hexagonal lattice:

$$\begin{aligned} \bar{\Lambda} &= 2^{3/2}3^{-5/2}(\sqrt{3} - 12\bar{\Gamma})^{3/2} & (\bar{\Gamma} < \sqrt{3}/12) \\ &= 0 & (\bar{\Gamma} \geq \sqrt{3}/12). \end{aligned} \quad (2.21)$$

This line lies primarily in the hatched region of the state diagram, see the violet line in Fig. 2.1. For points in the phase diagram beyond this line hexagonal networks are unstable. This instability is reflected in Eq. 2.11, which has no real positive roots  $p \geq 0$ ,  $p \in \mathbb{R}$  for hexagonal lattices ( $n = 6$ ,  $c = \sqrt{3}/24$ ) beyond the violet line.

## 2.5 Summary

In this chapter we presented a vertex model for cell mechanics based on a potential energy or work function. We chose for a potential energy the same form as was presented in [69, 71], with the motivation that this specific version of the vertex model

is being applied to study processes such as cell packing [69, 71], cell sorting [76], planar cell polarity [2], and the dynamics of growth control and morphogen scaling [78, 79]. However, the analytical arguments presented in this chapter do not depend on the specific functional form chosen for the potential energy. The derivation of the ground-state diagram could be repeated for different vertex models, and the methods presented here are general in this sense. In particular, we find that the ground state diagram of the vertex model is dominated by the geometric requirement that cells be polygons, and the topological requirement that these polygons must form a contiguous network. We find that external pressure can be incorporated as a rescaling of model parameters, leaving the ground state diagram otherwise unchanged. Finally, we present shear and compression moduli for the hexagonal lattice, relating critical values of these elastic moduli to transitions in the ground-state diagram of the vertex model.

# 3 Topological processes and tissue growth

The ground state is an important reference state for cellular networks, representing the most relaxed configuration. Network configurations that correspond to cell packings in tissues in general do not correspond to ground states. Active processes such as cell division and morphogenetic movements perform mechanical work, and thus generate network configurations that are of higher potential energy than the ground state. However, these configurations are force-balanced, and thus local minima of the potential  $F$  [69]. The large number of such local minima are physiologically relevant, and are generated via topological rearrangements of the network. Such topological changes are often associated with energy barriers. Here we discuss three types of topological transitions, namely T1 transitions, T2 transitions, and cell division. A T1 transition occurs when a cell boundary shrinks to zero length, forming a fourfold vertex, which subsequently decomposes, creating a new cell bond [142]. This process changes neighbourhood relationships, see Fig. 3.1. A T2 transition occurs when a  $n$ -sided polygon shrinks to a point and is replaced with an  $n$ -fold vertex, see Fig. 3.2. Such a T2 transition corresponds to cell extrusion from an epithelium, typically associated with cell death (apoptosis).

## 3.1 Energetics of manifold vertices

The energetics of manifold vertices in the vertex model are relevant for the dynamics of boundary rearrangements, i.e. T1-transitions. A manifold vertex is unstable if

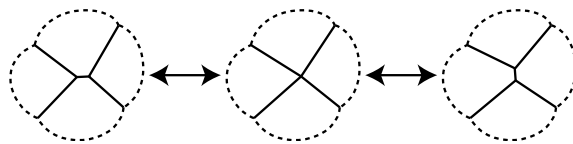


Figure 3.1: Schematic of a network rearrangement called a T1 transition. Two threefold vertices combine to form a fourfold vertex, which subsequently decomposes into two new threefold vertices. The overall topology of the network is changed during this process, and cells change their neighbourhood relation.

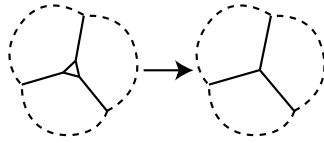


Figure 3.2: Schematic of a network rearrangement called a T2 transition. A cell shrinks to zero area and is removed from the lattice. This process corresponds to the extrusion of a cell from an epithelium (apoptosis).

there exists a decomposition into infinitesimally separated threefold vertices that lowers the potential  $F$  of the network. For example, a fourfold vertex can be replaced by two threefold vertices in two topologically different ways, see Fig. 3.1. Our work suggests that manyfold vertices are unstable if all cells are equivalent (common values of  $A_0$ ,  $\Lambda$ ,  $\Gamma$ , and  $K$ ), unless  $a = 1$  and  $p = p_0$ . A general proof of this statement is lacking, but it holds true for any case investigated.

Consider for example the case where cells meeting at a fourfold vertex have equal area  $a \neq 1$  and equal perimeter  $p \neq p_0$ . If a fourfold vertex decomposes into two threefold vertices then the total energy change is:

$$\delta\bar{F} = \frac{1}{N} \sum_{\alpha} [(a_{\alpha} - 1)\delta a_{\alpha} + \bar{\Gamma}(p_{\alpha} - p_0)\delta p_{\alpha}], \quad (3.1)$$

plus terms of order  $\delta a_{\alpha}^2$  and  $\delta p_{\alpha}^2$ . Substituting  $a_{\alpha} = a$  and  $p_{\alpha} = p$ , Eq. 3.1 reduces to

$$\delta\bar{F} = \frac{\bar{\Gamma}(p - p_0)}{N} \sum_{\alpha} \delta p_{\alpha}. \quad (3.2)$$

Thus the change in potential during decomposition of a fourfold vertex is proportional to the total perimeter change in this case. There are two topologically distinct ways to decompose a fourfold vertex into two threefold vertices, see Fig. 3.1. For each of these two topologically distinct decompositions, there is a continuum of possible variations, assuming that infinitesimal movements of the resulting threefold vertices are permitted. As a consequence, there always exist many decompositions of a fourfold vertex into threefold vertices, some of which increase and some of which decrease the total perimeter. Thus it is possible to lower the potential of the network by decomposing the fourfold vertex, and the fourfold vertex is always unstable in this case. Finally, if cells are unequal in their mechanical properties then stable manyfold vertices can occur.

## 3.2 Cell extrusion by T2 transitions

Cell extrusion can be discussed in a simple scenario where triangular cells of dimensionless side length  $\ell = l/\sqrt{A_0}$  are introduced at the vertices of a hexagonal network.

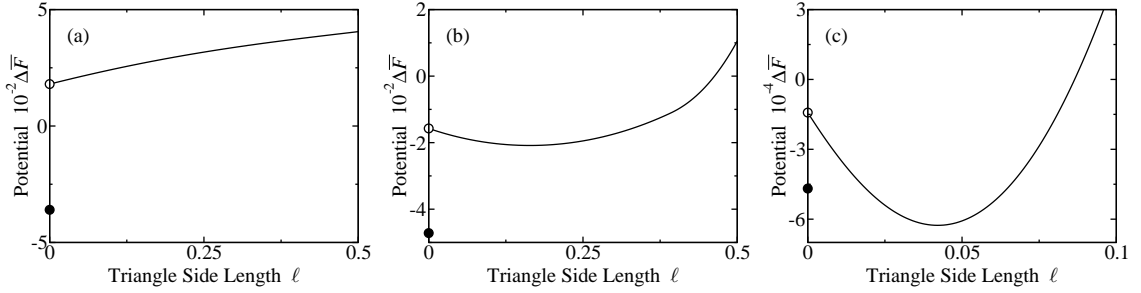


Figure 3.3: Diagrams of the potential energy per cell  $\Delta\bar{F} = \bar{F} - e_0 - 1/2$  of “3-12” lattices, which are hexagonal lattices into which triangular cells are periodically introduced, see Fig. 2.1b. Different parameter values reveal three possible situations: (a) no barrier to cell extrusion (b) a finite barrier to cell extrusions and (c) stable 3-12 lattices in region (IV). Parameter values are  $(\bar{\Lambda}, \bar{\Gamma}) = (0.12, 0.04)$ ,  $(0, 0.1)$ , and  $(-0.005, 0.15)$ , corresponding to (a), (b), and (c), respectively.

The resulting lattice consists of three- and twelve-sided cells, as in region IV of Fig. 2.1. We show in Fig. 3.3 the potential energy per cell of the lattice as a function of the side length  $\ell$  of the triangles. Depending on parameter values we find three distinct behaviours: (a) instability of triangles with respect to spontaneous cell extrusion, (b) locally stable triangles with a barrier to cell extrusion, and (c) globally stable triangles in region IV of Fig. 2.1.

### 3.3 Cell division in the vertex model

In the vertex model, cell division can be introduced by the following steps [69] (algorithm I): (i) Initially the network is in a force-balanced state, i.e. a local minimum of  $F$ . (ii) A cell  $\alpha$  is selected to divide. (iii) The preferred area  $A_\alpha^{(0)}$  of cell  $\alpha$  is doubled quasistatically. (iv) A new cell boundary is introduced bisecting the cell  $\alpha$  into two daughter cells. In the case of isotropic cell division, the new cell bond has a random orientation. We choose it to pass through the center of cell  $\alpha$ , defined as the average of the vertex positions of that cell. (v) The preferred areas  $A_\alpha^{(0)}$  of the daughter cells are reset to the original preferred area of cells. (vi) The system is relaxed to a force-balanced configuration<sup>1</sup>. This relaxation introduces network rearrangements by T1 and T2 transitions. A detailed discussion of the algorithms used to account for topological changes are given in App. B.1.

For simplicity and to improve computational performance, the steps described above can be reduced as follows (algorithm II): (i) Initially the network is in a force-balanced state. (ii) A cell  $\alpha$  is selected to divide. (iii) The cell  $\alpha$  is bisected into

<sup>1</sup>Both here and in Ref. [69] force-balanced states are obtained using the Polak-Ribière variant of the conjugate gradient algorithm [143], e.g., as implemented in the GNU Scientific Library [144].

two daughter cells by inserting a new cell bond. This new cell bond has a random orientation and passes through the geometric center of cell  $\alpha$ . (iv) The system is relaxed to a force-balanced state. We show in App. B.2 that algorithm I and II give very similar results, and that for practical purposes algorithm II is sufficient to describe tissue morphology.

### 3.4 Tissue morphologies generated by growth

Growth simulations are performed by randomly selecting cells with equal probability to divide. A single cell division is performed using algorithm II and the next cell is subsequently selected at random. This implies a quasistatic representation of growth. This process can be related to real time by assigning times to each cell division event. This can be done such that the probability per unit time of each cell to divide, the cell division rate  $k_d$ , is constant. Alternatively, one can describe the process as a function of generation number  $g = \log_2(N/N_0)$ , where  $N$  is the cell number and  $N_0$  is the cell number in the original generation of cells.

We show in Fig. 3.4a polygon class distributions resulting from vertex model simulations using algorithm II (solid line). These data were obtained by performing  $10^4$  simulations, each starting from 16 cells and having  $10^2$  subsequent cell divisions. The errors are smaller than the line width and are thus not indicated. Note that neighbour numbers in the simulations were determined without a cutoff for minimal bond length and therefore the average neighbour number is 6. This data is compared to experimental estimates of neighbour number distributions in the developing wing of the fruit fly *Drosophila* (data from Ref. [69]).

In a series of studies spanning from 1928 to 1950, F. T. Lewis reported an approximately linear relationship between the number of sides and the area of cells of various organisms [145, 146]. This maxim is commonly referred to as Lewis's Law. We present in Fig. 3.4b the area of polygons resulting from simulated growth in the vertex model (algorithm II, solid line) and values reported experimentally (dashed line). Note that our simulations show that the average area exhibits nonlinear behaviour. However, if the same data were presented over a limited range of  $n$  (e.g.  $4 \leq n \leq 8$ ) and with larger error bars, then one might mistakenly identify a linear relationship. Nonlinearities can have several causes, for instance because cells cannot have arbitrarily large areas while the number of neighbours can become large. These nonlinearities are accessible in simulations, where precise statistics are possible. Lewis's Law therefore represents an approximation that is valid for limited ranges of  $n$ .

We also present in Figs. 3.4c and 3.4d the full distributions of polygon area and perimeter. The mean areas  $\langle a \rangle_n$  presented in Fig. 3.4b are the first moments of the distributions shown in 3.4c.

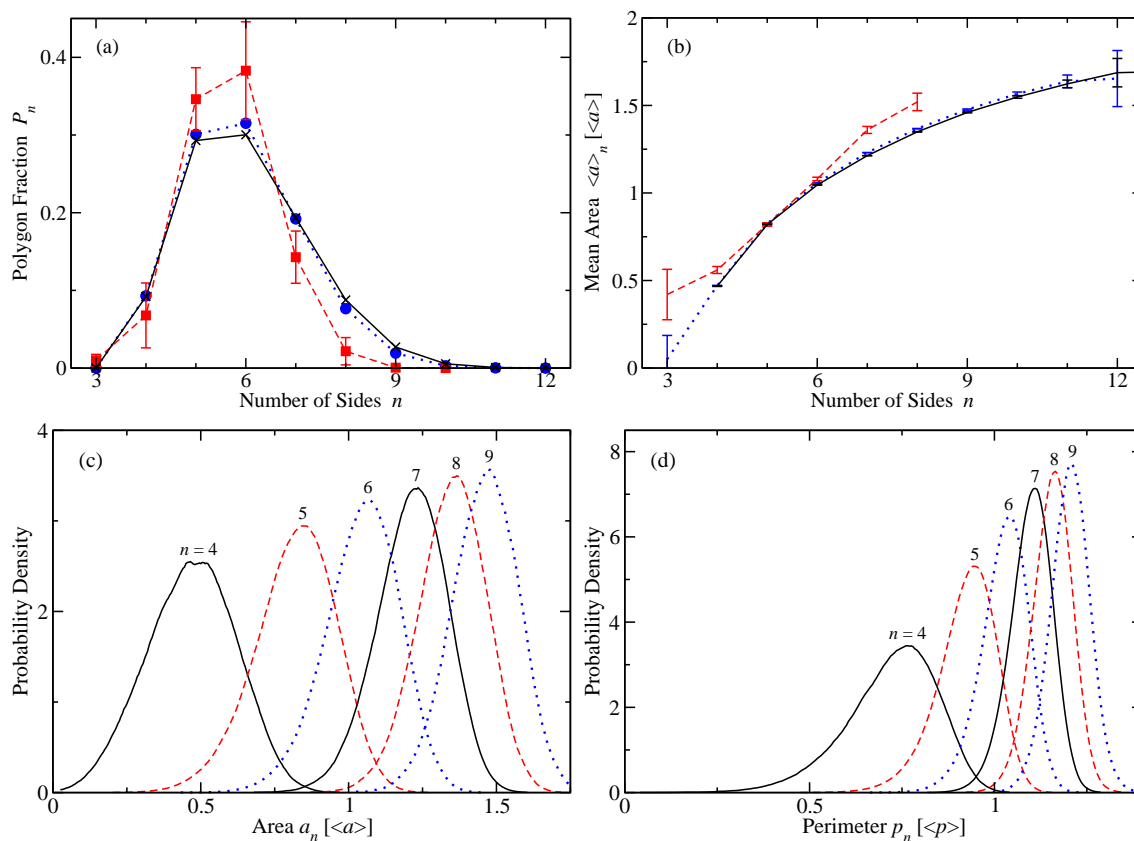


Figure 3.4: (a) Fraction of  $n$ -sided polygons as a function of cell neighbour number  $n$ . Neighbour number distributions are obtained in growth simulations with algorithm II for  $(\bar{\Lambda}, \bar{\Gamma}) = (0.12, 0.04)$  without a length cutoff (black) and with a length cutoff of 20% of the average bond length (blue). Experimental data (red) of the wing of the fruit fly from Ref. [69] is shown for comparison. The length cutoff defines a distance, below which two threefold vertices are considered to be a single fourfold vertex. For each polygon containing one or more edges shorter than the length cutoff, the neighbour number  $n$  is reduced appropriately. (b) Average area of  $n$ -sided polygons, normalized by the average area of cells in the network, for the same simulations and experiments shown in (a). (c) Stationary probability distributions of the areas of  $n$ -sided polygons in the growth simulations with algorithm II that are indicated by solid lines in (a) and (b). (d) Stationary probability distributions of the perimeters of  $n$ -sided polygons in the simulations shown in (c).

## 3.5 Summary

In this chapter we investigated topological changes present in real tissues, including T1 and T2 transitions, cell division, and growth. Here T1 and T2 transitions correspond to cell-boundary rearrangement and cell extrusion, respectively. These transitions arise naturally in vertex model simulations, in the situations where either a bond or a cell vanishes to zero length or area, respectively. During a T1 transition, a four-way or many-way vertex is formed in an intermediate state, see Fig. 3.1. Here we find that four-way vertices are unstable in the vertex model in the case where all cells have identical parameters. With regards to T2 transitions, we find three distinct situations: no barrier to cell extrusions, a finite barrier to cell extrusions, and stable triangular cells in region (IV) of the ground state diagram, see Fig. 3.3.

We presented in Sects. 3.3 and 3.4 an algorithm for simulating tissue growth in the vertex model. This algorithm is a simplified version of that presented in Ref. [69], which gives the same results as that algorithm in the present simulations, see Appendix B.2. These algorithms for tissue growth allow a connection to be made with experiments, see Figs. 3.4a and 3.4b, and can make predictions for future experiments, see Figs. 3.4c and 3.4d and Refs. [2, 69, 76, 78, 79].

## 4 Dynamics beyond the quasistatic approximation

The growth simulations presented in Chapter 3 made use of quasistatic dynamics, which are valid on timescales longer than the mechanical relaxation of the network. However, there are specific situations where the choice of dynamics plays a critical role. In this chapter we discuss the limitations of the quasistatic approximation, and develop an alternative dynamic description based on the balance between reactive and dissipative (frictional) forces. Relaxation modes emerging in this dynamic description are derived analytically using a lattice of square cells. We apply our dynamic description to study the effects of friction on tissue growth, demonstrating that the quasistatic results of Chapter 3 can be obtained in a dynamic calculation in the limit of low friction or slow growth rate.

### 4.1 Limitations of the quasistatic approximation

In simulated laser ablation [69] the network is subjected to an instantaneous perturbation and the response is measured. These simulations are designed to mimic experiments where single cell boundaries are cut with a laser. By definition, the response to such a local perturbation occurs on timescales of mechanical relaxation of the network. Thus, quasistatic simulations of laser ablation cannot capture the dynamics of the process, and can only be compared to experiments in terms of long-time behaviour. Simulations of laser ablation would directly benefit from a dynamic implementation of the vertex model valid outside the quasistatic approximation.

The quasistatic approximation causes other, more subtle problems in simulations of large systems. For sufficiently large tissues, one expects the emergence of a hydrodynamic limit, which permits tissues to be treated using continuum descriptions [39, 97, 98]. Such a continuum limit is accompanied by the emergence of tissue viscosity on long timescales. In vertex model simulations, this hydrodynamic limit manifests itself in the structure of the potential energy  $F$ . For large systems,  $F$  becomes a high-dimensional potential landscape. This high-dimensionality is accompanied by long-length scale motions involving many vertices, which we refer to as “slow modes”. These slow modes are characterized by shallow gradients in the potential energy  $F$ . From a numerical point of view, because  $F$  becomes increasingly

flat for large systems, the minimization of  $F$  via a conjugate gradient method becomes increasingly numerically difficult. From a physical point of view, these slow modes relax on long timescales, and relaxing these modes is likely an unrealistic representation of the dynamics in a real tissue.

Related to the emergence of slow modes in large networks, in practice one finds length-correlations on the order of the size of the network in quasistatic simulations of the vertex model. For example, in the quasistatic growth simulations presented in Chapter 3, single cell divisions cause all vertices in the network to move <sup>1</sup>. These long-length correlations are related to the quasistatic approximation: relaxing the network potential energy is equivalent to the infinite-time limit, such that perturbations have time to be transmitted to the entire network.

Finally, quasistatic dynamics can cause inhomogeneities in the effective time evolution of simulations. For example, when simulating simple shear, the imposed shear-rate sets a timescale based on which the “rates” of other processes can be evaluated [2]. During shear simulations, strain builds up in the tissue resulting in shear stress. Eventually the tissue undergoes a topological change, such as a T1-transition. Following a T1-transition, the cells involved in the transition reorganize significantly, as the stored strain relaxes in response to the internal shear stress. Thus, quasistatic shear simulations involve continuous phases, where strain builds up in the tissue, and discontinuous changes, where T1-transitions occur and are followed by instantaneous network remodelling [2].

## 4.2 Dynamic description of the vertex model

In the vertex model, conservative forces are generated by the gradient of the potential energy  $F$ ; we call such forces “reactive”. In a dynamic description obeying Newton’s Second Law, these reactive forces must be balanced by dissipative (frictional) and inertial forces. Considering the relevant length, time, density, and viscosity scales, inertial forces in, e.g., the developing wing, are small compared to viscous friction forces and are thus neglected here. In this section we show that the resulting force balance between reactive and dissipative forces can be used to construct a dynamic equation for the vertex model, Eq. 4.11.

### 4.2.1 Generalized coordinates

In the simulations presented in this thesis, which make use of periodic boundary conditions, forces act both on the vertices and on the system boundaries. In order to define force-balance on all these variables, we introduce generalized coordinates  $q_i$ , which are typically the  $x$ - and  $y$ -coordinates of each vertex in the network, together

---

<sup>1</sup>A cell division anywhere in the network typically causes all vertices to move by numerically measurable amounts. However, rearrangement far from the site of a cell division is small compared to that in the neighbourhood of the cell division.

with the size of the periodic box  $L_x$  and  $L_y$  in the  $x$  and  $y$  dimensions. Thus, there are typically  $N_g = 2N_V + 2$  generalized coordinates  $q_i$  in a network containing  $N_V$  vertices. The generalized reactive force  $f_i^{(r)}$  acting on the  $i^{\text{th}}$  generalized coordinate  $q_i$  is then:

$$f_i^{(r)} = -\frac{\partial F}{\partial q_i}, \quad (4.1)$$

and the force balance condition is

$$f_i^{(r)} + f_i^{(d)} = 0. \quad (4.2)$$

Depending on the physical situation being described, it may be helpful to choose different generalized coordinates  $q_i$  than the  $2N_V + 2$  variables given here. For example, in Sect. 4.4 vertex displacements are used as generalized coordinates, rather than vertex positions. Furthermore, calculations can be performed in an ensemble where the periodic box dimensions  $L_x$  and  $L_y$  are fixed, or where open boundary conditions are used. In such situations the variables  $L_x$  and  $L_y$  can be excluded from the generalized coordinates.

## 4.2.2 Choices of dissipative forces

Dissipative forces represent both internal viscous forces, as well as external friction forces, for example between the network and a substrate or a fluid medium. In general, these dissipative forces  $f_i^{(d)}$  could depend on the past history of the network, on external parameters such as pressure, or on other system variables. Here we restrict our attention to a simplified case where the system possesses no “memory”, i.e., the  $f_i^{(d)}$  at any time depend only on the state of the system at that time. In writing the potential energy for the vertex model, we included terms dependent on cell area, bond length, and cell perimeter, see Eq. 2.1. This motivates us to consider friction forces corresponding to changes in these variables: we consider bond friction, area friction, and perimeter friction, which oppose changes in bond lengths, cell areas, and cell perimeters, respectively. We also consider friction forces that directly oppose changes in vertex position due to friction with a substrate or fluid medium. However, the physical interpretation of substrate friction becomes complicated when periodic boundary conditions are used. It is unclear whether changing the size of a periodic simulation box involves moving with respect to a fixed substrate. If so, then which of the vertices move, and by how much? These subtleties do not arise if the size of the periodic box is fixed during a simulation, or if open boundary conditions are used. Even when periodic boundaries are used and change during a simulation, using some nonzero but numerically small substrate friction  $\xi_r$  is helpful in solving the dynamic equations of the vertex model; this point is discussed in detail in Sect. 4.3. For generality, we include substrate-friction  $\xi_r$  in the dynamic description to follow; physical issues relating to periodic boundaries can be solved by working in the case  $\xi_r = 0$ .

### 4.2.3 Area friction

A plausible functional form for area friction can be derived in the situation where the only reactive and dissipative forces present are those relating to the areas  $A_\alpha$  of all cells  $\alpha$ . The potential energy of the network can then be written as:

$$F = F(\{A_\alpha\}) = \sum_{\alpha} \frac{K_\alpha}{2} (A_\alpha - A_\alpha^{(0)})^2. \quad (4.3)$$

In this case, a phenomenological equation describing the time evolution of cell areas  $A_\alpha$  is:

$$-\frac{\partial F}{\partial A_\alpha} - \xi_A \frac{dA_\alpha}{dt} = 0, \quad (4.4)$$

where  $\xi_A$  is a generalized friction coefficient and  $t$  is time. Here the first term represents a generalized reactive force acting on the cell area  $A_\alpha$ , and the second term represents a balancing generalized dissipative (friction) force. Even in this simplified case, there is some freedom in writing Eq. 4.4. The specific choice given here is motivated by an analogy to Stokes' law, where the friction force on a body moving in a viscous fluid is linear in the velocity of that body relative to the fluid. Alternatively, Eq. 4.4 can be derived by supposing  $\partial F/\partial A_\alpha$  is a function of  $A_\alpha$  and its time derivatives such that  $\xi_A dA_\alpha/dt$  is the first nonzero term in a systematic expansion. Eq. 4.4 gives:

$$-\frac{\partial F}{\partial A_\alpha} \frac{\partial A_\alpha}{\partial q_i} - \xi_A \frac{dA_\alpha}{dt} \frac{\partial A_\alpha}{\partial q_i} = 0, \quad (4.5)$$

where summation over  $\alpha$  is implied. We identify the reactive and dissipative forces acting on a generalized coordinate  $q_i$ :

$$-\frac{\partial F}{\partial A_\alpha} \frac{\partial A_\alpha}{\partial q_i} = f_i^{(r)} \quad (4.6)$$

$$-\xi_A \frac{dA_\alpha}{dt} \frac{\partial A_\alpha}{\partial q_i} = f_i^{(d)}, \quad (4.7)$$

and identify Eq. 4.5 as the force balance condition  $f_i^{(r)} + f_i^{(d)} = 0$ . Rewriting  $f_i^{(d)}$ , we find

$$f_i^{(d)} = -M_{ij} \frac{dq_j}{dt}, \quad (4.8)$$

where summation over  $j$  is implied and the friction matrix  $M_{ij}$  is given by

$$M_{ij} = \xi_A \frac{\partial A_\alpha}{\partial q_i} \frac{\partial A_\alpha}{\partial q_j}, \quad (4.9)$$

for the case where area friction is the only dissipative force present in the system.

### 4.2.4 Dynamic equation for the vertex model

The same arguments as given in Sect. 4.2.3 can be used to derive friction matrices  $M_{ij}$  corresponding to bond, perimeter, and substrate friction. Assuming that the friction forces add linearly, we obtain the following friction matrix for the vertex model:

$$M_{ij} = \xi_A \frac{\partial A_\alpha}{\partial q_i} \frac{\partial A_\alpha}{\partial q_j} + \xi_L \frac{\partial L_\alpha}{\partial q_i} \frac{\partial L_\alpha}{\partial q_j} + \xi_l \frac{\partial l_k}{\partial q_i} \frac{\partial l_k}{\partial q_j} + \xi_r \frac{\partial \mathbf{r}_n}{\partial q_i} \cdot \frac{\partial \mathbf{r}_n}{\partial q_j} \quad (4.10)$$

Here  $\mathbf{r}_n$  is the position of a vertex  $n$ , summations are implied over cells  $\alpha$ , bonds  $k$ , and vertices  $n$ , and  $\xi_A$ ,  $\xi_L$ ,  $\xi_l$ , and  $\xi_r$  are friction coefficients describing dissipative forces generated in response to changes in cell areas, cell perimeters, bond lengths, and vertex positions, respectively. Using Eq. 4.10 together with the force-balance condition  $f_i^{(r)} + f_i^{(d)} = 0$ , we obtain a dynamic equation for the vertex model:

$$M_{ij} \frac{dq_j}{dt} = - \frac{\partial F}{\partial q_i}. \quad (4.11)$$

In order to solve Eq. 4.11 for  $dq_j/dt$ , it is necessary that  $M_{ij}$  be invertible; this point is the subject of the next section.

## 4.3 Numerically solving vertex model dynamics

In practice, it may be that the friction matrix  $M_{ij}$  has eigenvalues that are zero, precluding the solution of Eq. 4.11. Physically speaking, zero eigenvalues in  $M_{ij}$  represent frictionless modes. In particular, in the case of periodic boundary conditions in two dimensions with no substrate friction ( $\xi_r = 0$ ), the matrix  $M_{ij}$  has two zero eigenvalues, with eigenvectors corresponding to translational invariance in each of the two dimensions.

Zero eigenvalues of  $M_{ij}$  arising from translational invariance can be dealt with in several different ways. For example, the translational invariance can be broken by adding a friction coefficient that couples to the collective motion of all vertices. However, it turns out that these are not the only zero eigenvalues that can occur. For example, in the case where friction on bond-lengths is the only dissipative process ( $\xi_A = \xi_L = \xi_r = 0$ ), the friction matrix  $M_{ij}$  will have one zero eigenvalue per cell, for each of the  $N$  cells in the network. What are the frictionless modes corresponding to these zero eigenvalues? In this case, cells can have their areas changed with zero dissipative force generated, as long as all bond lengths remain fixed, see Fig. 4.1. Ultimately, even for general  $\xi_A$ ,  $\xi_L$ , and  $\xi_l$  it is possible to have eigenvalues of  $M_{ij}$  become numerically small, at least transiently. It is useful to be able to simulate systems with zero eigenvalues of  $M_{ij}$ , for example in order to perform the calculation presented in Fig. 4.1. Thus, we need a general solution to the problem of zero eigenvalues of  $M_{ij}$ .

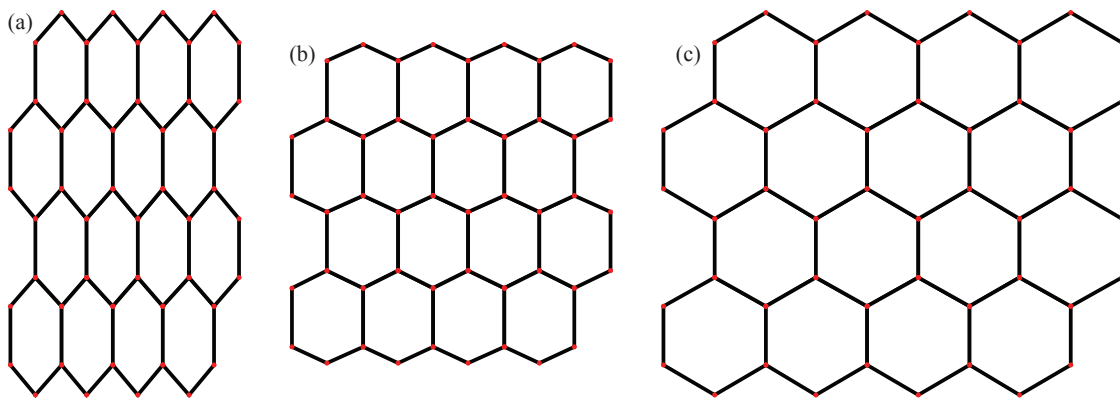


Figure 4.1: Results of a dynamic calculation in the vertex model, showing the instantaneous relaxation of frictionless modes, followed by the relaxation of other modes in finite time. (a) The initial condition for the simulation: a hexagonal network of sixteen cells, where individual cells have been compressed along the  $x$ -axis. (b) In an infinitesimal time in the future, the network relaxes to an intermediate state shown here. All bond lengths in panels (a) and (b) are numerically identical. This panel is obtained by integrating the dynamic equation Eq. 4.11 for a time interval  $\Delta t = 0.01\xi_l/(KA_0)$ . (c) In the long-time limit, bond lengths relax to their equilibrium configuration shown here. The resultant network is force-balanced and is a hexagonal network with all bond lengths identical. This panel is obtained by integrating Eq. 4.11 for a time interval  $\Delta t = 100\xi_l/(KA_0)$ . Parameters common to all panels:  $\bar{\Lambda} = 0.12$ ,  $\bar{\Gamma} = 0.04$ , and  $\xi_A = \xi_L = 0$ .

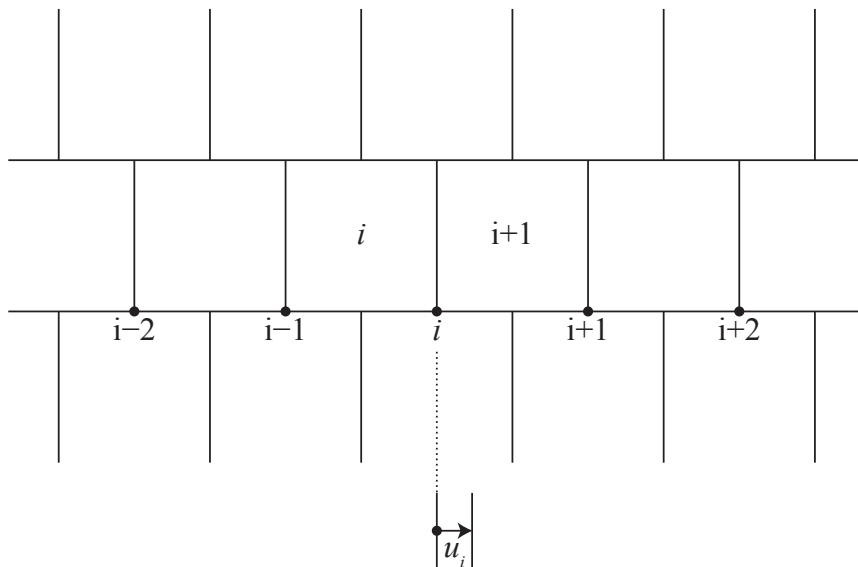


Figure 4.2: Schematic representation of a lattice of square cells. Cells in the central row and horizontal cell boundary displacements  $u_i$  are indexed with the same variable  $i$ .

Including substrate friction ( $\xi_r > 0$ ) is a simple way to ensure that  $M_{ij}$  is invertible<sup>2</sup>. However, physical arguments were given in Sect. 4.2 that  $\xi_r$  should be set to zero for systems with moving periodic boundaries. In order to ensure that  $M_{ij}$  is invertible, while avoiding issues related to periodic boundary conditions, it is helpful to choose  $\xi_r$  to be small but nonzero. If  $\xi_r$  is chosen infinitesimally small then  $\xi_r dq_j/dt$  is infinitesimal for finite  $dq_j/dt$ . This leads to a system of dynamic equations where zero eigenvalue modes are relaxed instantaneously. Physically, frictionless modes relax on timescales fast compared to the other modes in the system. Numerically,  $\xi_r$  should be chosen sufficiently small that results are unchanged when  $\xi_r$  is further decreased; meanwhile  $\xi_r$  should be sufficiently large that the eigenvalues of  $M_{ij}$  are numerically nonzero.

## 4.4 Relaxation rates

The vertex model can be treated quasistatically on timescales longer than mechanical relaxation times  $\tau_r = k_r^{-1}$ . In order to estimate the relaxation rates  $k_r$ , we consider a network of square cells with bond length  $l_0 = \sqrt{A_0}$ . For simplicity, we consider

<sup>2</sup>If the generalized coordinates  $q_i$  are simply the  $x$ - and  $y$ - coordinates of the vertices in the network, then  $\xi_r > 0$  implies that  $M_{ij}$  is positive definite and thus invertible. If the size of the periodic boundaries  $L_x$  and  $L_y$  are included in the generalized coordinates  $q_i$ , then it is necessary that at least one other friction coefficient ( $\xi_A$ ,  $\xi_L$ , or  $\xi_t$ ) be nonzero in order for  $M_{ij}$  to be invertible.

the case where all cells have common preferred area  $A_\alpha^{(0)} = A_0$ , perimeter stiffness  $\Gamma_\alpha = \Gamma$ , and area stiffness  $K_\alpha = K$ , and where all bonds have the same line tension  $\Lambda_k = \Lambda = -8\Gamma l_0$ . Such lattices are among the degenerate ground states in region (I) of the phase diagram ( $\bar{\Lambda} = -8\bar{\Gamma}$ ), see Fig. 2.1. To perturb the system away from the ground state, we introduce horizontal displacements  $u_i$  on one row of cell boundaries, see Fig. 4.2. A cell  $i$  in such a network has area  $A_i = A_0 + l_0(u_i - u_{i-1})$  and perimeter  $L_i = 4l_0 + 2u_i - 2u_{i-1}$ . The potential energy of the network can be written as

$$F = F_0 + \frac{1}{2}(KA_0 + 4\Gamma) \sum_i (u_i - u_{i-1})^2, \quad (4.12)$$

where  $F_0 = -8N\Gamma A_0$ . The derivative of the network potential energy with respect to the displacement is then:

$$\frac{\partial F}{\partial u_i} = (KA_0 + 4\Gamma)\Delta u_i \quad (4.13)$$

where  $\Delta u_i = 2u_i - u_{i-1} - u_{i+1}$ . Using the displacements  $u_i$  as generalized coordinates, we obtain for the friction matrix:

$$M_{ij} = (\xi_A + 2\xi_L)(2\delta_{ij} - \delta_{n,j-1} - \delta_{n,j+1}) + (4\xi_l + 2\xi_r)\delta_{ij}, \quad (4.14)$$

where  $\delta_{ij}$  is the Kronecker delta. Substituting Eqs. 4.13 and 4.14 into 4.11 yields a system of coupled differential equations for the displacements  $u_i$ :

$$(A_0\xi_A + 2\xi_L)\frac{d\Delta u_i}{dt} + (4\xi_l + 2\xi_r)\frac{du_i}{dt} = -(KA_0 + 4\Gamma)\Delta u_i. \quad (4.15)$$

The system of equations Eq. 4.15 is similar to the one that arises in the derivation of the normal modes of a one-dimensional monatomic lattice [147]. By analogy, we choose the ansatz:

$$u_i(t) = u_0 e^{(2\pi I m i / N_x) - k_m t}, \quad (4.16)$$

where  $u_0$  is the initial amplitude of a perturbation,  $k_m$  is the relaxation rate,  $N_x \approx \sqrt{N}$  is the number of cells in the  $x$ -direction,  $m$  is an integer, and  $I = \sqrt{-1}$ , not to be confused with the index  $i$ . Substituting Eq. 4.16 into Eq. 4.15 yields an expression for  $k_m$ :

$$k_m = \frac{2(KA_0 + 4\Gamma) \sin^2\left(\pi \frac{m}{N_x}\right)}{2\xi_l + \xi_r + 2(A_0\xi_A + 2\xi_L) \sin^2\left(\pi \frac{m}{N_x}\right)}. \quad (4.17)$$

For  $m = 0$  the relaxation rate  $k_m$  vanishes; this corresponds to the trivial solution where cell boundaries are displaced by a constant amount  $u_i(t) = u_0$ . The slowest nonzero relaxation rate is obtained for  $m = 1$ , yielding:

$$k_{\min} \approx \frac{2\pi^2(KA_0 + 4\Gamma)}{(2\xi_l + \xi_r)N}, \quad (4.18)$$

where we have approximated  $N_x \approx \sqrt{N}$  and neglected terms of order  $O(1/N^2)$ .

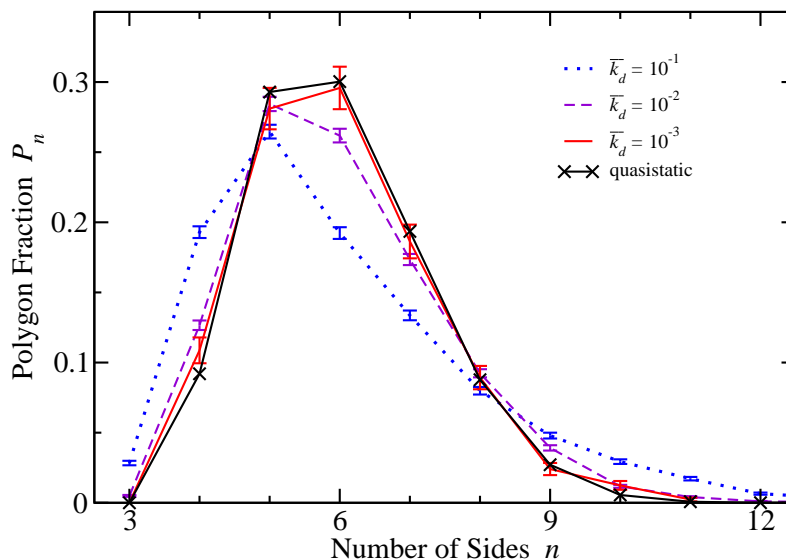


Figure 4.3: Fraction of  $n$ -sided polygons as a function of cell neighbour number  $n$  computed in growth simulations of the vertex model. Results are presented for three different values of the ratio  $\bar{k}_d = k_d \xi_l / (K A_0)$  namely  $\bar{k}_d = 10^{-1}$ ,  $10^{-2}$ , and  $10^{-3}$ . The black curve represents the result of a quasistatic calculation, and is identical to the black curve shown in Fig. 3.4a. These calculations show that in the limit of low friction (equivalently, slow growth) the quasistatic result is recovered. Parameters:  $\bar{\Lambda} = 0.12$ ,  $\bar{\Gamma} = 0.04$ ,  $\xi_L = 0$ ,  $\xi_A = \xi_l / A_0$ , and  $\xi_r = 10^{-5} \xi_l$

## 4.5 Effects of friction on tissue growth

In order to simulate tissue growth using the dynamic description presented here, it is necessary to choose the time between cell divisions  $\Delta t$  appropriately. Two dominant effects determining  $\Delta t$  are: (i) As the number of cells  $N$  increases, more cells are available to divide, and the time between single cell divisions thus decreases. (ii) Cell division is a fluctuating process, so times  $\Delta t$  should be drawn from a distribution of possible waiting times. Here we assume that single cells divide as a Poisson process with rate  $k_d$ . We assume furthermore that distinct cells divide independently from one another, such that the collective process of cell division in a tissue of  $N$  cells is a Poisson process with rate  $Nk_d$ . Under these assumptions, the time between cell divisions  $\Delta t$  has an exponential probability density function  $P_d$ :

$$P_d(\Delta t) = Nk_d \exp(-Nk_d \Delta t). \quad (4.19)$$

Values of  $\Delta t$  can be stochastically drawn from this distribution using the so-called inversion method [148, 149]:

$$\Delta t = \frac{-\ln u}{Nk_d}, \quad (4.20)$$

where  $u$  is a random number chosen uniformly from the interval  $[0, 1]$ . The statistics of tissue growth in real organisms are not completely known and are certainly non-Poissonian in nature. Nevertheless, we make use of a Poissonian growth rule here for simplicity; different growth rules can be used when greater detail or realism is required [78].

We present in Fig. 4.3 polygon distributions obtained in growth simulations analogous to those presented in Sect. 3.4. Cell division is performed using the simplified algorithm described in Sect. 3.3, with the exception that, rather than relaxing via a conjugate-gradient method between cell divisions, the system is evolved forward in time according to Eq. 4.11. The numerical procedure is as follows: After the system is initialized, or following a cell division, the time until the next cell division  $\Delta t$  is stochastically computed via Eq. 4.20.  $dq_i/dt$  is then integrated over a time interval  $\Delta t$ , using an explicit Runge-Kutta method of second and third order with adaptive step-size control [144]. At each step of the numerical integration,  $dq_i/dt$  is computed via the numerical solution of Eq. 4.11, obtained using Gaussian elimination with partial pivoting [144, 150]. Overall, each cell division requires that the system be evolved forward in time by a stochastically determined time unit  $\Delta t$ , each time evolution step  $\Delta t$  involves up to hundreds of integration steps  $dt$ , and each integration step requires the solution to an  $N_g \times N_g$  system of linear equations, where  $N_g = 2N_V + 2$  is the dimension of  $M_{ij}$ .

We see in Fig. 4.3 that as the friction coefficients  $\xi_l$  and  $\xi_A$  are decreased at a fixed growth rate  $k_d$ , the resulting polygon distributions (dotted blue, dashed purple, and solid red curves) converge to the results obtained using a quasistatic algorithm (black curve). A priori, we expected the quasistatic result to emerge in cases where cell division is slow compared to the internal relaxation time of the tissue. In Sect. 4.4, we estimated that the slowest relaxation mode in the vertex model relaxes at a rate:

$$k_{\min} \approx \frac{2\pi^2(KA_0 + 4\Gamma)}{(2\xi_l + \xi_r)N}. \quad (4.21)$$

Performing an order-of-magnitude comparison between the time between cell divisions  $\Delta t \approx (Nk_d)^{-1}$  and  $k_{\min}^{-1}$  for  $N \approx 100$ , we find that the quasistatic limit should be obtained for  $\overline{k_d} < 10^{-3}$ , where  $\overline{k_d} = k_d \xi_l / (KA_0)$ , consistent with Fig. 4.3.

## 4.6 Summary

In this chapter a dynamic description for the vertex model is developed based on a balance between reactive and dissipative (frictional) forces. A dynamic equation was presented, describing the time evolution  $dq_j/dt$  of the system variables  $q_j$  in terms of

---

a friction matrix  $M_{ij}$  and the gradient of the potential energy, see Eqs. 4.10 and 4.11. Relaxation modes in this model were derived in a simplified scenario using a network of square cells. This dynamic description was applied in Sect. 4.5 to study the effects of friction on tissue growth, demonstrating the emergence of the quasistatic result in the limit of low friction, i.e., the limit of slow growth. The focus of the present chapter was on constructing a dynamic description of the vertex model that was physically motivated, could be used to perform simulations, and could be used to understand the emergence of the quasistatic limit. In future work, the methods presented here would be well applied for understanding laser-ablation experiments where single cell boundaries are cut using a laser.



## 5 Quantifying tissue dynamics in experiments

Here we turn our attention to experimental data, developing quantification methods for cell flow and planar polarity based on theoretical definitions. We define in Sect. 5.1 an algorithm for quantifying cell flow in experimental images based on correlations between subsequent frames in time-lapsed confocal microscope images. The resultant velocity fields are then analyzed using a unique decomposition of the velocity gradient tensor into terms corresponding to local rotation, shear, and compression. In Sect. 5.2 we describe a theoretical definition and quantification method for planar cell polarity (PCP). The analysis presented here motivates a hydrodynamic theory of polarity reorientation, presented in Sect. 6.1 of the next chapter. That hydrodynamic theory is subsequently compared to a cell-scale model of polarity, presented in Sect. 6.2, based on the same vertex model presented in Chapters 2–4. Thus the quantifications presented here connect to a theory of planar polarity, which itself connects with the vertex model of the preceding chapters, unifying the themes of this thesis. It is worth pointing out to the interested reader that, while the research presented in this chapter was in the publication process, a related paper was published on morphogenetic strain rates [151].

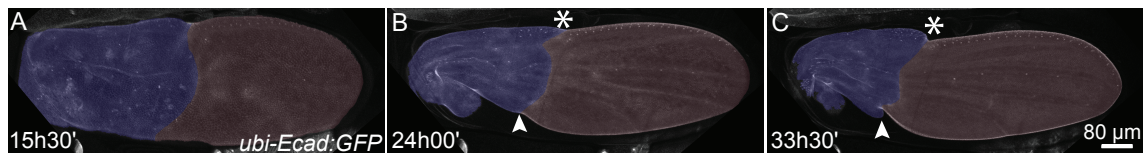


Figure 5.1: The wing hinge contracts during development. The wing hinge (blue) and blade (red) are shown at three times during development (A) 15h30' after puparium formation (APF), (B) 24 hours after puparium formation (APF), and (C) 33h30' APF. Figure by B. Aigouy reproduced from [2].

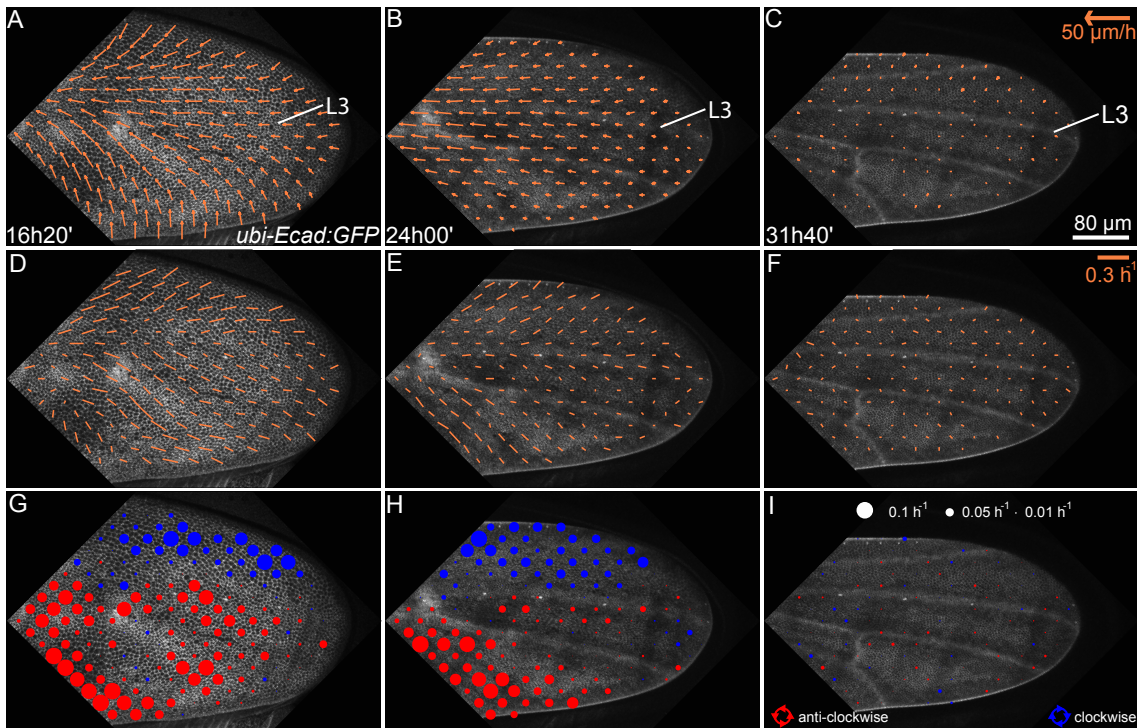


Figure 5.2: Quantified cell flow velocity field (A-C), shear field (D-F), and rotation field (G-I) in a *Drosophila* wing at three indicated times during development. Times are measured in hours after puparium formation (hAPF).

## 5.1 Cell velocity and derivative fields

During development, cells divide, cells die, and processes such as differential adhesion drive cell rearrangement. In the wing of the fly, the hinge (the region where the fly wing attaches to the fly body) contracts significantly, see Fig. 5.1. These active processes cause cells to flow, highlighting the fact that tissues can behave as viscoelastic fluids during development.

### 5.1.1 Cell flow

As raw data for quantifying cell-flow in the fly wing during development, we obtain videos of developing fly wings courtesy of our experimental collaborators<sup>1</sup>. These videos are obtained as series of time-lapsed confocal microscope images. The flies being imaged are transgenic, having the transmembrane protein E-Cadherin fluorescently labelled with green fluorescent protein (GFP). A typical experimental data set surveyed fifteen to seventeen hours of development, with images taken every five to seven minutes. These developmental videos show dramatic cell flow, see Fig. 5.2.

<sup>1</sup>B. Aigouy, A. Sagner, and J.-C. Röper, and S. Eaton at MPI-CBG, Dresden.

Given these raw data sets, spatiotemporal velocity fields are quantified using correlations between subsequent time-lapsed images. Firstly, images are divided into a Cartesian grid. For each square region  $\tau(t_i)$  in each time frame  $i$ , we minimize the function

$$\chi^2(\Delta\mathbf{r}) = \frac{1}{A_\tau} \int_\tau dx dy [I(\mathbf{r}; t_i) - I(\mathbf{r} + \Delta\mathbf{r}; t_{i+1})]^2 + \eta |\Delta r^2 - \Delta r_\tau^2(t_{i-1})| \quad (5.1)$$

with respect to  $\Delta\mathbf{r}$ , extracting the displacement  $\Delta\mathbf{r}_\tau(t_i)$  over which the region  $\tau$  moved during a time interval  $\Delta t = t_{i+1} - t_i$ . Here  $I(\mathbf{r}; t)$  is the experimental intensity profile,  $A_\tau$  is the area of a single square region, and  $\eta$  is a parameter that disfavors rapid changes in the displacement  $\Delta\mathbf{r}_\tau$ . We then define the average velocity  $\mathbf{v}_\tau(t_i)$  of the region  $\tau$  over  $N_f = 10$  images before and after the time  $t_i$ :

$$\mathbf{v}_\tau(t_i) = \frac{1}{t_{i+N_f} - t_{i-N_f}} \left( \sum_{j=i-N_f}^{i+N_f-1} \Delta\mathbf{r}_\tau(t_j) \right). \quad (5.2)$$

Resulting from this analysis is the complete spatiotemporal velocity field, which we present for one wing and three specific time-points in Fig. 5.2A-C. The complete spatiotemporal field is presented as a video in Supplemental Movie S3 of Ref. [2]. At earlier stages of development (Fig. 5.2A), we find that the cell velocity field contains a significant inward (anterior-posterior) component, as well as a significant component in the distal direction (towards the base of the wing). Later in development (Fig. 5.2B), the inward component of the velocity field is no longer visible, although significant flow is still visible in the distal direction. Cell flow ultimately drops to zero at the end of development, around 32 hAPF (hours after puparium formation, Fig. 5.2C).

### 5.1.2 Local rotation, shear, and compression rates

For the analysis of experimental flow fields we define spatial derivatives of velocity, namely local compression, shear, and rotation rates. We start by defining the velocity gradient tensor,  $\partial_i v_j$ , which we separate into a trace, a traceless symmetric part, and a traceless antisymmetric part:

$$\begin{pmatrix} \partial_x v_x & \partial_x v_y \\ \partial_y v_x & \partial_y v_y \end{pmatrix} = \begin{pmatrix} C & 0 \\ 0 & C \end{pmatrix} + \begin{pmatrix} S_1 & S_2 \\ S_2 & -S_1 \end{pmatrix} + \begin{pmatrix} 0 & \omega \\ -\omega & 0 \end{pmatrix}. \quad (5.3)$$

We identify in this decomposition the local compression rate  $C = (\partial_x v_x + \partial_y v_y)/2$  and the local rotation rate  $\omega = (\partial_x v_y - \partial_y v_x)/2$ . The components  $S_1 = (\partial_x v_x - \partial_y v_y)/2$  and  $S_2 = (\partial_x v_y + \partial_y v_x)/2$  form a traceless symmetric tensor that describes the local shear rate  $k_s = (S_1^2 + S_2^2)^{1/2}$  and axis  $\theta_s$ , where

$$\begin{aligned} \cos 2\theta_s &= S_1/k_s, \\ \sin 2\theta_s &= S_2/k_s. \end{aligned} \quad (5.4)$$

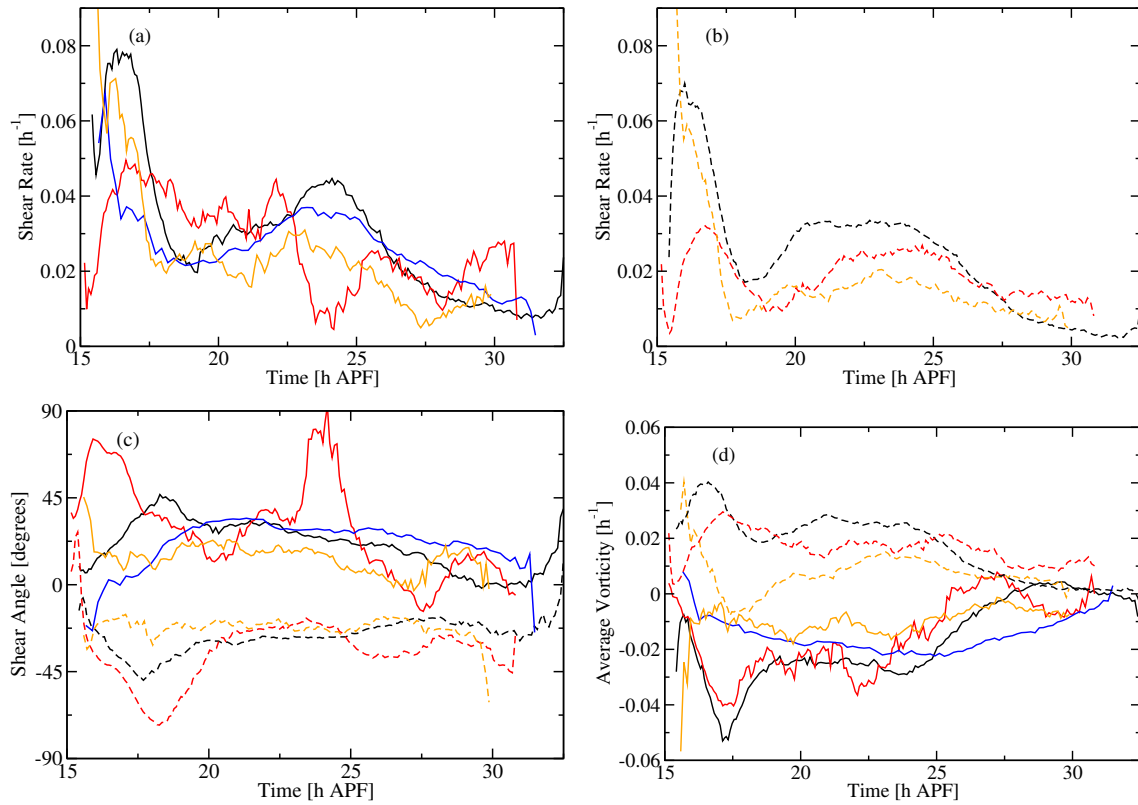


Figure 5.3: Average shear and vorticity in four *Drosophila* wings. In each panel, solid curves represent averages over the region anterior to the third longitudinal vein (L3), and dashed curves represent averages posterior to L3. Black and red curves correspond to wild-type wings, while yellow and blue curves correspond to mutant wings misexpressing the protein Ds. (A) Average shear rate anterior to L3. (B) Average shear rate posterior to L3. (C) Average shear angle anterior (solid curves) and posterior (dashed curves) to L3. (D) Average vorticity (rotation) rates anterior and posterior to L3. The black curves in this figure correspond to the same wing as presented in Fig. 5.2. Average shear was computed by averaging the tensor components  $S_1$  and  $S_2$ . The posterior region for one Ds wing (blue) was not analyzed because the flow field could not be determined in the posterior region of that wing.

Thus, the spatiotemporal velocity field can be used to define spatiotemporal compression, shear, and rotation fields for a given developmental video. Shear and rotation fields for three specific time points are presented in Fig. 5.2D-F and Fig. 5.2G-I, respectively. The complete spatiotemporal patterns are given in Supplemental Movie S3 of Ref. [2]. The shear field (Fig. 5.2D-F) shows a fan-like pattern roughly symmetric around the third longitudinal vein (L3)<sup>2</sup>. Most dramatic, however, is the rotation field (Fig. 5.2D-F), which shows a clear antisymmetry around L3, with clockwise rotations anterior to L3 and counter-clockwise rotations posterior to L3.

The observed symmetries around the vein L3 suggest computing averages of  $S_1$ ,  $S_2$  and  $\omega$  separately in these two regions of the wing. The results of such an analysis are presented in Fig. 5.3 for two different wild-type wings (red and black curves), as well as for two mutant wings misexpressing the protein Ds (yellow and blue curves). Averages computed over anterior and posterior regions are represented as solid and dashed curves, respectively. Average shear rates show large fluctuations (Fig. 5.3A-B), and it is difficult to make conclusive statements based on Fig. 5.3A-B. Much clearer signals, however, are visible in the angle of average shear (Fig. 5.3C) and the average vorticity (Fig. 5.3D). Indeed, we see from Fig. 5.3C that shear angles anterior to L3 are predominantly positive with respect to the proximal-distal axis (in the range  $[0, 90^\circ]$ ). Conversely, shear angles posterior to L3 are negative (in the range  $[-90^\circ, 0]$ ), corroborating the impression of a “fan-like” pattern in Fig. 5.2D-E. The rotational asymmetry between anterior and posterior compartments is similarly captured in Fig. 5.3D, which clearly demonstrates clockwise (negative) vorticity in the region anterior to L3 and counter-clockwise (positive) vorticity in the region posterior to L3.

In order to better elucidate the data presented in Fig. 5.3, we define the total shear and rotation at a time  $t$ :

$$\begin{aligned} S_1^{(t)} &= \int_0^t S_1 dt' \\ S_2^{(t)} &= \int_0^t S_2 dt' \\ \omega^{(t)} &= \int_0^t \omega dt', \end{aligned} \tag{5.5}$$

where  $S_1 = S_1(t')$ ,  $S_2 = S_2(t')$ , and  $\omega = \omega(t')$  are the local time-dependent shear and rotation rates. The total shear is then characterized by an axis and a magnitude, and is represented by a traceless symmetric tensor with components  $S_1^{(t)}$  and  $S_2^{(t)}$ . Total shear and rotation are calculated for average regions by averaging each of the rates  $S_1$ ,  $S_2$ , and  $\omega$  in the region of interest before calculating the integrals in Eq. 5.5. The results of this analysis are presented in Fig. 5.4. As expected, the relative fluctuations in Fig. 5.4 are much smaller than those seen in Fig. 5.3, although the

<sup>2</sup>See Fig. 1.6 for a description of wing veins.

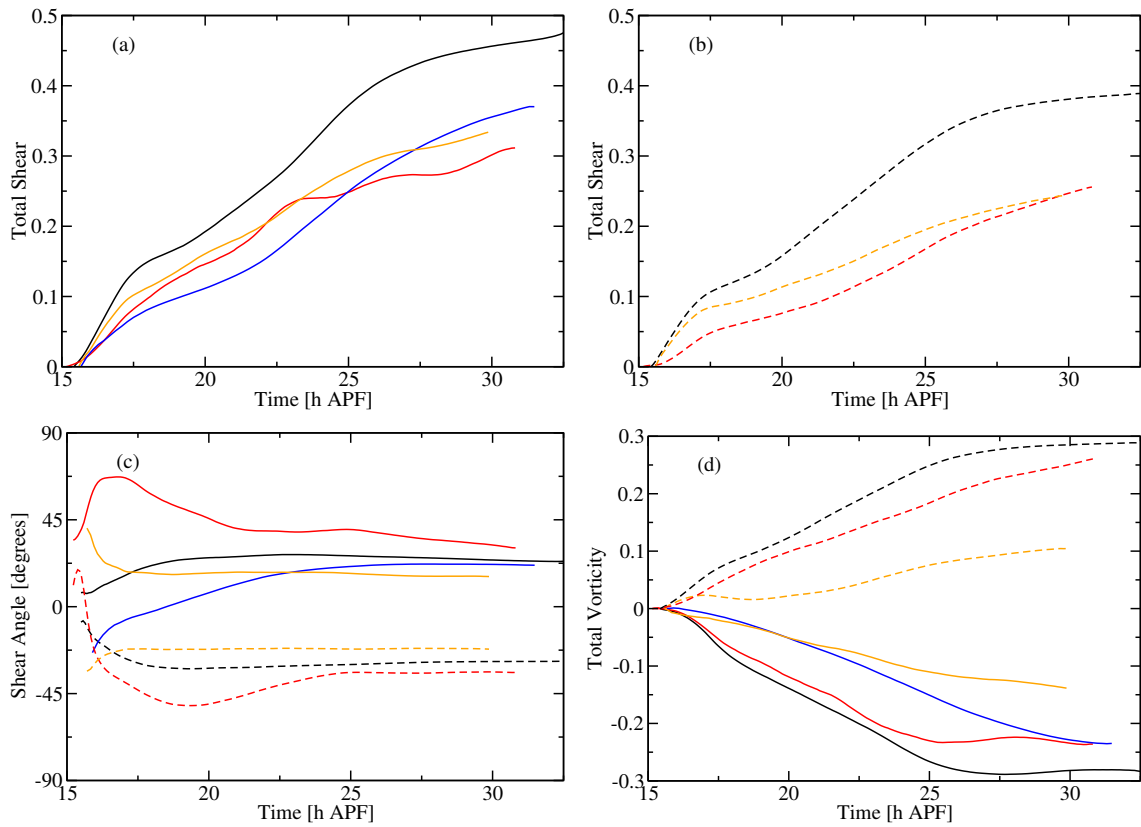


Figure 5.4: Total shear (a-b), angle of total shear (c) and total rotation or vorticity (d) in regions anterior and posterior to the third longitudinal vein in four different fly wings. All colours and symbols are consistent with those presented in Fig. 5.3: Solid curves represent totals for anterior regions, dashed curves for posterior regions; black and red curves are values for two different wild-type wings, while blue and yellow curves are values for two different mutant wings.

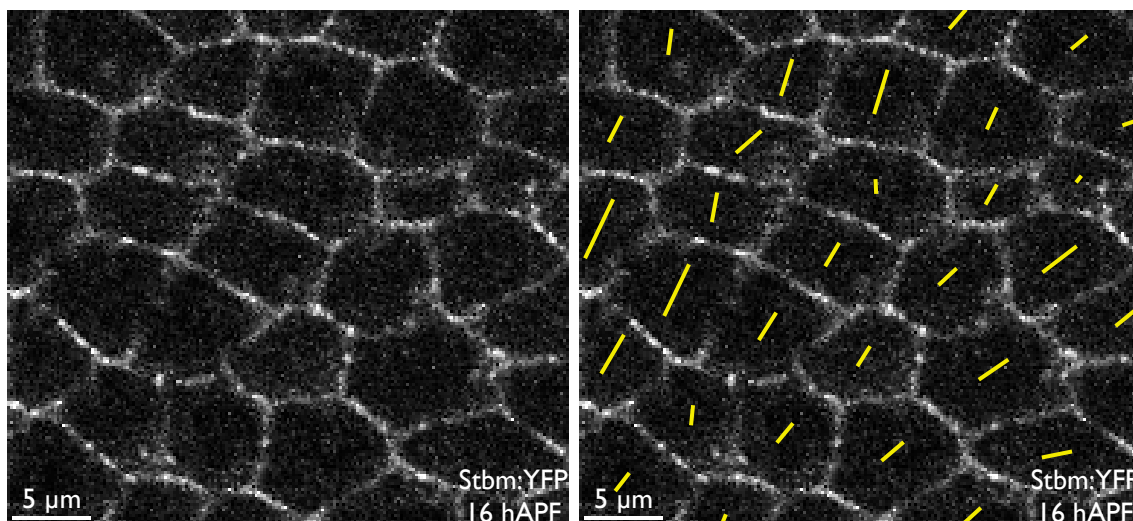


Figure 5.5: Confocal microscope image of cells in a Stbm:YFP expressing wing at an earlier time in development 16 h after puparium formation (hAPF). (a) Without quantification, it is not obvious if there is an anisotropy (polarity) in the intensity profile of Stbm:YFP in this image. (b) The same image in (a) overlaid with yellow bars representing the quantified polarity pattern. Yellow bars are placed at the angle of nematic order  $\phi_n$ , and have length proportional to the magnitude of nematic order  $Q$  for a given cell.

message of the two figures is the same. Note that the total rotation or vorticity (Fig. 5.4D) is simply the integral of the rotation or vorticity rate presented in 5.3D, although this is not the case for the total shear<sup>3</sup>.

The patterns of shear and rotation presented in this section are necessary for the proper functioning of planar polarity in the fly wing, as will be demonstrated in the remainder of this thesis. This connection between cell mechanics and planar polarity, yet to be established, is a unifying theme of this thesis.

## 5.2 Planar cell polarity

In order to calculate and subsequently visualize planar cell polarity (PCP) in the wing of the fruit fly *Drosophila*, we developed a quantification method based on the cell-perimeter intensity of a particular PCP protein (Stbm) labelled with yellow fluorescent protein (YFP). Here the raw data provided by the experimentalist are time-lapsed confocal microscope images of cells in Stbm:YFP expressing wings, see Fig. 5.5.

<sup>3</sup>The total shear is  $[(S_1^{(t)})^2 + (S_2^{(t)})^2]^{1/2}$ , which is not the same thing as the integral of the shear rate  $k_s = (S_1^2 + S_2^2)^{1/2}$ .

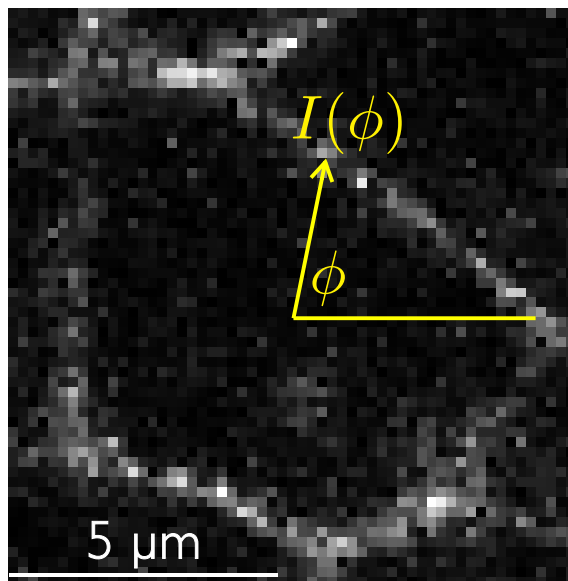


Figure 5.6: Coordinate system for quantifying polarity in a single cell. Here  $I(\phi)$  is the intensity measured on the cell perimeter at an angle  $\phi$  with respect to the cell center.

### 5.2.1 Quantitative definition of planar cell polarity

For a given cell in a confocal microscope image, we define the cell perimeter intensity  $I(\phi)$  as the intensity measured on the cell perimeter at an angle  $\phi$  with respect to the cell center, see Fig. 5.6. At the end of development, Stbm is found in higher concentrations at the proximal boundaries of cells, see Sect. 1.3. Thus, at the end of development one expects a peak in  $I(\phi)$  around an angle  $\phi_n$  corresponding to the proximal localization of Stbm within that cell. Furthermore, due to the limited resolution of confocal microscope images, it is not possible from the cell perimeter intensity to tell on which side of the cell boundary proteins are localized, i.e., the localization of Stbm on both sides of a given cell boundary contribute to  $I(\phi)$ . Hence, if there is a peak in  $I(\phi)$  around an angle  $\phi_n$ , then one also expects a peak in  $I(\phi)$  at  $\phi_n + \pi$  corresponding to the proximal localization of Stbm within the distally neighbouring cell, i.e. the function  $I(\phi)$  is  $\pi$ -symmetric.

The cell perimeter intensity  $I(\phi)$  can be uniquely decomposed via a Fourier expansion. Because the function  $I(\phi)$  is  $\pi$ -symmetric, the first nonzero terms in a Fourier expansion of  $I(\phi)$  are those in  $\cos(2\phi)$  and  $\sin(2\phi)$ :

$$Q_1 = \int_0^{2\pi} I(\phi) \cos 2\phi d\phi \quad (5.6)$$

$$Q_2 = \int_0^{2\pi} I(\phi) \sin 2\phi d\phi. \quad (5.7)$$

Using the Fourier coefficients  $Q_1$  and  $Q_2$ , we define the magnitude of nematic order for a single cell  $Q$  and the axis of nematic order for that cell as the angle  $\phi_n$ , where

$$Q = (Q_1^2 + Q_2^2)^{1/2} \quad (5.8)$$

$$\phi_n = \text{atan2}(Q_2, Q_1)/2. \quad (5.9)$$

Here  $\text{atan2}$  is the two-argument arctangent function <sup>4</sup>; equivalently, the angle  $\phi_n$  satisfies the two equations:

$$\cos 2\phi_n = \frac{Q_1}{Q} \quad (5.10)$$

$$\sin 2\phi_n = \frac{Q_2}{Q}. \quad (5.11)$$

The magnitude  $Q$  and axis  $\phi_n$  serve as a quantitative measure of polarity for a single cell. This choice of quantification fulfils several important requirements. Firstly, if the function  $I(\phi)$  is constant, then the magnitude of polarity  $Q$  is zero independently from the shape of the cell. This allows one to disentangle the effects of cell shape from that of an anisotropic protein distribution. In the context of experiment, if the Stbm:YFP intensity  $I(\theta)$  is homogeneous around a cell periphery, then that cell has zero nematic order using this definition. Similarly, the magnitude of nematic order  $Q$  is independent of cell size for fixed  $I(\theta)$ . Here the concept is that physically larger cells should not be declared more strongly polarized than smaller cells.

## 5.2.2 Methods for application to experimental data

In practice, experimental data are rasterized (pixelated) confocal microscope images. Considering this, the following steps are taken in order to apply Eq. 5.6 and 5.7 to experimental data:

- (i) Cell-segmentation software is used to identify cells and their boundaries <sup>5</sup>. Each cell  $\alpha$  is recorded as a set of pixel coordinates  $(x_j, y_j)$  together with the corresponding pixel intensity  $I_j$ . This procedure simultaneously identifies a set of boundary pixels for each cell, defined as pixels shared between two or more cells.

<sup>4</sup> The two-argument trigonometric function  $\text{atan2}(y, x)$  returns the polar angle of the point  $(x, y)$  in the  $x$ - $y$  plane relative to the origin. This function corrects problems with the ‘‘grammar-school’’ arctangent function  $\tan^{-1}(y/x)$ . In particular,  $\text{atan2}(y, x)$  is defined on the complete codomain  $(-\pi, \pi]$ , whereas  $\tan^{-1}(y/x)$  is defined only in the half unit-circle  $[0, \pi)$ . Additionally,  $\text{atan2}(y, x)$  is well defined for  $x = 0$ .

<sup>5</sup>Cell-segmentation software based on a Watershed algorithm was written by others (not the present author) [69].

- (ii) The geometric center  $(\bar{x}, \bar{y})$  of each cell is computed directly via the definitions:

$$\bar{x} = \frac{1}{N_p} \sum_{j=1}^{N_p} x_j, \quad (5.12)$$

$$\bar{y} = \frac{1}{N_p} \sum_{j=1}^{N_p} y_j, \quad (5.13)$$

where the sum is over all pixels belonging to the cell and  $N_p$  is the total number of such pixels.

- (iii) For each cell, the set of boundary pixels  $\{(x_j, y_j)\}$  and corresponding intensities  $I_j$  are sorted by the angle of the  $j^{\text{th}}$  pixel with respect to the cell center  $(\bar{x}, \bar{y})$ , such that  $\phi_{j+1} \geq \phi_j$ , where

$$\phi_j = \text{atan2}(y_j - \bar{y}, x_j - \bar{x}). \quad (5.14)$$

- (iv) The components of the nematic tensor corresponding to cell  $\alpha$  are computed via discretized versions of Eq. 5.6 and 5.7:

$$Q_1 = \sum_{j=1}^{N_b} I_j \cos 2\phi_j \Delta\phi_j \quad (5.15)$$

$$Q_2 = \sum_{j=1}^{N_b} I_j \sin 2\phi_j \Delta\phi_j, \quad (5.16)$$

where the sum is over all boundary pixels  $j$  belonging to cell  $\alpha$ ,  $N_b$  is the total number of pixels in the boundary, and  $\Delta\phi_j = (\phi_{j+1} - \phi_{j-1})/2$  is the midpoint difference of the angles, taking care of the periodic boundaries in our definitions of  $\phi_{i+1}$  and  $\phi_{i-1}$ :

$$\begin{aligned} \phi_{N_b+1} &\equiv \phi_1 + 2\pi \\ \phi_0 &\equiv \phi_{N_b} - 2\pi. \end{aligned} \quad (5.17)$$

- (v) Once  $Q_1$  and  $Q_2$  are computed for each cell  $\alpha$ , the discreteness of the experimental images no longer plays a role, and the procedure for quantifying planar cell polarity proceeds as described in Sect. 5.2. Each cell in an image is assigned a magnitude of nematic order  $Q$  and an axis of nematic order  $\phi_n$ . These nematics are represented on the original images as yellow bars, with length proportional to  $Q$  and bars placed passing through the cell center at an angle  $\phi_n$ .
- (vi) Finally, it is also interesting to visualize polarity on the scale of groups of cells. In order to accomplish this, cells are divided into groups in a Cartesian grid.

Cells are defined to belong to the “square” of the grid into which their center falls. In each such square, the magnitude of average nematic order  $I_n$  and the axis of average nematic order  $\theta_n$  are computed as described in Sect. 5.2.3. The average nematic order for each group of cells are then represented as yellow bars of length proportional to  $I_n$ , placed at an angle  $\theta_n$  passing through the center of the Cartesian cell.

### 5.2.3 Average nematic order

Given the components  $Q_1$  and  $Q_2$  for individual cells, we define the average nematic order for a group of  $N_c$  cells:

$$\begin{aligned}\langle Q_1 \rangle &= \frac{1}{N_c} \sum_{\alpha=1}^{N_c} Q_1^\alpha \\ \langle Q_2 \rangle &= \frac{1}{N_c} \sum_{\alpha=1}^{N_c} Q_2^\alpha,\end{aligned}\tag{5.18}$$

where  $Q_1^\alpha$  and  $Q_2^\alpha$  are the components of the nematic tensor corresponding to cell  $\alpha$ , the summation is over all cells in the patch of tissue to be averaged, and  $N_c$  is the number of cells in that patch. We then define the magnitude of average nematic order  $I_n = (\langle Q_1 \rangle^2 + \langle Q_2 \rangle^2)^{1/2}$  and the axis of average nematic order  $\theta_n$ , where

$$\begin{aligned}\cos 2\theta_n &= \frac{\langle Q_1 \rangle}{I_n} \\ \sin 2\theta_n &= \frac{\langle Q_2 \rangle}{I_n}.\end{aligned}\tag{5.19}$$

The average nematic order reflects both how well proteins are sorted within individual cells, as well as the degree to which different cells align their polarity. In order to separate these two effects we define the “cell polarization” as a measure of how well proteins are sorted within cells:

$$\langle Q \rangle = \frac{1}{N_c} \sum_{\alpha=1}^{N_c} Q^\alpha,\tag{5.20}$$

where  $Q^\alpha = [(Q_1^\alpha)^2 + (Q_2^\alpha)^2]^{1/2}$  is the magnitude of nematic order of cell  $\alpha$ . We then define the correlation between the PCP nematics of cells  $\alpha$  and  $\beta$ :

$$G_{\alpha\beta} = \frac{Q^\alpha Q^\beta}{\langle Q \rangle^2} \cos 2(\phi_n^\alpha - \phi_n^\beta),\tag{5.21}$$

where  $Q^\alpha$ ,  $Q^\beta$ ,  $\phi_n^\alpha$ , and  $\phi_n^\beta$  are the magnitudes and angles of nematic order for cells  $\alpha$  and  $\beta$ , respectively. Finally, we define the nematic correlation function  $g(r)$ , a

measure of the correlation between the PCP nematics of cells separated by a distance  $r$ :

$$g(r) = \frac{1}{n(r)} \sum_{\alpha \neq \beta} G_{\alpha\beta} B(r_{\alpha\beta}, r, \Delta r), \quad (5.22)$$

where the summation is over all pairs of cells,  $r_{\alpha\beta}$  is the distance between the centers of cells  $\alpha$  and  $\beta$ ,

$$n(r) = \sum_{\alpha \neq \beta} B(r_{\alpha\beta}, r, \Delta r), \quad (5.23)$$

is the number of cells separated by a distance  $r \pm \Delta r/2$ , and

$$B(r_{\alpha\beta}, r, \Delta r) = \Theta(r_{\alpha\beta} - r + \frac{\Delta r}{2}) - \Theta(r_{\alpha\beta} - r - \frac{\Delta r}{2}) \quad (5.24)$$

is the boxcar function, defined in terms of the unit step function  $\Theta$ .

## 5.2.4 Quantified polarity patterns at cell and tissue scales

Coarse-grained polarity patterns for *Drosophila* wings at two different stages of development are presented in Figs. 5.7A-B. Here red dots indicate the vectorial nature of polarity, and are determined via separate experiments (clonal analyses). Fig. 5.7A demonstrates that, at an earlier stage of development 15 hAPF, the *Drosophila* wing already possesses a coherent polarity pattern. Polarity at 15 hAPF is oriented in a fan-like pattern, differently in anterior and posterior compartments. At later times prior to hair outgrowth, around 30 hAPF, polarity is oriented along the proximal-distal axis. In addition to these snapshots of the polarity pattern, we can also quantify the complete time-dependence of the polarity pattern. This is shown in Figs. 5.7C-E for three time-points in a region of the anterior compartment between the first and third longitudinal veins (L1 and L3). Averaging the polarity over this region for many time-points yields the time-dependent average nematic order for the region, plotted in Fig. 5.7F.

We present in Fig. 5.8 an alternative representation of the data in Figs. 5.7C-E, namely the average polarity in a region of the anterior compartment. The lengths and angles of the bars ‘‘PCP order’’ in Fig. 5.7F are given by the magnitude and angle of average nematic order presented in Figs. 5.8A and 5.8B, respectively. We further present in Figs. 5.8C and D the cell polarization  $\langle Q \rangle$  and Nematic Correlation Function  $g(r)$ , which respectively capture the degree to which proteins are sorted within individual cells and the degree to which polarity is aligned between cells.

## 5.2.5 Connection with nematic liquid crystals

The quantification of planar cell polarity given here is inspired by an analogy to liquid crystals. Liquid crystals are composed of ellipsoidal or rod-like molecules [152].

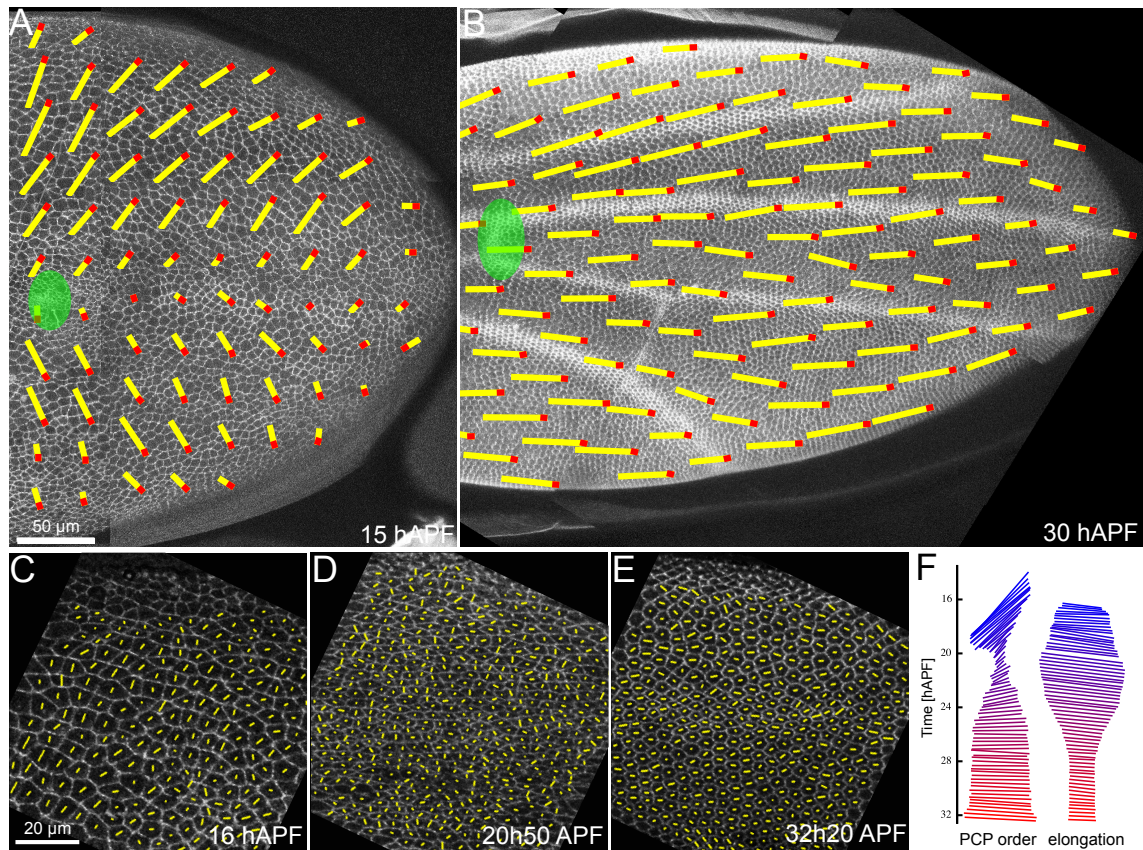


Figure 5.7: Quantified polarity pattern in wild-type *Drosophila* wings. The length and angle of yellow bars represent the magnitude and angle of nematic order, respectively. (A-B) Coarse-grained pattern of average polarity (A) earlier in development (15 hAPF) and (B) later in development prior to hair outgrowth (30 hAPF). Green ellipses represent the anterior crossvein and can be used as a marker of position. Red dots indicate the vectorial nature of the polarity pattern, and are determined in separate experiments (clonal analyses). (C-E) Cell-scale polarity pattern at three times during development, in a region between the longitudinal veins L1 and L3. The fluorescently labelled protein in panels (A-E) is *Stbm:YFP*. (F, left) Magnitude and axis of average nematic order averaged in the region shown in (C-E). (F, right) Magnitude (arbitrary units) and angle of cell elongation, a quantification of cell shape shown for comparison. Collaborative figure taken from [2].

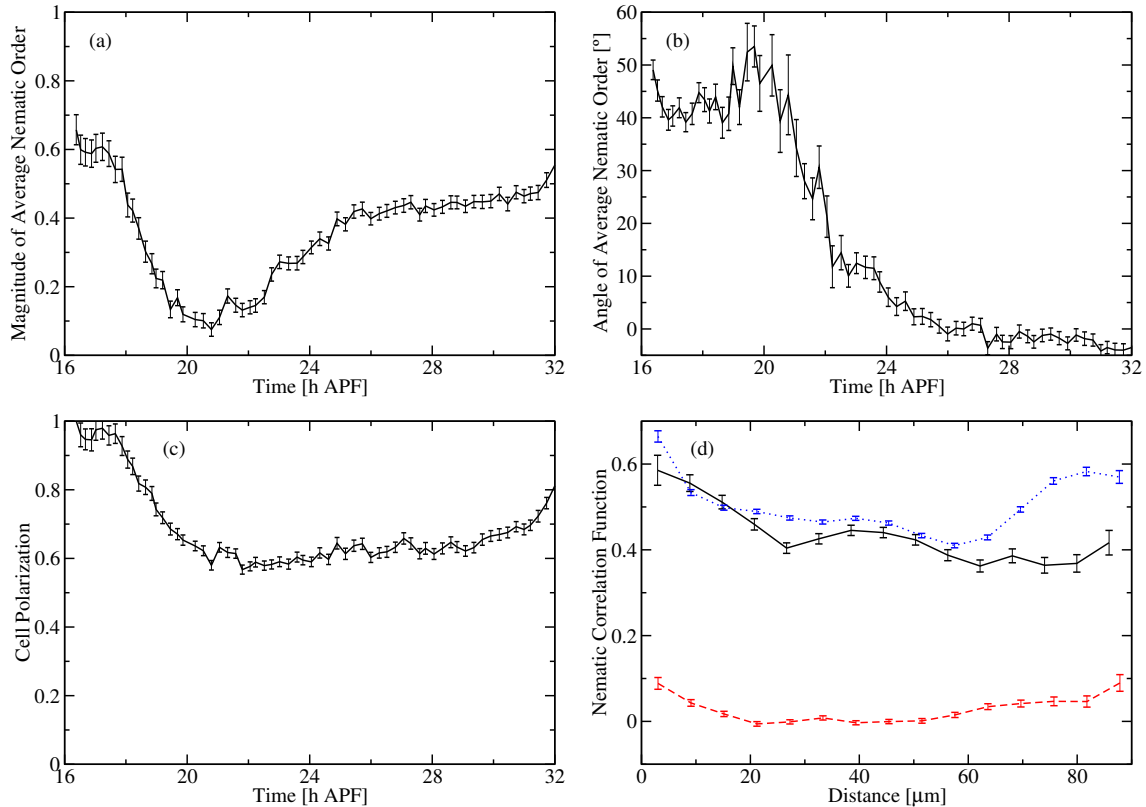


Figure 5.8: Average nematic order computed in a region between veins L1 and L3, shown as a function of time. (A-B) The magnitude and angle of average nematic order (same data as presented in Fig. 5.7F). The angle of nematic order is measured with respect to the proximal-distal axis, i.e., the horizontal axis in Fig. 5.7C-E. (C) Cell polarization  $\langle Q \rangle = \langle Q_1^2 + Q_2^2 \rangle^{1/2}$ , indicating the degree to which proteins are sorted within cells. (D) Nematic correlation function  $g(r)$  for these different times in development, namely 16 hAPF (black), 21 hAPF (red), and 32 hAPF (blue). All panels are computed for the same data presented in Fig. 5.7C-E.

In the “nematic” phase, these ellipsoidal molecules align parallel to one another. Such rod-like molecules have a mirror symmetry: rods can be perpendicular or parallel, but there is no concept of antiparallel rods because there is no vectorial asymmetry. In this sense, ellipsoidal molecules in a nematic liquid crystal have the same  $\pi$ -symmetry as the cell perimeter intensity  $I(\phi)$  introduced in Sect. 5.2.

The nematic phase of a liquid crystal can be characterized using a traceless-symmetric tensor  $Q_{ij} = \langle p_i p_j \rangle - \delta_{ij}/d$ , where  $p_i$  is a vector parallel to the ellipsoidal axis of a given molecule,  $\langle \dots \rangle$  denotes an ensemble average,  $\delta_{ij}$  is the Kronecker delta, and  $d$  is the dimensionality of the liquid crystal (e.g.  $d = 2$  or  $3$ ). In two dimensions, the traceless-symmetric tensor  $Q_{ij}$  with components  $Q_1 = Q_{xx} = -Q_{yy}$  and  $Q_2 = Q_{xy} = Q_{yx}$  can be written in matrix notation as:

$$\begin{pmatrix} Q_1 & Q_2 \\ Q_2 & -Q_1 \end{pmatrix}. \quad (5.25)$$

The eigenvalues of  $Q_{ij}$  are  $\pm Q$ , where  $Q = (Q_1^2 + Q_2^2)^{1/2}$  is the magnitude of nematic order. The eigenvector corresponding to the positive eigenvalue  $Q$  points at the angle  $\phi_n$ , where  $\phi_n = \text{atan2}(Q_2, Q_1)/2$  as defined previously. The remaining eigenvector, corresponding to the negative eigenvalue  $-Q$ , points in the perpendicular direction at angle  $\phi_n + \pi/2$ .

## 5.3 Summary

In this chapter we developed methods for quantifying cell flow and planar polarity in the *Drosophila* wing. We showed in Figs. 5.2 and 5.7 that cell flow, shear, rotation, and polarity each form coherent spatiotemporal fields in the developing wing. Figs. 5.7 and 5.8 demonstrate that polarity reorients during development between 15–30 hAPF. This observation motivates the question: What mechanisms reorient polarity during development? The comparison between polarity reorientation (Fig. 5.7) and the spatiotemporal shear and rotation fields (5.2D-I) is highly suggestive towards answering this question, which we address in Chapter 6.



# 6 Theoretical framework for planar cell polarity

In this chapter we formulate theoretical models of planar cell polarity with the aim to extract the underlying physical mechanisms present in the real system. Along these lines we present in Sect. 6.1 a hydrodynamic theory of polarity reorientation on the scale of groups of cells, based on the quantifications presented in Chapter 5. We further present in Sect. 6.2 a model of polarity at the cell scale based on the vertex model presented in Chapters 2–4.

## 6.1 Hydrodynamic theory of polarity reorientation

In general, any pattern in a moving medium will move together with the medium. If a pattern is embedded in an inhomogeneously flowing medium, then the pattern will necessarily be reorganized. These effects are captured in a hydrodynamic theory of polarity reorientation; such theories are well established in the context of liquid crystals [152]. Here we apply these ideas to investigate whether or not cell flow plays a role in reorienting polarity.

### 6.1.1 Theoretical background

A velocity vector-field can be decomposed into a homogeneous translational vector component, together with the pattern of velocity gradients. The tensor-field of velocity gradients can be subsequently decomposed into patterns of compression  $C$ , shear  $S_1$  and  $S_2$ , and rotation  $\omega$ , corresponding to the trace, traceless-symmetric part, and traceless-antisymmetric part of the velocity gradient tensor, see Sect. 5.1.2. In general each of these components couples to polarity [42, 152]. In order to describe this coupling we define a local polarity vector  $\mathbf{p}$  with components  $p_i$ , where  $i = x$  or  $y$ , together with the co-rotational derivative of the polarization vector [42]:

$$P_i = \frac{Dp_i}{Dt} = \partial_t p_i + v_j \partial_j p_i + \omega_{ij} p_j. \quad (6.1)$$

Here  $t$  is time,  $v_j$  is the  $j^{\text{th}}$  component of the velocity field  $\mathbf{v}$ , and  $\omega_{ij} = (\partial_i v_j - \partial_j v_i)/2$ . Several factors can contribute to  $P_i$ . These can be divided as  $P_i = P_i^r + P_i^d$  into

reactive components  $P_i^r$ , which change sign under time inversion, and dissipative components  $P_i^d$ , which are unchanged under time inversion. The reactive component  $P_i^r$  can be described using the phenomenological equation [42]:

$$P_i^r = -\nu p_j v_{ij} - \bar{\nu} p_i v_{jj}, \quad (6.2)$$

where  $v_{ij} = (\partial_i v_j + \partial_j v_i)/2$  is the strain-rate tensor,  $\nu$  is a parameter describing the coupling between shear and polarity, and  $\bar{\nu}$  is a parameter describing the coupling of compression and polarity. Eqs. 6.1 and 6.2 define a dynamic equation for polarity reorientation:

$$\partial_t p_i = -v_j \partial_j p_i - \omega_{ij} p_j - \nu p_j v_{ij} - \bar{\nu} p_i v_{jj} + P_i^d, \quad (6.3)$$

where the five terms on the right-hand side account for convection, local rotation, shear, compression, and dissipative effects, respectively.

### 6.1.2 Simplified dynamic equation for polarity reorientation

Eq. 6.3 can be significantly simplified for the purposes of applying it to experimental data. Firstly, we note that the term accounting for compression,  $\bar{\nu} p_i v_{jj}$ , couples only to the magnitude of the polarity vector  $\mathbf{p}$ . Recall our motivation for formulating the present hydrodynamic theory: a polarity pattern embedded in a flowing tissue will be reorganized. Here we envision shearing, locally rotating tissues reorienting polarity. Such a hypothesis does not give any insight as to how flow should influence the local magnitude of polarity. This suggests that we should restrict our attention to the angle  $\theta_v$  of the polarity vector  $\mathbf{p}$ , rather than the magnitude  $|\mathbf{p}|$ . Along these lines, we can treat the phenomenological coefficient  $\bar{\nu}$  as a Lagrange multiplier, assigning the value necessary to fix the magnitude of the polarity vector  $\mathbf{p}^2 = 1$ , but leaving the polarity angle  $\theta_v$  unchanged.

The second simplification that can be made to Eq. 6.3 is to ignore the dissipative component  $P_i^d$  of polarity reorientation. Physically, we expect polarity to corotate with a moving reference frame and thus do not expect a large dissipative component opposing patterns of local rotation. Furthermore, the terms contributing to a dissipative component include active terms and direct coupling between polarity reorientation and a conjugate external field [42]. Active terms could include the natural tendency of polarity domains to align. Terms conjugate to an external field are reminiscent of global cues for PCP, see Sect. 1.3.2. Here we purposefully neglect such terms in order to investigate mechanisms for polarity reorientation that do not rely on global cues. Similarly, we neglect the natural tendency of polarity domains to align in order to highlight the role of hydrodynamics in reorienting polarity. The final simplification that we make here is to neglect the contribution of convection  $v_j \partial_j p_i$  to polarity reorientation. This is motivated by calculation results: the calculations to follow were performed both accounting for and neglecting convection, and no differences relevant to the present discussion were observed. For the purposes of simplicity, convection was neglected in the final calculations presented here.

Ignoring dissipative terms and convection, Eq. 6.3 implies the following dynamic equation for the polarity angle  $\theta_v$ :

$$\frac{\partial \theta_v}{\partial t} = -\nu (S_2 \cos 2\theta_v - S_1 \sin 2\theta_v) + \omega, \quad (6.4)$$

where the polarity angle  $\theta_v$  is time and space dependent, and where  $\theta_v$  is measured with respect to a fixed reference frame. Rewriting this equation in terms of the local shear rate  $k_s$  and the angle of polarity with respect to the local axis of pure shear,  $\theta = \theta_v - \theta_s$ , we find:

$$\frac{\partial \theta}{\partial t} = \nu k_s \sin 2\theta + \omega. \quad (6.5)$$

Here,  $\omega$  is the local rotation rate, and  $k_s$  is the rate of pure shear. Eq. 6.5 reveals how the coefficient  $\nu$  influences polarity reorientation. For  $\omega = 0$ , Eq. 6.5 has fixed points at  $\theta = 0$  and  $\theta = \pi/2$ . The stability of these fixed points depends on the sign of the coefficient  $\nu$ : for  $\nu < 0$  the fixed point at  $\theta = 0$  (polarity parallel to shear) is stable and the fixed point  $\theta = \pi/2$  is unstable; for  $\nu > 0$  the opposite situation holds. In the absence of shear,  $k_s = 0$ , only the trivial action of local rotations on polarity is present,  $\partial \theta / \partial t = \omega$ .

### 6.1.3 Application to observed polarity reorientation

The patterns of rotation presented in Fig. 5.2G-I are consistent with the rotation of polarity shown in Fig. 5.7: anterior groups of cells collectively rotate counter-clockwise, while posterior groups of cells rotate clockwise, which is the pattern of rotations that would be necessary to reorient the fan-shaped polarity pattern of Fig. 5.7A to obtain that of Fig. 5.7B. Order of magnitude considerations agree with this assessment: local rotations in the pattern of cell flow amount to  $\sim 0.25$  radians in each of the two compartments, see Fig. 5.4.

In order to quantitatively determine the extent that hydrodynamics accounts for the polarity reorientation observed in experiments, we solved Eq. 6.4 using initial conditions, shear and rotation fields measured from experiments. The initial condition, shown in Fig. 6.1A, was generated using the same data as Fig. 5.7A with two exceptions: (i) the pattern was differently coarse-grained in order to fit onto the wing for which the flow patterns were obtained, and (ii) the resulting polarity vectors were renormalized to have equal length, because the present hydrodynamic theory does not describe the local magnitude of polarity. Given the initial condition in Fig. 6.1A, Eq. 6.4 was solved numerically, separately for each of the polarity vectors presented in Fig. 6.1. For each of the polarity vectors with angle  $\theta_v$ , the local time-dependent shear and rotation rates  $S_1$ ,  $S_2$ , and  $\omega$  were taken from the experimentally quantified spatiotemporal fields, presented for two times in Fig. 5.2.

Solving Eq. 6.4 for the 17 h developmental window under study here causes the fan-shaped initial condition of Fig. 6.1A to reorient, yielding the pattern in Fig. 6.1B at the end of the calculation. The only free parameter in such a calculation is

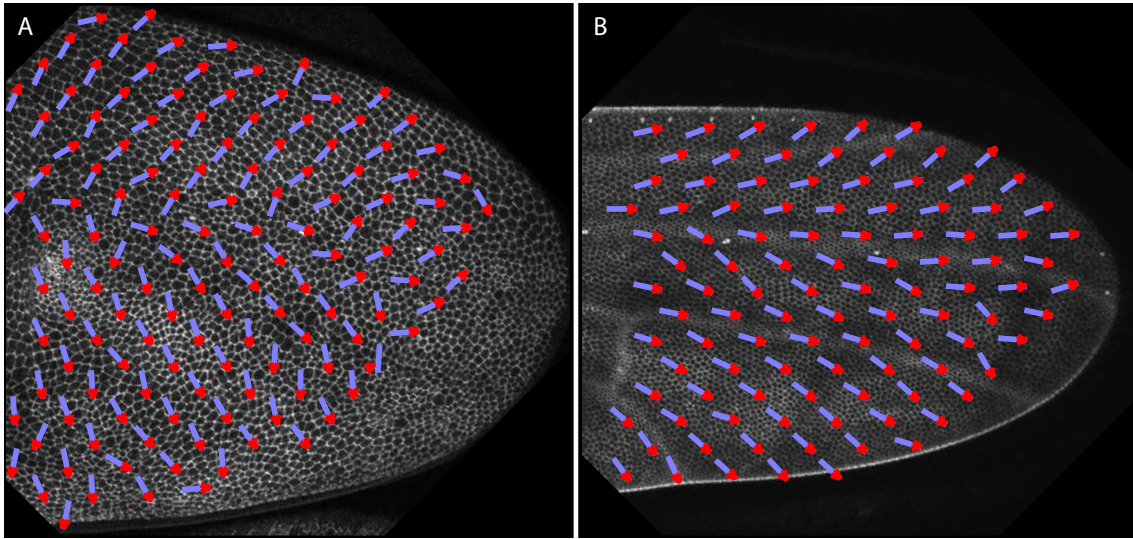


Figure 6.1: Reorientation of polarity in a hydrodynamic model. Starting from an initial condition based on experiments (A), Eq. 6.4 is solved using the parameter value  $\nu = -3$  and the spatiotemporal patterns of shear  $S_1$  and  $S_2$  and rotation  $\omega$  measured from experiment. After integrating Eq. 6.4 for an equivalent of 17 h of development, we obtain the final polarity pattern (B). The initial polarity pattern (A) is based on the pattern in Fig. 5.7A, with the exceptions that: (i) The pattern in (A) was differently coarse-grained than that in Fig. 5.7A, owing to the different shapes of the wings. (ii) All polarity vectors were normalized to constant length for the present figure. Collaborative figure taken from [2].

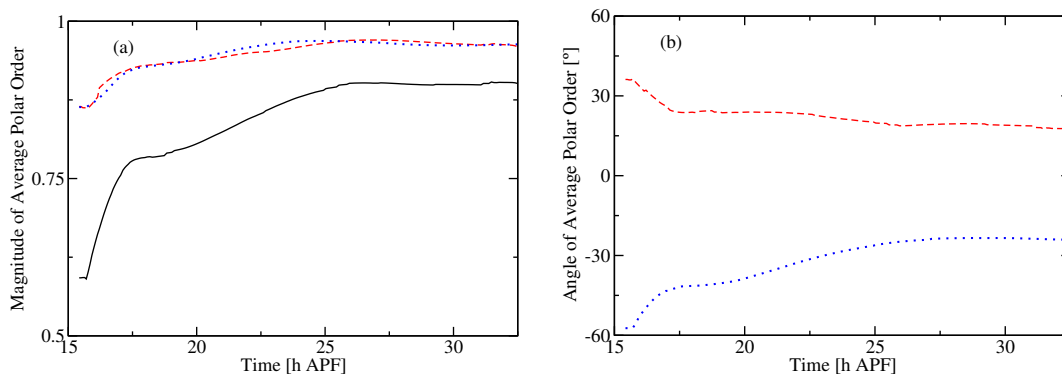


Figure 6.2: Quantification of polarity reorientation in a simple hydrodynamic model. (A-B) Magnitude (A) and angle (B) of average polar order averaged separately in anterior and posterior compartments for  $\nu = -3$ . Here dashed (red) curves represent the average polarity in the anterior to the third longitudinal vein and dotted (blue) curves represent polarity posterior to that vein. The solid black curve in (A) represents the magnitude of polar order for the complete wing, which increases to a maximum value of 0.90 at the end of the calculation. The data presented here is from the same calculation as Fig. 6.1.

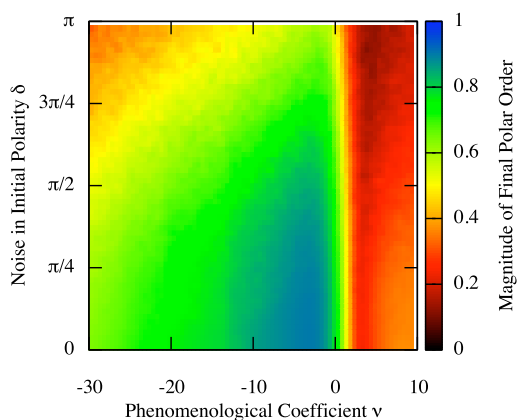


Figure 6.3: Magnitude of final polar order plotted as a function of the phenomenological coefficient  $\nu$ , as well as the magnitude of random white noise  $\delta$  added to the polarity initial condition. Calculations were computed using experimentally determined shear and rotation fields from a wild type wing, see Fig. 5.2.

the coefficient  $\nu$ . For  $\nu = 0$ , i.e. ignoring any influence of shear on polarity, polarity reorients, obtaining a final average polar order of 0.76, which is  $\sim 77\%$  of the experimental value at the end of development (0.98). Thus, local rotation makes up for a significant fraction of the reorientation observed in experiment. In order to investigate whether shear might contribute to reorientation, we repeated the calculations with nonzero  $\nu$ . We found that  $\nu \approx -3$  gives the maximum value of polar order at the end of the calculation, 0.90, or  $\sim 92\%$  of the experimentally observed value. The final polarity pattern and quantification of the computed dynamics for  $\nu = -3$  are presented in Figs. 6.1B and 6.2.

In order to test robustness with respect to noise, we performed calculations where random white noise in an interval  $\pm\delta/2$  was added to the initial condition prior to solving Eq. 6.4. The results of this analysis are presented in Fig. 6.3. We find that, within a range  $-10 < \nu < -1$ , polarity reorientation achieves an average polarity order  $\geq 0.85$ , and that this reorientation is stable in the presence of noise.

#### 6.1.4 Testing the model: Severed wings

The calculations shown in Figs. 6.1–6.3 provide strong evidence that cell flow reorients planar polarity in the *Drosophila* wing, together with the theoretical arguments of Sects. 6.1.1–6.1.2. According to the theory, altering the pattern of flow in the wing should alter the polarity reorientation, ultimately leading to a perturbed polarity pattern at the end of development. In order to test this prediction, we repeated the analysis of Chapter 5 on a fly wing that had been cut between the hinge and the blade during development. By removing the effects of hinge contraction on the blade, and potentially adding additional stresses due to wound healing, the pattern of cell flow in such mutant wings is seriously altered, see Fig. 6.4. Indeed, the pattern of cell flow is inverted, with net transport of cells from the proximal to the distal direction, compare Figs. 6.4A and 5.2B. The corresponding patterns of shear and rotation are presented in Figs. 6.4B–C. Most remarkable is the pattern of rotation in the severed wing, which is inverted with respect to the wild-type pattern, with clockwise rotation in the posterior compartment and counterclockwise rotation in the anterior compartment, see Fig. 6.4C.

The quantified polarity pattern for a severed wing at the end of development is shown in 6.4D. Indeed, the polarity pattern in severed wings is perturbed as compared to the wild-type pattern. We asked whether or not our hydrodynamic theory could consistently account for the change in polarity pattern in severed wings, given the measured change in cell flow. The first calculation which we performed along these lines was solving Eq. 6.4 using the spatiotemporal flow field measured for the wounded wing presented in Fig. 6.4, with an initial condition based on the known wild-type pattern. Once again, the dimensionless coefficient  $\nu$  is the only adjustable parameter in such a calculation. Using  $\nu \approx -3$ , such a calculation does not realistically reproduce the experimentally observed polarity pattern at the end of development. However, we found that a value of  $\nu = 2$  gave rise to a final polarity

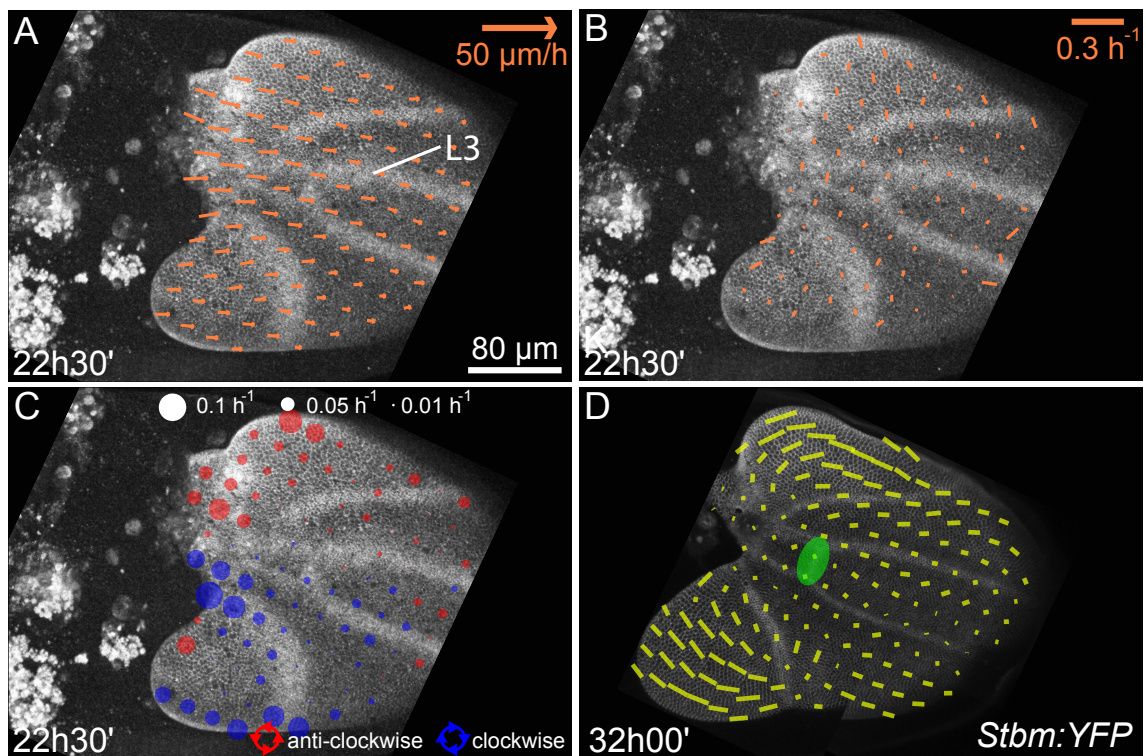


Figure 6.4: Flow (A), shear (B), rotation (C), and polarity (D) in a wing that was severed between the hinge and the blade during development. Collaborative figure taken from [2].

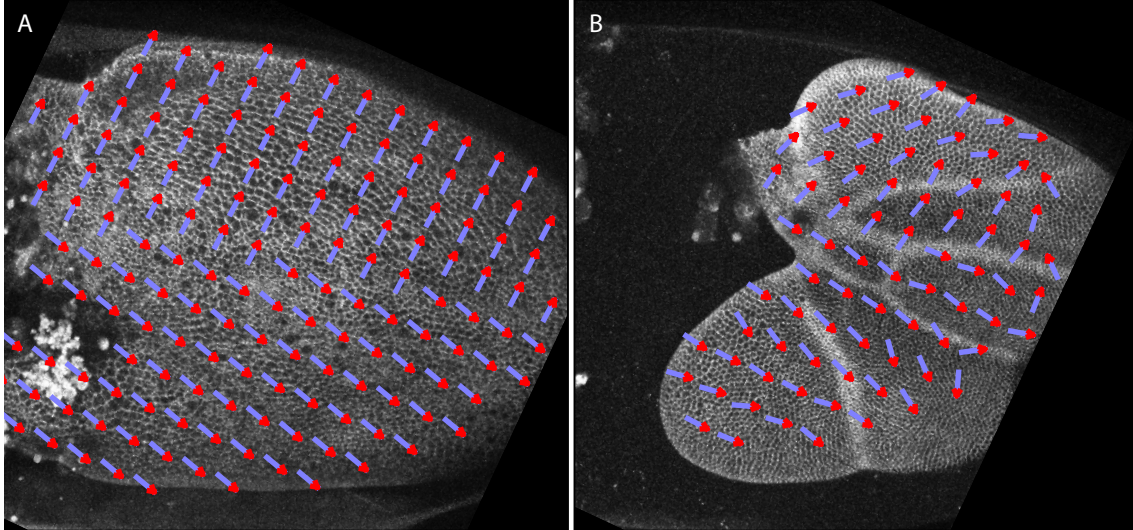


Figure 6.5: Predicted reorientation of polarity in a severed wing. Using an initial condition (A), and the spatiotemporal shear and rotation fields measured from experiment, Eq. 6.4 was solved to obtain the predicted pattern (B), using parameter value  $\nu = 2$ . Collaborative figure taken from [2].

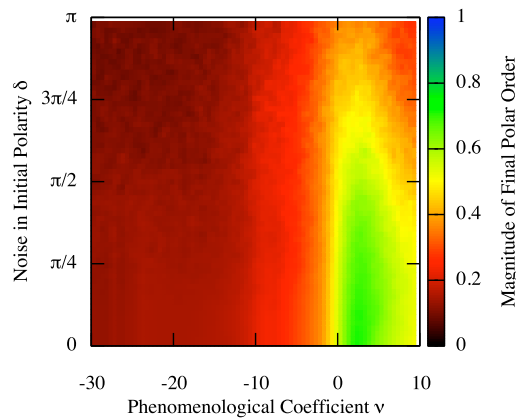


Figure 6.6: Magnitude of final polar order plotted as a function of the phenomenological coefficient  $\nu$ , as well as the magnitude of random white noise  $\delta$  added to the polarity initial condition. Calculations were computed using experimentally determined shear and rotation fields from a wing severed between the wing hinge and the blade, see Fig. 6.4.

pattern qualitatively consistent with that observed in experiment, see Fig. 6.5 and compare Fig. 6.5B with Fig. 6.4D.

We furthermore asked whether flow patterns in wounded wings could conceivably reorient polarity parallel to the PD-axis, for any value of  $\nu$ . The answer to this question is ‘no’, see Fig. 6.6. Indeed, the magnitude of final polar order remains below  $\sim 0.7$  for all values of  $\nu$ . Furthermore, we find in Fig. 6.6 that the highest magnitude of final polar order is obtained for small positive values of  $\nu$ , consistent with the value of  $\nu = 2$  used in the calculation of Fig. 6.5.

## 6.2 Planar cell polarity in the vertex model

We described in Sect. 6.1 a hydrodynamic description of polarity reorientation, valid on the scale of groups of cells, where the tissue behaves as a continuous material. Here we show that this hydrodynamic description of PCP emerges naturally in a cell-scale description of PCP based on the vertex model. This cell-scale PCP model first appeared in the doctoral thesis of R. Farhadifar [71]<sup>1</sup>. Such a model describes cell mechanics and growth using the methods described in Chapters 2–3.

PCP protein levels are described using dimensionless variables  $\sigma_i^\alpha$  and  $\sigma_i^\beta$ , see Fig. 6.7A. In this coarse-grained description, two types of PCP proteins are represented using the variables  $\sigma_i^\alpha$ : “proximal proteins” are represented as positive values of  $\sigma_i^\alpha$  and “distal proteins” are represented using negative values of  $\sigma_i^\alpha$ . Large magnitudes  $|\sigma_i^\alpha|$  represent high protein concentrations on bond  $i$  of cell  $\alpha$ . We are able to represent two protein concentrations (proximal and distal) using a single variable  $\sigma_i^\alpha$  because the accumulation of the two types of proteins are assumed to be mutually exclusive on a single bond. Proximal proteins in this simple theory correspond roughly to complexes involving Fmi, Stbm and Pk in the real experimental system; conversely, distal proteins correspond to complexes containing Fmi, Fz, Dsh, and Dgo, see Sect. 1.3.1. The interactions of PCP proteins with themselves and their environment are described using a potential:

$$E_{PCP} = J_1 \sum_i \sigma_i^\alpha \sigma_i^\beta - J_2 \sum_{\{i,j\}} \sigma_i^\alpha \sigma_j^\alpha - J_3 \sum_\alpha \epsilon^\alpha \cdot \mathbf{Q}^\alpha, \quad (6.6)$$

where the first summation describes interactions of PCP proteins between adjacent cells  $\alpha$  and  $\beta$  across a common cell boundary  $i$ , the second summation describes interactions between adjacent boundaries  $i$  and  $j$  within cells  $\alpha$ , and the third summation describes the interaction between cell shape  $\epsilon^\alpha$  and PCP nematic order  $\mathbf{Q}^\alpha$ .

<sup>1</sup>The simulations presented in Sect. 6.2 were performed by R. Farhadifar, not by the present author. Those calculations were part of a collaboration between R. Farhadifar, F. Jülicher, the experimental group of S. Eaton at MPI-CBG Dresden, and the present author. The entire group discussed and developed the model. The present author recommended specific parameter values for use in these calculations, and performed the data analysis presented in Figs. 6.8–6.9. For more information on the details of collaborative work presented in this thesis, see Appendix C.

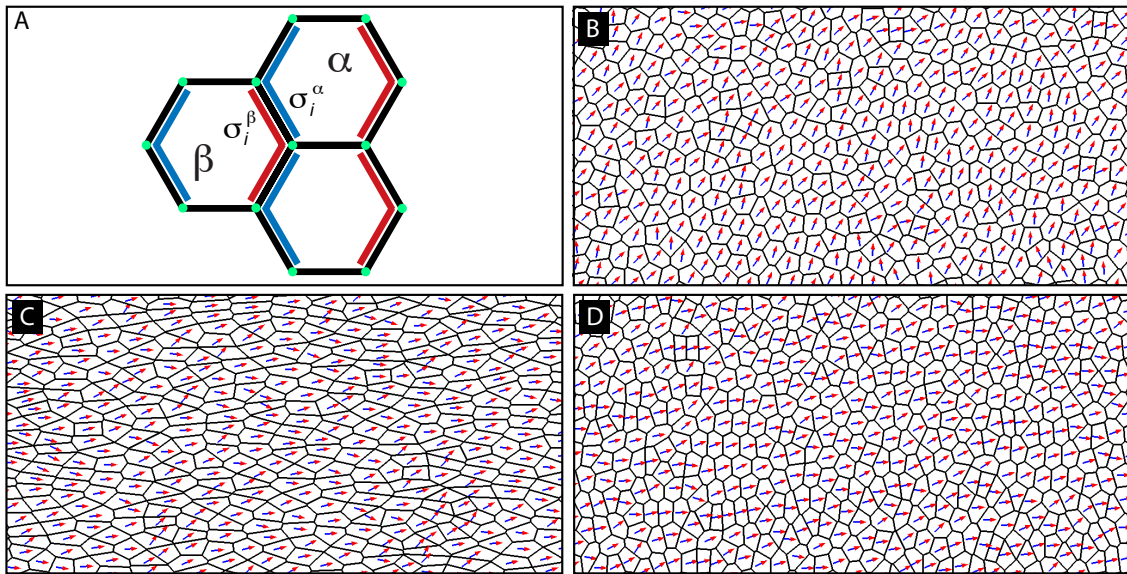


Figure 6.7: (A) PCP in the vertex model is represented using variables  $\sigma_i^\alpha$ , which describe the level of PCP proteins on bond  $i$  of cell  $\alpha$ . Each cell boundary  $i$  is shared by two cells  $\alpha$  and  $\beta$ ; the variables  $\sigma_i^\alpha$  and  $\sigma_i^\beta$  describe the protein levels on the two sides of the single cell boundary  $i$ . Here and in all panels proximal proteins corresponding to positive  $\sigma_i^\beta$  are represented by blue and distal proteins are shown in red. (B) Simulation of tissue growth in a vertex model including PCP dynamics. Arrows represent the direction of polarity. Parameter values:  $k_d\tau = 0.01$ ,  $J_2/J_1 = 0.5$  and  $J_3 = 0$ . (C) Reorientation of polarity caused by externally-imposed tissue shear. Parameter values:  $k_d\tau = 0.01$  and  $J_3/J_1 = 0.05$ . (D) Reorientation of polarity by oriented cell division. Parameter values:  $k_d\tau = 0.01$ ,  $J_3 = 0$ . Collaborative figure taken from [2].

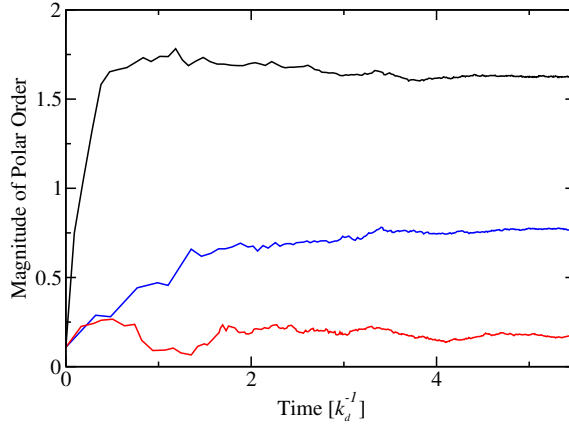


Figure 6.8: Magnitude of polar order in Vertex model simulations of polarity formation during growth, for three cell division rates  $k_d\tau = 0.01$  (black),  $k_d\tau = 0.1$  (blue), and  $k_d\tau = 1$  (red). Starting from a network of 36 cells with random polarity variables  $\sigma_i^\alpha$ , the magnitude of polar order increases within one cell-generation  $k_d^{-1}$  to reach its maximum value. For  $k_d\tau < 1$ , long-ranged polar order is maintained throughout development. Parameter values:  $J_2/J_1 = 0.5$  and  $J_3 = 0$ .

$J_1$ ,  $J_2$ , and  $J_3$  are parameters describing the strength of the three respective interactions. In addition to the potential  $E_{PCP}$ , the variables  $\sigma_i^\alpha$  are subjected to constraints. Firstly, the total number of proteins on cell boundaries is not expected to vary widely from cell to cell, and this fact is represented here using the constraint:

$$\sum_i (\sigma_i^\alpha)^2 = c, \quad (6.7)$$

where  $c$  is a constant. Secondly, each cell is assumed to have both types of proteins, in roughly equal amounts. This assumption is motivated by the fact that proximal and distal proteins play conjugate roles, with proteins of one type interacting across cell boundaries with proteins of the other type. This is captured here using the constraint:

$$\sum_i \sigma_i^\alpha = 0. \quad (6.8)$$

The time-evolution of PCP proteins is then described using a simple dynamic equation:

$$\frac{d\sigma_i^\alpha}{dt} = -k_{PCP} \frac{\partial \bar{E}_{PCP}}{\partial \sigma_i^\alpha}. \quad (6.9)$$

Here  $-k_{PCP}$  is a kinetic coefficient related to the PCP relaxation time  $\tau = 1/(k_{PCP}J_1)$  and

$$\bar{E}_{PCP} = - \sum_\alpha \psi_1^\alpha \sum_i \sigma_i^\alpha - \sum_\alpha \psi_2^\alpha \sum_i [(\sigma_i^\alpha)^2 - c], \quad (6.10)$$

where  $\psi_1^\alpha$  and  $\psi_2^\alpha$  are Lagrange multipliers used to impose the constraints.

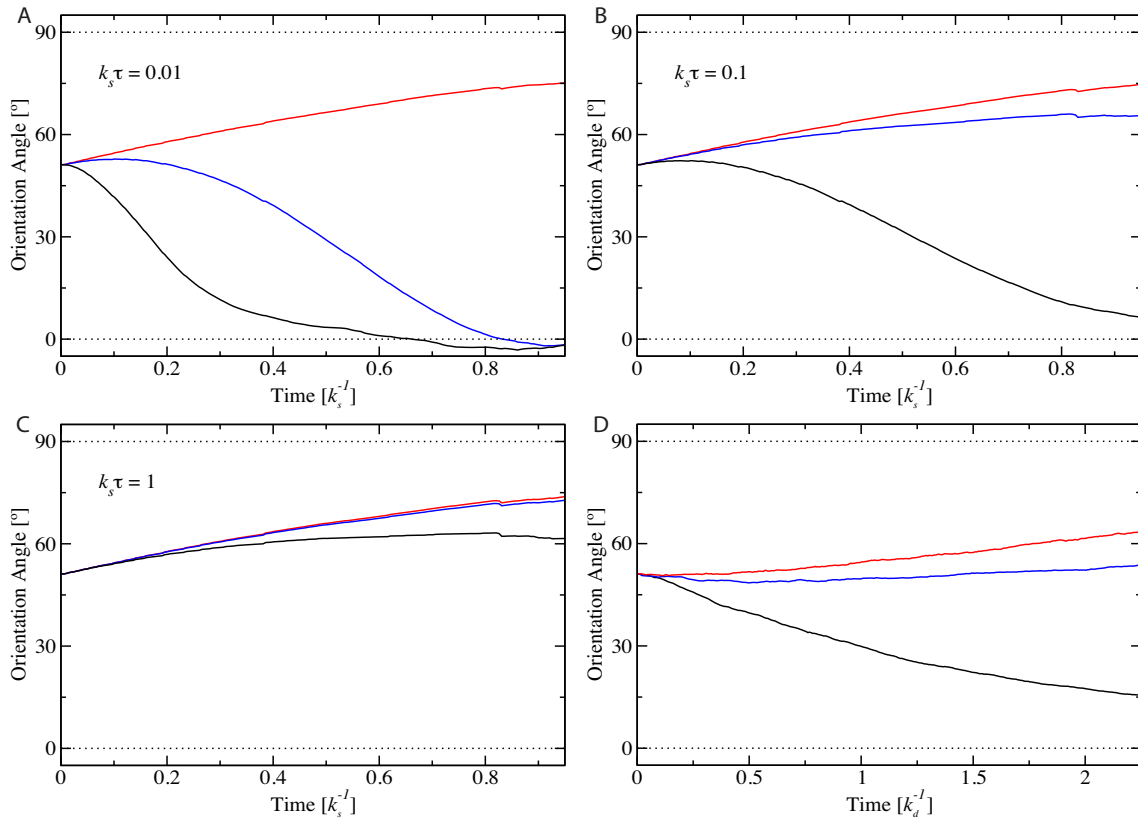


Figure 6.9: Simulations of polarity reorientation due to externally imposed shear and oriented cell division. (A-C) Starting from an initial condition with polarity at  $\sim 45$  degrees to the shear axis, Fig. 6.7B, external shear was applied by changing the aspect ratio of the periodic simulation box at fixed area. Curves are shown for three different couplings between polarity and cell elongation:  $J_3 = 0$  (red curves),  $J_3/J_1 = 0.05$  (blue curves) and  $J_3/J_1 = 0.5$  (black curves). Each set of curves is shown for three different shear rates:  $k_s \tau = 0.01$  (A),  $0.1$  (B) and  $1$  (C). Here  $k_s$  is the shear rate,  $\tau$  is the characteristic time for PCP relaxation, and only the product  $k_s \tau$  enters the present calculations. (D) Starting from the same initial condition as (A-C), shear induced by oriented cell division can also cause polarity reorientation, in this case with  $J_3 = 0$ . Three cell division rates are presented, namely  $k_d \tau = 0.01$  (black),  $k_d \tau = 0.1$  (blue) and  $k_d \tau = 1$  (red). Parameter common to all panels:  $J_2/J_1 = 0.5$ .

We present in Fig. 6.7 a vertex model calculation including PCP dynamics. Starting from an initial condition of 36 cells with random polarity variables, tissue growth was simulated using the methods of Chapter 3 while numerically solving PCP dynamics as described by Eq. 6.9. We see in Fig. 6.7B that a tissue grown in such a fashion results in global polar order free from polarity defects such as swirls. The magnitude of polar order as a function of time is presented in Fig. 6.8. Polar order is established first at the 36-cell stage, when the system is too small to support defects in the polarity pattern. This order is then maintained during development, resulting in the defect-free pattern in Fig. 6.7B. This is to be contrasted with a situation where polarity variables are assigned randomly to a tissue that has already been grown: in such a situation polarity patterns attain defects including swirls [71]. Note that there is no global biasing signal in these calculations: the emergent global polarity direction is determined randomly from fluctuations including stochastic cell divisions and the random initial condition. In the real experimental system the early polarity pattern could be determined by boundary conditions or any other symmetry breaking phenomenon.

We present in Fig. 6.7C-D two methods for reorienting polarity in vertex model simulations. In the first of these, shear is applied along the horizontal axis in Fig. 6.7C ( $\sim 45$  degrees to the initial polarity axis). Such shear is applied at a constant rate  $k_s$  by changing the aspect ratio of the periodic simulation box while maintaining constant area. This is performed in a quasistatic approximation, where the mechanical forces on the network were relaxed instantaneously throughout the calculation. In Fig. 6.7D, shear is generated by oriented cell division: new cell boundaries are drawn preferentially along the vertical axis, which results in shear along the horizontal axis. In both types of simulations polarity reorients parallel to the shear axis, see Fig. 6.7C-D. This behaviour depends on parameter values, as shown in Fig. 6.9.

## 6.3 Summary

Any pattern in a moving medium will move together with the medium. This simple idea can be used to derive hydrodynamic theories of polarity reorientation, which are well known in the context of liquid crystals [42, 152]. Here we develop a hydrodynamic theory of polarity reorientation in the fly wing. Due to the simplicity of the underlying arguments, hydrodynamic effects will be present in the real system, even if other biophysical mechanisms are also at work. This is most clear in the trivial coupling of PCP to patterns of local rotation. Here we find that that the magnitude and pattern of local rotation found in the wing accounts for PCP reorientation on the order of 77% of that observed in the real wing, measured in terms of the magnitude of final polar order. Coupling of PCP to patterns of shear may in general be nontrivial. However, due to symmetry arguments, any coupling between PCP and shear will have two fixed points, one parallel and one perpendicular to the shear axes. Only one of these fixed points can be stable, a fact captured by the

sign of the coefficient  $\nu$  in our hydrodynamic theory. In the real system as well as in hydrodynamic calculations, moving towards a stable fixed point can provide a robust mechanism for reorientation. By combining the effects of rotation and shear, we find that cell flow can account for over 90% of the reorientation observed in the fly wing. Finally, we present in Sect. 6.2 a cell-scale model of planar polarity in the vertex model. We find that shear in the vertex model is able to reorient polarity either parallel or perpendicular to the shear axis, consistent with the hydrodynamic theory of Sect. 6.1.

The hydrodynamic calculations presented in Sect. 6.1 are intentionally incomplete. In particular, we omit in our hydrodynamic equations the natural tendency for PCP to align, which could account for the remaining reorientation observed in the wing. Such a natural tendency would appear as terms involving the gradient of the polarity field. Here we omitted such terms in order to highlight the role of hydrodynamics in reorienting polarity.

While the research presented here was under review, a related paper discussing a different connection between hydrodynamic flow and polarity was published [153]. In that paper, Guirao *et al.* do not discuss the connection of cell flow and polarity during development, but rather hydrodynamic forces in the medium surrounding mammalian motile cilia coupling with planar polarity in those systems.

## 7 Conclusions

In this thesis we present a theoretical analysis of the vertex model for tissue mechanics and dynamics, and a theoretical description of planar cell polarity (PCP). The vertex model describes epithelia as networks of polygons, motivated by experimental images at the level of the adherens junctions. Here we analytically determine ground states of the vertex model, and derive a dynamic description of the model based on a balance between reactive and dissipative (frictional) forces. In order to determine tissue dynamics in experiments, we develop quantification methods for cell flow and planar polarity. Motivated by an analogy to the physics of liquid crystals, we show that cell flow reorients planar polarity in the developing wing of the fruit fly.

We present a wide range of methods and results throughout the thesis, including mathematical derivations, physical theories, and quantifications of experimental data. Firstly, in Chapter 2 we use the topological requirement that cells tile the plane to prove that the ground state of the vertex model is a hexagonal lattice in a region of parameter space, assuming tissue properties are homogeneous. This result demonstrates that topological requirements not only restrict the possible lattices that can be formed, but can actually determine the ground state of a cellular model. Our result extends and refines past work [69], which identified the key features of the phase diagram based on a combination of physical arguments and simulations.

Transition lines in the ground-state diagram coincide with changes in elastic properties including shear and compression moduli. In the region of parameter space where a hexagonal lattice is the ground state, cell shape is set by a balance between the cell's Young's modulus, elastically preferred shape, cell-cell adhesion, and stresses generated by a contractile actin-myosin ring. However, as cells are made sufficiently adhesive, it becomes possible to perfectly satisfy this balance, corresponding to an absolute minimum of the network potential or work function. This qualitative change is marked by a second-order phase transition to a region of degenerate ground states of irregular cells. This ground-state degeneracy allows the tissue to be continuously reshaped without increasing the potential energy, resulting in a vanishing shear modulus. This could be one mechanism among others [5] explaining why some real tissues show fluid-like behaviour, and others show predominantly solid-like behaviour. In one scenario, dominant contractile forces could push cells toward a hexagonal shape, minimizing cell-cell contact. However, if cells are sufficiently adhesive then other shapes with larger cell-cell contacts would be favoured over the hexagonal lattice. Such lattices are degenerate, allowing the possibility for

zero shear modulus and fluid-like behaviour.

In Chapter 3, we find that manifold vertices are typically unstable in the vertex model employed in this thesis, in the case of homogeneous tissue parameters. Surprisingly, vertices formed from junctions of as many as eleven cells are observed experimentally [101]. These manifold vertices or “rosettes” are associated with anisotropic, inhomogeneous distributions of actin-myosin contractility; our vertex model calculations imply that this inhomogeneous contractility is critical for their formation. Rosette formation is a striking, qualitative difference between cell networks in tissues and networks of foams, which only show threefold vertices in two dimensions [80]. It would be interesting to perform a detailed study of rosette formation using a combination of theory and experiment, in order to determine if inhomogeneous contractility is the sole mechanism for the formation of these seemingly paradoxical objects.

In addition to the formation and decomposition of manifold vertices, other topological processes are investigated in Chapter 3 including cell extrusion, cell division, and tissue growth. In previous work [69], tissue growth simulations were presented where cells would double in area, divide, and quasistatically relax to a force-balanced state. Here, in Chapter 3, we show that a simplified algorithm that omits the area-doubling phase gives very similar results. We furthermore introduce simplified rules for cell-boundary rearrangement (T1 transitions), finding indistinguishable results as compared to the previous algorithm. These simplifications hint towards a separation of timescales: if growth simulations are performed quasistatically, then one does not expect the reaction pathway on the timescale of single cell divisions to significantly affect the results. In order to go beyond the quasistatic approximation, in Chapter 4 we develop a dynamic description of the vertex model based on the balance of reactive and dissipative (frictional) forces. This description allows friction coefficients to be incorporated into the vertex model that couple to different types of motion, for example changes in cell bond lengths or areas. Here we use this dynamic description in order to determine relaxation modes and predict the emergence of the quasistatic limit, which is verified in numerical calculations. This dynamic description would also be well suited to investigating laser ablation experiments, where tissues are cut using a laser and the relaxation is observed [69, 154, 155].

In order to investigate the dynamics of tissues in experiments, we present in Chapter 5 quantification methods for determining cell flow and planar polarity based on confocal microscope images of the wing of the fruit fly. Noting that a polarity pattern in an inhomogeneously flowing tissue will necessarily reorganize, we develop a hydrodynamic theory of polarity reorientation in Chapter 6. Such theories are well known in the physics of liquid crystals, which order in response to shear flow. Using this combination of quantification and theoretical calculations, we show that cell flow is a key mechanism for reorienting polarity patterns during development. In general, polarity is ubiquitous in cells and tissues [102]. For instance, epithelial cells typically display polarity both in the apical-basal direction (perpendicular to the plane of the epithelium), and also in the plane of the epithelium (PCP). In humans, defective

PCP signalling has been implicated in polycystic kidney disease, possibly due to improper ciliary function [102]. The hydrodynamic theory of polarity reorientation presented in this thesis is highly general, being based on simple physical arguments. Thus, we hope that the present theory will be applied to diverse systems in order to understand tissue polarity in a broader context.



# A Ground states of the vertex model

## A.1 Networks of identical cells

We first determine the ground state of networks of identically shaped cells. Networks of identically shaped cells can only be  $n$ -sided polygons with  $n = 3, 4, 5$  or  $6$ . Note that, due to the restriction of average neighbour number, networks of identically shaped cells with  $n = 3, 4$  or  $5$  must contain fourfold or manyfold vertices. As shown in Sect. 2.2.1, for  $\bar{\Lambda} < -2^{5/2}3^{1/4}\bar{\Gamma}$  the lowest potential energy of individual polygons corresponds to irregular polygons with preferred area and perimeter. Similarly, it was shown that if

$$\bar{\Lambda} \geq 2 \cdot 3^{-5/2}(\sqrt{3} - 12\bar{\Gamma})^{3/2} \quad (\bar{\Gamma} < \sqrt{3}/12) \quad (\text{A.1})$$

or

$$\bar{\Lambda} \geq 0 \quad (\bar{\Gamma} \geq \sqrt{3}/12) \quad (\text{A.2})$$

then the lowest potential of individual polygons corresponds to collapsed cells with  $a = 0$ . These results also apply for networks of identical polygons. For values of  $\bar{\Lambda}$  between these two cases, a regular hexagon of minimal  $e$  has a lower potential than any other  $n$ -sided polygon with  $n \leq 6$ . Interestingly, for  $\bar{\Lambda} \geq 0$  this fact also follows directly from the so-called ‘‘Honeycomb Conjecture’’, which states that a network of regular hexagons has the smallest perimeter of any periodic tiling of equal area regions [156]. These arguments define the ground states of networks of identical cells, depending on the values of  $\bar{\Lambda}$  and  $\bar{\Gamma}$ , see Table A.1.

## A.2 General networks of cells

We now consider all possible networks and determine the ground states of  $\bar{F}$ . For  $\bar{\Lambda} < -2^{5/2}3^{1/4}\bar{\Gamma}$  any state for which all cells have area  $a = 1$  and perimeter  $p = p_0$  is a ground state of the system. In the following we only consider parameter values with  $\bar{\Lambda} \geq -2^{5/2}3^{1/4}\bar{\Gamma}$ .

The ground state of all networks composed of  $n$ -sided polygons with  $n \leq 6$  is a perfect hexagonal network with optimized areas. This follows because an optimal

Parameter Values		Ground State (Identical Cells)
$\bar{\Lambda} < \bar{\Lambda}_I$	–	irregular polygons ( $a = 1, p = p_0$ )
$\bar{\Lambda}_I \leq \bar{\Lambda} < \bar{\Lambda}_{II}$	$\bar{\Gamma} < \sqrt{3}/12$	} hexagonal lattice
$\bar{\Lambda}_I \leq \bar{\Lambda} < 0$	$\bar{\Gamma} \geq \sqrt{3}/12$	
$\bar{\Lambda} \geq \bar{\Lambda}_{II}$	$\bar{\Gamma} < \sqrt{3}/12$	} collapsed lattice ( $a = 0, p = 0$ )
$\bar{\Lambda} \geq 0$	$\bar{\Gamma} \geq \sqrt{3}/12$	

Table A.1: Ground states of the potential energy  $\bar{F}$  of networks of identically shaped cells as a function of the dimensionless line tension  $\bar{\Lambda}$  and perimeter elasticity  $\bar{\Gamma}$ . For  $\bar{\Lambda} < \bar{\Lambda}_I$  the ground states are degenerate, consisting of identical irregular polygons with  $a = 1$  and  $p = p_0$ . For  $\bar{\Lambda} \geq \bar{\Lambda}_{II}$  the ground state is a collapsed network of cells with zero area. Here  $\bar{\Lambda}_I = -2^{5/2}3^{1/4}\bar{\Gamma}$  and  $\bar{\Lambda}_{II} = 2 \cdot 3^{-5/2}(\sqrt{3} - 12\bar{\Gamma})^{3/2}$ .

hexagon has a lower potential than any other  $n$ -gon with  $n \leq 6$ . The problem is nontrivial in the case where some polygons have  $n > 6$  sides. Because for periodic boundary conditions the average neighbour number  $\langle n \rangle$  in an arbitrary network is  $\langle n \rangle \leq 6$ , any  $n$ -gon with  $n > 6$  must be balanced by a number of  $n$ -gons with  $n < 6$ . We use this fact to determine a lower bound  $\Delta_{net}(n) + e_6$  of the potential of networks containing cells with  $n > 6$ , where  $e_6$  denotes the optimal energy of regular hexagons.

For a network containing an  $n > 6$ -sided cell, the average neighbour number can be less than or equal to 6 if the network also contains  $n - 6$  pentagons,  $(n - 6)/2$  quadrilaterals, or  $(n - 6)/3$  triangles. Combinations of triangles, quadrilaterals, and pentagons are also possible. A lower bound on the potential difference between such a network and one containing only regular hexagons is given by:

$$\Delta_{net}(n) = \Delta_n + (n - 6) \min \left[ \Delta_5, \frac{\Delta_4}{2}, \frac{\Delta_3}{3} \right], \quad (\text{A.3})$$

where  $\Delta_n = e_n - e_6$ . Here  $e_n$  is the lowest energy  $e$  of an  $n$ -sided polygon given  $\bar{\Lambda}$  and  $\bar{\Gamma}$ . Note that as shown in Sect. 2.2.1, the corresponding optimal polygon shape is either a regular  $n$ -sided polygon, an irregular polygon with  $a = 1$  and  $p = p_0$ , or a collapsed cell ( $a = 0, p = 0$ ). If  $\Delta_{net}(n) > 0$ , then any network constructed using cells with six or fewer sides together with cells with  $n > 6$  sides will have a higher potential than the hexagonal lattice. If  $\Delta_{net}(n) > 0$  for all  $n > 6$  then the optimal hexagonal network is the ground state of the system for the given parameter values.

We note that  $e_n$  is monotonically decreasing with  $n$ , so that

$$\Delta_{\text{net}}(n') \geq \Delta_{\text{net}}(n) + e_\infty - e_n \quad (\text{A.4})$$

for all  $n' \geq n$ , where

$$e_\infty = \lim_{n \rightarrow \infty} e_n. \quad (\text{A.5})$$

The procedure for showing that the hexagonal lattice is the ground state for a particular set of parameter values  $(\bar{\Lambda}, \bar{\Gamma})$  is as follows. Starting at  $n = 7$ , we check the inequality  $\Delta_{\text{net}}(n) > 0$  for increasing values of  $n$ . If  $\Delta_{\text{net}}(n) < 0$  for any  $n$ , the hexagonal network may not be the ground state. If for  $\Delta_{\text{net}}(n) > 0$  we also find  $\Delta_{\text{net}}(n) + e_\infty - e_n > 0$  then the hexagonal network is proven to be the ground state, and larger  $n$  do not need to be considered. We continue checking these two inequalities for increasing values of  $n$ , until either  $\Delta_{\text{net}}(n) < 0$  for some  $n$ , and no conclusions can be drawn, or  $\Delta_{\text{net}}(n) + e_\infty - e_n > 0$ , and thus the hexagonal lattice is shown to be the ground state.

We have applied these arguments numerically at each set of parameter values  $(\bar{\Lambda}, \bar{\Gamma})$  in the ranges  $-1.5 \leq \bar{\Lambda} \leq 0.5$ ,  $0 \leq \bar{\Gamma} \leq 0.2$  in increments of  $\Delta\bar{\Lambda} = \Delta\bar{\Gamma} = 10^{-4}$ . We find that the hexagonal lattice is the ground-state network of the vertex model everywhere in the part of region (II) of Figs. 2.1a and 2.1b that is exterior to the dotted lines.



# B Topological processes and tissue growth

## B.1 Topological changes

When the potential energy  $F$  is minimized by a conjugate gradient procedure, a cell bond can shrink to zero length and the network undergo a T1-transition. Similarly, a cell can shrink to zero area and induce a T2-transition.

### B.1.1 T1 transitions

**Method A.** Each bond  $k$  is assigned a state variable  $\sigma_k$ , which can take the values 0 or 1. Initially  $\sigma_k = 1$  for all bonds. The algorithm consists of the following steps, applied at each iteration of energy minimization: (i) A T1 transition is performed whenever a bond with  $\sigma_k = 1$  shrinks below a cutoff length  $l_{\min}$ , i.e. if  $l_k < l_{\min}$ . After the transition this bond no longer exists, and the newly created bond is assigned  $\sigma_k = 0$ . (ii) For all bonds with  $l_k \geq l_{\min}$  we set  $\sigma_k = 1$ .

**Method B** is the algorithm used in Ref. [69]. The algorithm consists of the following steps, applied at each iteration of energy minimization: (i) For each bond with  $l_k < l_{\min}$  we determine  $F_+$  and  $F_-$ , the energies corresponding to network configurations due to right-handed and left-handed T1 transitions, see Fig. B.1. (ii) The network with the lowest potential value  $F_0$ ,  $F_+$ , or  $F_-$  is chosen, where  $F_0$  is the energy of the initial network, see Fig. B.1. This implies that a T1 transition occurs whenever  $F_+$  or  $F_-$  is below  $F_0$ .

**Method C** is similar to **Method B**, except that  $F_+$  and  $F_-$  are determined after an additional relaxation, which keeps all vertices fixed except for the two vertices  $i$  and  $j$  involved in the T1 transition, see Fig. B.1.

We find that polygon distributions and cell area variations are indistinguishable for tissues obtained using these three algorithms (data not shown). The simplest algorithm presented here (**Method A**) is more robust to numerical implementation than methods **B** and **C**, because methods **B** and **C** require precise computation of small potential changes  $F_+ - F_0$  and  $F_- - F_0$ .

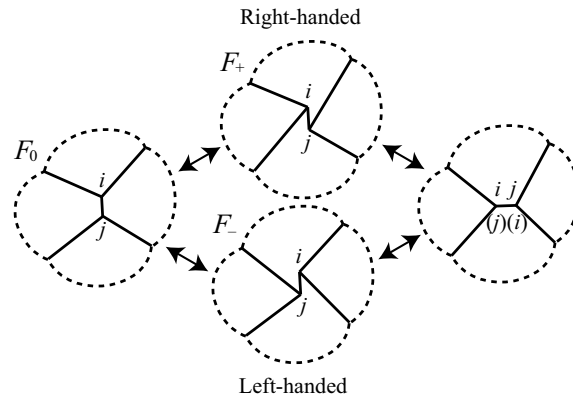


Figure B.1: Schematic representation of T1 transitions as implemented in the numerical algorithm described in App. B.1. Labels indicate vertices  $i$  and  $j$ , which are connected by a bond  $k$  undergoing a T1 transition (bond not labelled).

### B.1.2 T2 transitions

T2-transitions are accounted for by replacing a cell  $\alpha$  with  $A_\alpha < A_{\min}$  with a vertex, where  $A_{\min}$  is an area cutoff.

## B.2 Comparison of growth algorithms

Algorithm II for quasistatic cell division introduced in this paper is a simplified version of Algorithm I, which was used in Ref. [69], see Sect. 3.3. We show in Fig. B.2 that these two growth algorithms give very similar results (compare solid and dashed lines).

Note that the polygon distributions shown in Ref. [69] differ slightly from the dashed line in Fig. B.2, which is obtained using the same algorithm. Reasons for this are: (i) A length cutoff was used when defining neighbour numbers in Ref. [69], which is necessary when comparing with experiment. No such cutoff is used here. (ii) In Ref. [69] a single network containing  $10^4$  cells was used, whereas here we use  $10^3$  networks (dashed line in Fig. B.2) and  $10^4$  networks (solid line) containing  $\sim 110$  cells each. This implies a larger statistical error in Ref. [69] compared to Fig. B.2. (iii) There are additional numerical inaccuracies in Ref. [69].

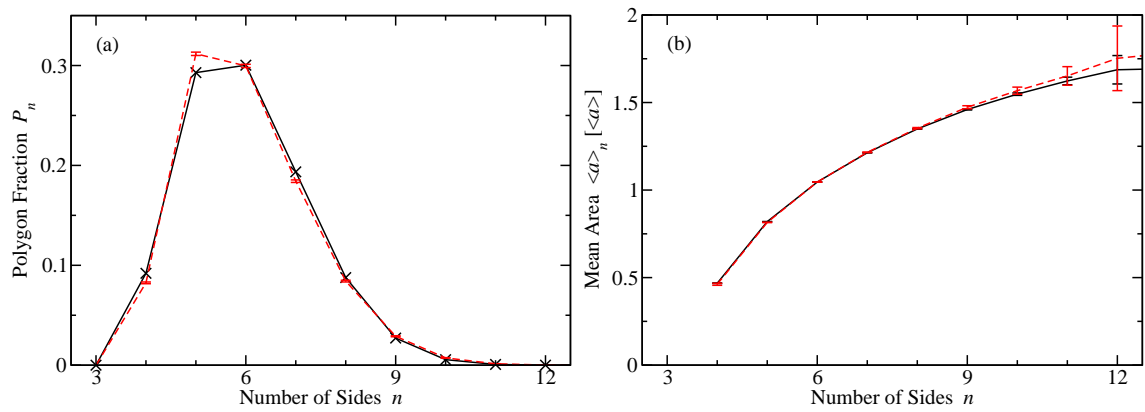


Figure B.2: Comparison of algorithms I (dashed red lines) and II (solid black lines), which use different rules for cell division, for  $(\bar{\Lambda}, \bar{\Gamma}) = (0.12, 0.04)$ . (a) Fraction of  $n$ -sided polygons as a function of cell neighbour number  $n$ . (b) Average area of  $n$ -sided polygons, normalized by the average area of cells in the network, for the same simulations shown in (a). The solid black lines in (a) and (b) are the same as in Figs. 3.4a and 3.4b.



## C Collaborative contributions

The research related to planar cell polarity presented in this thesis would have been impossible without the combined effort of physicists and biologists working on the same problem. Such collaboration is a strength of this thesis: because of our aggregate effort, our results were of sufficient quality to warrant publication in the journal *Cell*. Due to the degree of collaboration, lines between contributions of different authors were occasionally blurred. This is partly due to the nature of an interdisciplinary field such as biophysics, and partly because of the inherently collaborative design of the undertaken research. This is at odds with a historical doctoral system where a student might have worked alone for several years. Correspondingly, the author wishes to clarify in this appendix which parts of this thesis benefited from collaborative work and how. Such clarifications are also made redundantly throughout the text.

The research presented in this thesis on planar cell polarity was published in [2]. The author list on that paper was B. Aigouy, R. Farhadifar, D. B. Staple, A. Sagner, J.-C. Röper, F. Jülicher, and S. Eaton. Of these authors, R. Farhadifar and myself were theoretical physicists working in the group of F. Jülicher here at MPI-PKS, Dresden. B. Aigouy, A. Sagner, and J.-C. Röper were experimental biologists working in the group of S. Eaton at MPI-CBG, Dresden. Theoretical efforts were roughly divided between R. Farhadifar and myself under the supervision of F. Jülicher, with R. Farhadifar responsible for vertex model calculations of planar cell polarity (presented in Sect. 6.2) and myself responsible for the quantifications and theory of cell flow and planar polarity presented in Chapter 5 and Sect. 6.1. I contributed analysis of the vertex model simulations performed by R. Farhadifar; for example the curves plotted in Figs. 6.8 and 6.9 were computed by the present author based on raw data provided by R. Farhadifar. Such figures were truly a collaborative effort.

The computations necessary to produce Fig. 5.7 were also highly collaborative. The present author designed the algorithm presented in Sect. 5.2 based on an early algorithm developed by R. Farhadifar and F. Jülicher. The present author then wrote software for implementing the algorithm, and sent this software to B. Aigouy for integration into cell-segmentation software that was used in previous work [69]. B. Aigouy ran the combined software and prepared the final images presented in Fig. 5.7A-E.

Work for final figure preparation was distributed throughout the collaborative

efforts. Final versions of figures that both contained both experimental images of fly wings and the results of theoretical calculations were typically prepared by B. Aigouy, even where the author developed the theoretical tools and wrote the numerical routines used to perform the calculations. For example, in the case of Fig. 5.2, the author wrote software for computing the cell velocity and derivative fields. Said software was used to prepare preliminary versions of the panels in Fig. 5.2 as well as the associated videos. These preliminary versions of the figures together with figure specifications were sent to B. Aigouy, who prepared the final version of Fig. 5.2. In total, Figs. 5.1, 5.2, 5.7, 6.1, 6.4, and 6.5 were prepared by B. Aigouy. Fig. 6.7 was prepared by R. Farhadifar, and 5.5 was created by the present author based on Fig. 5.2C, which was in turn prepared by B. Aigouy.

# Bibliography

- [1] D. B. Staple, R. Farhadifar, J.-C. Röper, B. Aigouy, S. Eaton, and F. Jülicher. Mechanics and remodelling of cell packings in epithelia. *Eur. Phys. J. E*, 33(2):117–127, 2010.
- [2] B. Aigouy, R. Farhadifar, D. B. Staple, A. Sagner, J.-C. Röper, F. Jülicher, and S. Eaton. Cell flow reorients the axis of planar polarity in the wing epithelium of *Drosophila*. *Cell*, 142(5):773–786, 2010.
- [3] U.S. National Library of Medicine Medical Subject Headings. <http://www.nlm.nih.gov/mesh/> Accessed Feb. 28, 2011. Keywords: tissues, connective tissue, bone and bones.
- [4] Oxford English Dictionary. <http://www.oed.com/> Accessed Jul. 4, 2011. Keyword: tissue.
- [5] J. Ranft, M. Basan, J. Elgeti, J.-F. Joanny, J. Prost, and F. Jülicher. Fluidization of tissues by cell division and apoptosis. *Proc. Nat. Acad. Sci.*, 107(49):20863–20868, 2010.
- [6] M. S. Steinberg. On the mechanism of tissue reconstruction by dissociated cells, I. Population kinetics, differential adhesiveness, and the absence of directed migration. *Proc. Nat. Acad. Sci.*, 48(9):1577–1582, 1962.
- [7] M. S. Steinberg. Mechanism of tissue reconstruction by dissociated cells, II: Time-course of events. *Science*, 137(3532):762–763, 1962.
- [8] M. S. Steinberg. On the mechanism of tissue reconstruction by dissociated cells, III. Free energy relations and the reorganization of fused, heteronomic tissue fragments. *Proc. Nat. Acad. Sci.*, 48(10):1769–1776, 1962.
- [9] M. S. Steinberg. Reconstruction of tissues by dissociated cells. *Science*, 141(3579):401–408, 1963.
- [10] M. S. Steinberg. Does differential adhesion govern self-assembly processes in histogenesis? Equilibrium configurations and the emergence of a hierarchy among populations of embryonic cells. *J. Exptl. Zool.*, 173(4):395–433, 1970.

- 
- [11] M. S. Steinberg. Differential adhesion in morphogenesis: a modern view. *Curr. Opin. Genetics Dev.*, 17(4):281–286, 2007.
- [12] H. V. Wilson. On some phenomena of coalescence and regeneration in sponges. *J. Exptl. Zool.*, 5(2):245–258, 1907.
- [13] J. Holtfreter. Experimental studies on the development of the pronephros. *Rev. Can. Biol.*, 3:220–250, 1944.
- [14] A. Moscona. Cell suspensions from organ rudiments of chick embryos. *Exp. Cell Res.*, 3(3):535–539, 1952.
- [15] A. Moscona. Cell suspensions from organ rudiments of chick embryos. *J. Anat.*, 86(3):287–301, 1952.
- [16] J. P. Trinkaus and P. W. Groves. Differentiation in culture of mixed aggregates of dissociated tissue cells. *Proc. Nat. Acad. Sci.*, 41(10):787–795, 1955.
- [17] P. L. Townes and J. Holtfreter. Directed movements and selective adhesion of embryonic amphibian cells. *J. Exptl. Zool.*, 128(1):53–120, 1955.
- [18] A. Moscona. Development of heterotypic combinations of dissociated embryonic chick cells. *Proc. Soc. Exp. Biol. Med.*, 92(2):410–416, 1956.
- [19] A. Moscona. The development in vitro of chimeric aggregates of dissociated embryonic chick and mouse cells. *Proc. Nat. Acad. Sci.*, 43(1):184–194, 1957.
- [20] J. Holtfreter. Gewebeaffinität: Ein Mittel der embryonalen Formbildung. *Arch. Exptl. Zellforsch. Gewebezücht.*, 139(1):110–190, 1939.
- [21] Johannes Holtfreter. Studien zur Ermittlung der Gestaltungspaktoren in der Organentwicklung der Amphibien. *Arch. Entwicklungsmech. Organ.*, 139(1):110–190, 1939.
- [22] P. Weiss. The problem of specificity in growth and development. *Yale J. Biol. Med.*, 19(3):235–278, 1947.
- [23] M. S. Steinberg. On the chemical bonds between animal cells. A mechanism for type-specific association. *Amer. Nat.*, 92(863):65–81, 1958.
- [24] D. A. Beysens, G. Forgacs, and J. A. Glazier. Cell sorting is analogous to phase ordering in fluids. *Proc. Nat. Acad. Sci.*, 97(17):9467–9471, 2000.
- [25] R. Grima and S. Schnell. Can tissue surface tension drive somite formation? *Dev. Biol.*, 307(2):248–257, 2007. ISSN 0012-1606.
- [26] M. Basan, T. Risler, J.-F. Joanny, X. Sastre-Garau, and J. Prost. Homeostatic competition drives tumor growth and metastasis nucleation. *HFSP J.*, 3(4):265–272, 2009.

- 
- [27] M. Basan, J.-F. Joanny, J. Prost, and T. Risler. Undulation instability of epithelial tissues. *Phys. Rev. Lett.*, 106(15):158101, 2011.
- [28] Y. C. Fung. *Biomechanics: Mechanical Properties of Living Tissues*. Springer-Verlag New York, Inc., 2nd edition, 1993.
- [29] W. A. Malik, S. C. Prasad, K. R. Rajagopal, and L. Preziosi. On the modeling of the viscoelastic response of embryonic tissues. *Math. Mech. Solids*, 13(1): 81–91, 2008.
- [30] L. Preziosi, D. Ambrosi, and C. Verdier. An elasto-visco-plastic model of cell aggregates. *J. Theor. Biol.*, 262(1):35–47, 2010.
- [31] L. Preziosi and A. Farina. On Darcy’s law for growing porous media. *Int. J. Nonlinear Mech.*, 37(3):485–491, 2002.
- [32] C. Verdier, J. Etienne, A. Duperray, and L. Preziosi. Review: Rheological properties of biological materials. *C. R. Phys.*, 10(8):790–811, 2009.
- [33] D. Ambrosi, L. Preziosi, and G. Vitale. The insight of mixtures theory for growth and remodeling. *Z. Angew. Math. Phys.*, 61(1):177–191, 2010.
- [34] A. Chauvière, T. Hillen, and L. Preziosi. Modeling the motion of a cell population in the extracellular matrix. *Discr. Cont. Dyn. Sys. (Supplement)*, (Special Issue):250–259, 2007.
- [35] A. Chauvière, T. Hillen, and L. Preziosi. Modeling cell movement in anisotropic and heterogeneous network tissues. *Netw. Heterog. Media*, 2(2): 333–357, 2007.
- [36] A. Chauvière and L. Preziosi. Mathematical framework to model migration of cell population in extracellular matrix. In A. Chauvière, L. Preziosi, and C. Verdier, editors, *Cell Mechanics: From Single Scale-Based Models to Multiscale Modeling*, pages 279–312. CRC Press, 2010.
- [37] A. Chauvière, L. Preziosi, and H. Byrne. A model of cell migration within the extracellular matrix based on a phenotypic switching mechanism. *Math. Med. Biol.*, 27(3):255–281, 2010.
- [38] K. Kruse, J.-F. Joanny, F. Jülicher, J. Prost, and K. Sekimoto. Asters, vortices, and rotating spirals in active gels of polar filaments. *Phys. Rev. Lett.*, 92(7):078101, 2004.
- [39] K. Kruse, J.-F. Joanny, F. Jülicher, J. Prost, and K. Sekimoto. Generic theory of active polar gels: a paradigm for cytoskeletal dynamics. *Eur. Phys. J. E*, 16(1):5–16, 2005.

- 
- [40] J.-F. Joanny. Active behavior of the cell cytoskeleton. *Progr. Theoret. Phys. Suppl.*, 165:100–102, 2006.
- [41] R. Voituriez, J.-F. Joanny, and J. Prost. Generic phase diagram of active polar films. *Phys. Rev. Lett.*, 96(2):028102, 2006.
- [42] J.-F. Joanny, F. Jülicher, K. Kruse, and J. Prost. Hydrodynamic theory for multi-component active polar gels. *New J. Phys.*, 9(11):422, 2007.
- [43] F. Jülicher, K. Kruse, J. Prost, and J.-F. Joanny. Active behavior of the cytoskeleton. *Phys. Rep.*, 449(1-3):3–28, 2007.
- [44] J.-F. Joanny and J. Prost. Active gels as a description of the actin-myosin cytoskeleton. *HFSP J.*, 3(2):94–104, 2009.
- [45] T. B. Liverpool, M. C. Marchetti, J.-F. Joanny, and J. Prost. Mechanical response of active gels. *Europhys. Lett.*, 85(1):18007, 2009.
- [46] G. Salbreux, J. Prost, and J.-F. Joanny. Hydrodynamics of cellular cortical flows and the formation of contractile rings. *Phys. Rev. Lett.*, 103(5):058102, 2009.
- [47] J. Elgeti, M. E. Cates, and D. Marenduzzo. Defect hydrodynamics in 2D polar active fluids. *Soft Matt.*, 7(7):3177–3185, 2011.
- [48] D. Drasdo, R. Kree, and J. S. McCaskill. Monte Carlo approach to tissue-cell populations. *Phys. Rev. E*, 52(6):6635–6657, 1995.
- [49] D. Drasdo and G. Forgacs. Modeling the interplay of generic and genetic mechanisms in cleavage, blastulation, and gastrulation. *Dev. Dynam.*, 219(2):182–191, 2000.
- [50] D. Drasdo. Buckling instabilities of one-layered growing tissues. *Phys. Rev. Lett.*, 84(18):4244–4247, 2000.
- [51] D. Drasdo and M. Loeffler. Individual-based models to growth and folding in one-layered tissues: Intestinal crypts and early development. *Nonlinear Anal.*, 47(1):245–256, 2001.
- [52] D. Drasdo and S. Höhme. Individual-based approaches to birth and death in avascular tumors. *Math. Comp. Model.*, 37(11):1163–1175, 2003.
- [53] D. Drasdo. Coarse graining in simulated cell populations. *Adv. Complex Syst.*, 08(02):319–363, 2005.
- [54] D. Drasdo and S. Höhme. A single-cell-based model of tumor growth *in vitro*: monolayers and spheroids. *Phys. Biol.*, 2(3):133, 2005.

- 
- [55] J. Galle, M. Loeffler, and D. Drasdo. Modeling the effect of deregulated proliferation and apoptosis on the growth dynamics of epithelial cell populations in vitro. *Biophys. J.*, 88(1):62–75, 2005.
- [56] J. Galle, G. Aust, G. Schaller, T. Beyer, and D. Drasdo. Individual cell-based models of the spatial-temporal organization of multicellular systems—Achievements and limitations. *Cytom. Part A*, 69A(7):704–710, 2006.
- [57] M. Block, E. Schöll, and D. Drasdo. Classifying the expansion kinetics and critical surface dynamics of growing cell populations. *Phys. Rev. Lett.*, 99(24):248101, 2007.
- [58] D. Drasdo, S. Höhme, and M. Block. On the role of physics in the growth and pattern formation of multi-cellular systems: What can we learn from individual-cell based models? *J. Stat. Phys.*, 128(1):287–345, 2007.
- [59] S. Höhme, J. G. Hengstler, M. Brulport, M. Schäfer, A. Bauer, R. Gebhardt, and D. Drasdo. Mathematical modelling of liver regeneration after intoxication with  $\text{CCl}_4$ . *Chem.-Biol. Interact.*, 168(1):74–93, 2007.
- [60] H. Byrne and D. Drasdo. Individual-based and continuum models of growing cell populations: a comparison. *J. Math. Biol.*, 58(4):657–687, 2009.
- [61] M. Radszuweit, M. Block, J. G. Hengstler, E. Schöll, and D. Drasdo. Comparing the growth kinetics of cell populations in two and three dimensions. *Phys. Rev. E*, 79(5):051907, 2009.
- [62] I. Ramis-Conde, M. A. J. Chaplain, A. R. A. Anderson, and D. Drasdo. Multi-scale modelling of cancer cell intravasation: the role of cadherins in metastasis. *Phys. Biol.*, 6(1):016008, 2009.
- [63] S. Höhme and D. Drasdo. A cell-based simulation software for multi-cellular systems. *Bioinformatics*, 26(20):2641–2642, 2010.
- [64] S. Höhme and D. Drasdo. Biomechanical and nutrient controls in the growth of mammalian cell populations. *Math. Popul. Stud.*, 17(3):166–187, 2010.
- [65] M. Basan, J. Prost, J.-F. Joanny, and J. Elgeti. Dissipative particle dynamics simulations for biological tissues: rheology and competition. *Phys. Biol.*, 8(2):026014, 2011.
- [66] M. C. Gibson, A. B. Patel, R. Nagpal, and N. Perrimon. The emergence of geometric order in proliferating metazoan epithelia. *Nature*, 442(7106):1038–1041, 2006.
- [67] R. Nagpal, A. B. Patel, and M. C. Gibson. Epithelial topology. *BioEssays*, 30(3):260–266, 2008.

- 
- [68] A. B. Patel. *Modeling and Inferring Cleavage Patterns in Proliferating Epithelia*. PhD thesis, Harvard University, 2008.
- [69] R. Farhadifar, J.-C. Röper, B. Aigouy, S. Eaton, and F. Jülicher. The influence of cell mechanics, cell-cell interactions, and proliferation on epithelial packing. *Curr. Biol.*, 17(24):2095–2104, 2007.
- [70] U.S. National Library of Medicine Medical Subject Headings. <http://www.nlm.nih.gov/mesh/> Accessed Feb. 28, 2011. Keywords: cadherins, adherens junctions.
- [71] R. Farhadifar. *Dynamics of Cell Packing and Polar Order in Developing Epithelia*. PhD thesis, Technische Universität Dresden, 2009.
- [72] T. Nagai, K. Kawasaki, and K. Nakamura. Vertex dynamics of two-dimensional cellular patterns. *J. Phys. Soc. Jpn.*, 57(7):2221–2224, 1988.
- [73] M. Weliky and G. Oster. The mechanical basis of cell rearrangement. I. Epithelial morphogenesis during *Fundulus* epiboly. *Development*, 109(2):373–386, 1990.
- [74] T. Nagai and H. Honda. A dynamic cell model for the formation of epithelial tissues. *Phil. Mag. B*, 81(7):699–719, 2001.
- [75] T. Nagai and H. Honda. Computer simulation of wound closure in epithelial tissues: Cell–basal-lamina adhesion. *Phys. Rev. E*, 80(6):061903, 2009.
- [76] K. P. Landsberg, R. Farhadifar, J. Ranft, D. Umetsu, T. J. Widmann, T. Bittig, A. Said, F. Jülicher, and C. Dahmann. Increased cell bond tension governs cell sorting at the *Drosophila* anteroposterior compartment boundary. *Curr. Biol.*, 19(22):1950–1955, 2009.
- [77] T. Aegerter-Wilmsen, A. C. Smith, A. J. Christen, C. M. Aegerter, E. Hafen, and K. Basler. Exploring the effects of mechanical feedback on epithelial topology. *Development*, 137(3):499–506, 2010.
- [78] P. Mumcu. *Self-Organized Growth in Developing Epithelia*. PhD thesis, Technische Universität Dresden, 2011.
- [79] O. Wartlick, P. Mumcu, A. Kicheva, T. Bittig, C. Seum, F. Jülicher, and M. González-Gaitán. Dynamics of Dpp signaling and proliferation control. *Science*, 331(6021):1154–1159, 2011.
- [80] J. Plateau. *Statique expérimentale et théorique des Liquides soumis aux seules Forces moléculaires*. Paris, Gauthier-Villars; London, Trübner & Co.; Gand et Leipzig, F. Clemm, 1873.

- 
- [81] J. E. Taylor. The structure of singularities in soap-bubble-like and soap-film-like minimal surfaces. *Ann. Math.*, 103(3):489–539, 1976.
- [82] K. Kawasaki, T. Nagai, and K. Nakashima. Vertex models for two-dimensional grain growth. *Phil. Mag. B*, 60(3):399–421, 1989.
- [83] K. Nakashima, T. Nagai, and K. Kawasaki. Scaling behavior of two-dimensional domain growth: Computer simulation of vertex models. *J. Stat. Phys.*, 57(3):759–787, 1989.
- [84] T. Okuzono and K. Kawasaki. Intermittent flow behavior of random foams: A computer experiment on foam rheology. *Phys. Rev. E*, 51(2):1246–1253, 1995.
- [85] R. L. Fullman. Boundary migration during grain growth. In *Metal Interfaces*, pages 179–207. American Society for Metals, Cleveland, 1952.
- [86] A. Soares, A. C. Ferro, and M. A. Fortes. Computer simulation of grain growth in a bidimensional polycrystal. *Scripta Met.*, 19:1491–1496, 1985.
- [87] D. Weaire. *The Physics of Foams*. Oxford University Press, 2000. ISBN 0198505515.
- [88] K. Barmak, E. Eggeling, M. Emelianenko, Y. Epshteyn, D. Kinderlehrer, R. Sharp, and S. Ta’asan. Critical events, entropy, and the grain boundary character distribution. *Phys. Rev. B*, 83(13):134117, 2011.
- [89] M. S. Hutson, J. Veldhuis, X. Ma, H. E. Lynch, P. G. Cranston, and G. W. Brodland. Combining laser microsurgery and finite element modeling to assess cell-level epithelial mechanics. *Biophys. J.*, 97(12):3075–3085, 2009.
- [90] S. Hilgenfeldt, S. Eriskien, and R. W. Carthew. Physical modeling of cell geometric order in an epithelial tissue. *Proc. Natl. Acad. Sci.*, 105(3):907–911, 2008.
- [91] F. Graner and J. A. Glazier. Simulation of biological cell sorting using a two-dimensional extended Potts model. *Phys. Rev. Lett.*, 69(13):2013–2016, 1992.
- [92] J. C. M. Mombach, Rita M. C. de Almeida, and J. R. Iglesias. Mitosis and growth in biological tissues. *Phys. Rev. E*, 48(1):598–602, 1993.
- [93] M. Scianna, R. M. H. Merks, L. Preziosi, and E. Medico. Individual cell-based models of cell scatter of ARO and MLP-29 cells in response to hepatocyte growth factor. *J. Theor. Biol.*, 260(1):151–160, 2009.
- [94] R. Smallwood. Computational modeling of epithelial tissues. *Wiley Interdiscip. Rev. Syst. Biol. Med.*, 1(2):191–201, 2009.

- 
- [95] C. Giverso, M. Scianna, L. Preziosi, N. Lo Buono, and A. Funaro. Individual cell-based model for in-vitro mesothelial invasion of ovarian cancer. *Math. Model. Nat. Phenom.*, 5(1):203–223, 2010.
- [96] P. Pathmanathan, J. Cooper, A. Fletcher, G. Mirams, P. Murray, J. Osborne, J. Pitt-Francis, A. Walter, and S. J. Chapman. A computational study of discrete mechanical tissue models. *Phys. Biol.*, 6(3):036001, 2009.
- [97] Y. Hatwalne, S. Ramaswamy, M. Rao, and R. A. Simha. Rheology of active-particle suspensions. *Phys. Rev. Lett.*, 92(11):118101, 2004.
- [98] T. Bittig, O. Wartlick, A. Kicheva, M. González-Gáitan, and F. Jülicher. Dynamics of anisotropic tissue growth. *New J. Phys.*, 10(6):063001, 2008.
- [99] P. N. Adler. Planar signaling and morphogenesis in *Drosophila*. *Dev. Cell*, 2(5):525–535, 2002.
- [100] H. Strutt and D. Strutt. Long-range coordination of planar polarity in *Drosophila*. *BioEssays*, 27(12):1218–1227, 2005.
- [101] J. A. Zallen. Planar polarity and tissue morphogenesis. *Cell*, 129(6):1051–1063, 2007.
- [102] M. Simons and M. Mlodzik. Planar cell polarity signaling: From fly development to human disease. *Annu. Rev. Genet.*, 42(1):517–540, 2008.
- [103] E. K. Vladar, D. Antic, and J. D. Axelrod. Planar cell polarity signaling: The developing cell’s compass. *Cold Spring Harb. Perspect. Biol.*, 1(3), 2009.
- [104] H. McNeill. Planar cell polarity: Keeping hairs straight is not so simple. *Cold Spring Harb. Perspect. Biol.*, 2(2), 2010.
- [105] C. Wansleeben and F. Meijlink. The planar cell polarity pathway in vertebrate development. *Dev. Dynam.*, 240(3):616–626, 2011.
- [106] J. Casal, P. A. Lawrence, and G. Struhl. Two separate molecular systems, Dachshous/Fat and Starry night/Frizzled, act independently to confer planar cell polarity. *Development*, 133(22):4561–4572, 2006.
- [107] H. Matakatsu and S. S. Blair. Interactions between Fat and Dachshous and the regulation of planar cell polarity in the *Drosophila* wing. *Development*, 131(15):3785–3794, 2004.
- [108] A.-K. Classen, K. I. Anderson, E. Marois, and S. Eaton. Hexagonal packing of *Drosophila* wing epithelial cells by the planar cell polarity pathway. *Dev. Cell*, 9(6):805–817, 2005.

- 
- [109] C. R. Vinson and P. N. Adler. Directional non-cell autonomy and the transmission of polarity information by the *frizzled* gene of *Drosophila*. *Nature*, 329(6139):549–551, 1987.
- [110] P. A. Lawrence, J. Casal, and G. Struhl. Cell interactions and planar polarity in the abdominal epidermis of *Drosophila*. *Development*, 131(19):4651–4664, 2004.
- [111] J. Taylor, N. Abramova, J. Charlton, and P. N. Adler. *Van Gogh*: A new *Drosophila* tissue polarity gene. *Genetics*, 150(1):199–210, 1998.
- [112] Y. Shimada, S. Yonemura, H. Ohkura, D. Strutt, and T. Uemura. Polarized transport of Frizzled along the planar microtubule arrays in *Drosophila* wing epithelium. *Dev. Cell*, 10(2):209–222, 2006.
- [113] J.-F. Le Garrec, P. Lopez, and M. Kerszberg. Establishment and maintenance of planar epithelial cell polarity by asymmetric cadherin bridges: A computer model. *Dev. Dynam.*, 235(1):235–246, 2006.
- [114] J.-F. Le Garrec and M. Kerszberg. Modeling polarity buildup and cell fate decision in the fly eye: insight into the connection between the PCP and Notch pathways. *Dev. Genes Evol.*, 218(8):413–426, 2008.
- [115] K. Amonlirdviman, N. A. Khare, D. R. P. Tree, W.-S. Chen, J. D. Axelrod, and C. J. Tomlin. Mathematical modeling of planar cell polarity to understand domineering nonautonomy. *Science*, 307(5708):423–426, 2005.
- [116] R. L. Raffard, K. Amonlirdviman, J. D. Axelrod, and C. J. Tomlin. Automatic parameter identification via the adjoint method, with application to understanding planar cell polarity. In *Proceedings of the 45th IEEE Conference on Decision and Control*, pages 13–18, 2006.
- [117] R. L. Raffard, K. Amonlirdviman, J. D. Axelrod, and C. J. Tomlin. An adjoint-based parameter identification algorithm applied to planar cell polarity signaling. *IEEE Trans. Automat. Control*, 53(Special Issue on Systems Biology):109–121, 2008.
- [118] D. Ma, K. Amonlirdviman, R. L. Raffard, A. Abate, C. J. Tomlin, and J. D. Axelrod. Cell packing influences planar cell polarity signaling. *Proc. Nat. Acad. Sci.*, 105(48):18800–18805, 2008.
- [119] J. D. Axelrod and C. J. Tomlin. Modeling the control of planar cell polarity. *Wiley Interdiscip. Rev. Syst. Biol. Med.*, 3(5):588–605, 2011.
- [120] Y. Burak and B. I. Shraiman. Order and stochastic dynamics in *Drosophila* planar cell polarity. *PLoS Comput. Biol.*, 5(12), 12 2009.

- 
- [121] Hao Zhu. Is anisotropic propagation of polarized molecular distribution the common mechanism of swirling patterns of planar cell polarization? *J. Theor. Biol.*, 256(3):315–325, 2009.
- [122] S. Schamberg, P. Houston, N. Monk, and M. Owen. Modelling and analysis of planar cell polarity. *Bull. Math. Biol.*, 72(3):645–680, 2010.
- [123] J. Westerweel, T. Hofmann, C. Fukushima, and J. C. R. Hunt. The turbulent/non-turbulent interface at the outer boundary of a self-similar turbulent jet. *Exp. Fluids*, 33(6):873–878, 2002.
- [124] S. Nettlesheim, A. von Oertzen, H. H. Rotermund, and G. Ertl. Reaction diffusion patterns in the catalytic CO-oxidation on Pt(110): Front propagation and spiral waves. *J. Chem. Phys.*, 98(12):9977–9985, 1993.
- [125] M. Schirber. Nobel focus: Chemistry in 2D. *Phys. Rev. Focus*, 20:Story 15, 2007.
- [126] M. M. Karim. Micro2Macro Arthropod Gallery. <http://www.micro2macro.net/> Accessed Jul. 04, 2011.
- [127] Wikipedia, The Free Encyclopedia. <http://en.wikipedia.org/> Accessed Jun. 21, 2011. Keywords: turbulence, butterfly.
- [128] L. Wolpert, R. Beddington, T. Jessell, P. Lawrence, E. Meyerowitz, and J. Smith. *Principles of Development*. Oxford University Press, 2nd edition, 2002. ISBN 0199249393.
- [129] G. Nicolis and I. Prigogine. *Self-Organization in Nonequilibrium Systems: From Dissipative Structures to Order through Fluctuations*. John Wiley & Sons, 1977. ISBN 0471024015.
- [130] G. Nicolis. *Introduction to Nonlinear Science*. Cambridge University Press, 1995. ISBN 0521467829.
- [131] J. Walleczek. *Self-Organized Biological Dynamics & Nonlinear Control*. Cambridge University Press, 2000. ISBN 0521624363.
- [132] J. Mathieu and J. Scott. *An Introduction to Turbulent Flow*. Cambridge University Press, 2000. ISBN 0521570662.
- [133] P. A. Davidson. *Turbulence*. Oxford University Press, 2004. ISBN 0198529481.
- [134] A. M. Turing. The chemical basis of morphogenesis. *Phil. Trans. R. Soc. Lond. B*, 237(641):37–72, 1952.

- 
- [135] T. Leppänen. The theory of turing pattern formation. In R. A. Barrio and K. K. Kaski, editors, *Current Topics in Physics: In Honor of Sir Roger J Elliott*, pages 199–227. Imperial College Press, 2005.
- [136] G. Grambow. *Drosophila melanogaster* in the forest “Nauener Stadtwald” in Brandenburg, Germany. <http://commons.wikimedia.org/wiki/File:Drosophila-melanogaster-Nauener-Stadtwald-03-VII-2007-12.jpg> Accessed Jul. 04, 2011.
- [137] S. Camazine, J.-L. Deneubourg, N. R. Franks, J. Sneyd, G. Theraulaz, and E. Bonabeau. *Self-Organization in Biological Systems*. Princeton University Press, 2001. ISBN 0691012113.
- [138] C. Kittel. *Introduction to Solid State Physics*. Wiley, 8th edition, 2004. ISBN 047141526X.
- [139] H. Haken. *Synergetics*. Springer-Verlag, 3rd edition, 1983. ISBN 3540123563.
- [140] H. Haken. *Advanced Synergetics: Instability Hierarchies of Self-Organizing Systems and Devices*. Springer-Verlag, 3rd printing, 1993. ISBN 3540121625.
- [141] Stanford Encyclopedia of Philosophy. <http://plato.stanford.edu/> Accessed Jan. 5, 2011. Keyword: emergent properties.
- [142] D. Weaire and N. Rivier. Soap, cells and statistics—Random patterns in two dimensions. *Contemp. Phys.*, 25(1):59–99, 1984.
- [143] E. Polak and G. Ribière. Note sur la convergence de méthodes de directions conjuguées. *Rev. Fr. Inform. Rech. O.*, 3(16):35–43, 1969.
- [144] B. Gough. *GNU Scientific Library Reference Manual*. Network Theory Limited, 3rd revised edition, 2009. ISBN 0954612078.
- [145] F. T. Lewis. The correlation between cell division and the shapes and sizes of prismatic cells in the epidermis of cucumis. *Anat. Rec.*, 38(3):341–376, 1928.
- [146] F. T. Lewis. The geometry of growth and cell division in epithelial mosaics. *Am. J. Botany*, 30(10):766–776, 1943.
- [147] N. W. Ashcroft and N. D. Mermin. *Solid State Physics*. Brooks/Cole, Thomson Learning, 1976. ISBN 0030839939.
- [148] D. T. Gillespie. A general method for numerically simulating the stochastic time evolution of coupled chemical reactions. *J. Comp. Phys.*, 22(4):403–434, 1976.

- 
- [149] L. Devroye. *Non-Uniform Random Variate Generation*. Springer, 1986. ISBN 0387963057. Note: This book has been republished electronically and is available at <http://cg.scs.carleton.ca/~luc/rnbookindex.html> Accessed Sep. 2, 2011.
- [150] G. H. Golub and C. F. Van Loan. *Matrix Computations*. The Johns Hopkins University Press, 3rd edition, 1996. ISBN 0801854148.
- [151] G. B. Blanchard, A. J. Kabla, N. L. Schultz, L. C. Butler, B. Sanson, N. Gorfinkiel, L. Mahadevan, and R. J. Adams. Tissue tectonics: morphogenetic strain rates, cell shape change and intercalation. *Nat. Methods*, 6(6): 458–464, 2009.
- [152] P. G. de Gennes and J. Prost. *The Physics of Liquid Crystals*. Oxford University Press, 2nd edition, 1995. ISBN 9780198517856.
- [153] B. Guirao, A. Meunier, S. Mortaud, A. Aguilar, J.-M. Corsi, L. Strehl, Y. Hirota, A. Desoeuvre, C. Boutin, Y.-G. Han, Z. Mirzadeh, H. Cremer, M. Montcouquiol, K. Sawamoto, and N. Spassky. Coupling between hydrodynamic forces and planar cell polarity orients mammalian motile cilia. *Nat. Cell Biol.*, 12(4):341–350, 2010.
- [154] M. S. Hutson, Y. Tokutake, M.-S. Chang, J. W. Bloor, S. Venakides, D. P. Kiehart, and G. S. Edwards. Forces for morphogenesis investigated with laser microsurgery and quantitative modeling. *Science*, 300(5616):145–149, 2003.
- [155] S. W. Grill. Growing up is stressful: biophysical laws of morphogenesis. *Curr. Opin. Genetics Dev.*, 21(5):647–652, 2011.
- [156] T. C. Hales. The honeycomb conjecture. *Discrete Comput. Geom.*, 25(1):1–22, 2001.

# Versicherung

Hiermit versichere ich, dass ich die vorliegende Arbeit ohne unzulässige Hilfe Dritter und ohne Benutzung anderer als der angegebenen Hilfsmittel angefertigt habe; die aus fremden Quellen direkt oder indirekt übernommenen Gedanken sind als solche kenntlich gemacht. Die Arbeit wurde bisher weder im Inland noch im Ausland in gleicher oder ähnlicher Form einer anderen Prüfungsbehörde vorgelegt. Die vorliegende Arbeit wurde am Max-Planck-Institut für Physik komplexer Systeme angefertigt und von Prof. Dr. Frank Jülicher betreut.

Dresden, den 3.2.2012, Douglas B. Staple